

**The Rheology of Perovskites and its Implication
for Mantle Dynamics**

by

Kathleen Valerie WRIGHT

*A thesis submitted to the University of London for the degree
of Doctor of Philosophy*

August 1991

Department of Geological Science

University College London

ProQuest Number: 10609786

All rights reserved

INFORMATION TO ALL USERS

The quality of this reproduction is dependent upon the quality of the copy submitted.

In the unlikely event that the author did not send a complete manuscript and there are missing pages, these will be noted. Also, if material had to be removed, a note will indicate the deletion.



ProQuest 10609786

Published by ProQuest LLC (2017). Copyright of the Dissertation is held by the Author.

All rights reserved.

This work is protected against unauthorized copying under Title 17, United States Code
Microform Edition © ProQuest LLC.

ProQuest LLC.
789 East Eisenhower Parkway
P.O. Box 1346
Ann Arbor, MI 48106 – 1346

ABSTRACT

A combination of experimental studies on analogues and computer simulation techniques has been used to investigate the rheological behaviour of MgSiO_3 , the major phase in the Earth's lower mantle.

Creep experiments have been performed on two oxide perovskites, CaTiO_3 and NaNbO_3 . Both are found to deform according to a dislocation controlled power-law mechanism. Experiments performed on CaTiO_3 with applied stress parallel to two different directions, indicate a strong dependence of creep rate on orientation.

Computer simulation techniques have been used to model defects and diffusion in the perovskites SrTiO_3 , CaTiO_3 and MgSiO_3 . The calculated value of activation enthalpy for oxygen diffusion in SrTiO_3 agrees well with published experimental data thereby justifying the use of this method for materials with the perovskite structure. In CaTiO_3 , Ti is predicted to be the rate controlling species. Defects and diffusion in MgSiO_3 have been simulated at pressures of 0, 60 and 125 GPa. Si is predicted to be the rate controlling species at 0 and 60 GPa, but at 125 GPa, Mg has the higher diffusion activation enthalpy.

The results of the experiments on perovskites have been compared to those of other studies to assess the likelihood of perovskites forming an isomechanical series. No evidence for isomechanical behaviour has been found. However, CaTiO_3 is considered to be a suitable analogue for MgSiO_3 .

The information from experiments and simulations has been combined in order to compile rheological data sets for both CaTiO_3 and MgSiO_3 perovskites. These data sets have been used to construct deformation mechanism maps for both and in the case of MgSiO_3 to construct viscosity profiles for the lower mantle.

Materials-based predictions of mantle viscosity are comparable with those inferred from geophysics. The viscosity profiles indicate that the lower mantle is best described by a power-law rheology, with an increase of a factor 10 in viscosity with depth. The models are consistent with, but do not exclusively require, whole mantle convection.

ACKNOWLEDGEMENTS

First and foremost, I would like to thank my supervisor, Professor G.D. Price for his unfailing support during my years at U.C.L. His help, advice and continued interest in the project have been invaluable.

I would also like to thank Alison Wall for many useful discussions on all aspects of the project, J.P. Poirier and F. Guyot for help and advice with the electron microscopy, Phil Meredith for long discussions on the experimental apparatus and results and Ian Wood for his continuing good humour.

On the technical side thanks go to John Bowles for looking after the creep apparatus so well, Pete Woods for being able to fix anything and everything with the minimum of fuss, and to Sean Houlding for the use of his radio and help with sample preparation. Thanks also to Colin Stuart for the majority of the thesis drawings, to Mike Grey for photography and to Ron Dudman for his monumental patience.

My thanks also to the many staff and students at U.C.L who have given me help and advice over the years, in particular, Judith Milledge, Monica Mendelssohn, Wendy Kirk, Trish Cooper, Janet Baker and Guy Cooper.

Finally, I would like to thank my son Tom for patience and understanding beyond his years, without which I could not have completed this work.

CONTENTS

Title	1
Abstract	2
Acknowledgements	4

CHAPTER 1 : INTRODUCTION

1.1 Introduction	17
1.2 Earth structure and composition	17
1.3 The thermal state of the Earth	22
1.3.1 Heat sources in the Earth	22
1.3.2 Temperature gradients in the mantle	23
1.4 Thermal convection	23
1.5 Convection in the Earth's mantle	26
1.6 The importance of rheology	28

CHAPTER 2 : THEORIES OF HIGH TEMPERATURE CREEP

2.1 Introduction	30
2.2 Diffusional creep	31
2.3 Dislocation creep	34
2.3.1 Dislocations	34
2.3.2 Power-Law creep models	35
2.3.2.1 The Weertman model	36
2.3.2.2 Cross-slip controlled creep	37
2.3.3 Harper-Dorn creep	38
2.4 Superplasticity	39
2.5 Dynamic recrystallization	39
2.6 The effects of pressure	40
2.6.1 The activation volume	40
2.6.2 Material parameters	42

2.7 Deformation mechanism maps and isomechanical series	42
2.8 Summary	44

CHAPTER 3 : HIGH TEMPERATURE CREEP EXPERIMENTS

3.1 Introduction	46
3.2 Samples	47
3.2.1 CaTiO ₃	47
3.2.2 NaNbO ₃	50
3.3 The creep apparatus	50
3.4 Calibration procedures	53
3.4.1 Calibration of the furnace	53
3.4.2 Calibration of the LVDT	55
3.5 Methodology	55
3.5.1 Sample preparation	55
3.5.2 Sample orientation	55
3.5.3 Calculation of applied stress	57
3.5.4 Experimental procedure	57
3.6 Analysis of data	58
3.7 Transmission Electron Microscopy	60
3.7.1 General description of TEM	60
3.7.2 TEM techniques	61
3.7.3 Sample preparation	63

CHAPTER 4 : EXPERIMENTAL RESULTS

4.1 Experimental conditions	64
4.1.1 Experiments on CaTiO ₃	64
4.1.2 Experiments on NaNbO ₃	69
4.2 Data analysis	71
4.2.1 Analysis of data by linear regression	71

4.2.2 Analysis by inversion	74
4.3 Results	75
4.3.1 CaTiO ₃ with stress parallel to <100> _{pc}	75
4.3.2 CaTiO ₃ with stress parallel to <110> _{pc}	75
4.3.3 NaNbO ₃	76
4.4 Examination of samples	77
4.4.1 Examination and analysis using TEM	77
4.5 Summary and conclusions	°1
4.5.1 A creep law for CaTiO ₃	81
4.5.2 A creep law for NaNbO ₃	82

CHAPTER 5: COMPUTER SIMULATION OF DEFECTS AND DIFFUSION IN PEROVSKITE

5.1 Introduction	90
5.2 Simulation techniques	91
5.2.1 Interatomic potentials	91
5.2.2 Modelling the perfect lattice	92
5.2.3 Calculating defect energies	93
5.3 The treatment of defects and diffusion	95
5.3.1 Defect formation energies	95
5.3.2 Migration and diffusion	96
5.3.3 Diffusion coefficients	97
5.3.4 Defect energies from CASCADE	98
5.4 Choice of potential parameters	99
5.5 Perfect lattice calculations : Results	101
5.6 Simulation of defects and diffusion in SrTiO ₃	101
5.7 Simulation of defects and diffusion in CaTiO ₃	106
5.7.1 Defect formation	106
5.7.2 Diffusion in CaTiO ₃	108

5.8 Summary of results for SrTiO ₃ and CaTiO ₃	110
5.9 Defects and diffusion in MgSiO ₃	112
5.9.1 Defects in MgSiO ₃	112
5.9.2 Silicon diffusion in MgSiO ₃ at 0 GPa	117
5.9.3 Silicon diffusion at high pressure	119
5.8.4 Diffusion of Mg at high pressure	121
5.9 Defect reactions in MgSiO ₃	122
5.10 Discussion of results	122

CHAPTER 6 : THE RHEOLOGY OF PEROVSKITES

6.1 Introduction	129
6.2 Review of experiments	129
6.3 Comparability of data	131
6.4 The rheology of perovskites	132
6.5 An analogue for MgSiO ₃	133
6.6 Deformation mechanism maps for perovskites	133
6.6.1 Methods of construction	134
6.6.2 Including the effects of pressure	136
6.7 Deformation maps for CaTiO ₃	137
6.7.1 A rheological data set for CaTiO ₃	137
6.7.2 A deformation mechanism map for CaTiO ₃	139
6.7.3 Discussion	144
6.8 Deformation maps for MgSiO ₃	147
6.8.1 A rheological data set for MgSiO ₃	147
6.8.2 Deformation maps for MgSiO ₃ with contours of constant strain rate	147 158
6.8.3 Deformation maps for MgSiO ₃ with contours of constant viscosity	158
6.9 Discussion	

CHAPTER 7 : THE RHEOLOGY OF THE LOWER MANTLE

7.1 Introduction	163
7.2 Mantle viscosity from Geophysics	164
7.3 Previous models of mantle viscosity	166
7.4 Calculation of viscosity profiles: Methodology	168
7.5 Models of lower mantle viscosity	169
7.5.1 The effects of temperature and stress	170
7.5.2 The effects of grain size	172
7.5.3 Changing the activation parameter	173
7.5.4 Discussion	175
7.6 Rheology and convection	178
7.7 Conclusions	180
Bibliography	183

APPENDICES

A. Creep curves for experiments on CaTiO_3 and NaNbO_3	199
B. Program for construction of deformation mechanism maps	212
C. List of commonly used symbols	219

LIST OF FIGURES

CHAPTER 1 : INTRODUCTION

1.1 Structure of the Earth	19
1.2 Phase changes through the mantle	21
1.3 The geotherms of Stacey and Brown and Shankland	24

CHAPTER 2 : THEORIES OF HIGH TEMPERATURE CREEP

2.1 The flow of vacancies in a crystal	33
2.2 Arrangement of atoms around dislocations	35
2.3 A simplified deformation map of MgO	43

CHAPTER 3 : HIGH TEMPERATURE CREEP EXPERIMRNTS

3.1 The ideal perovskite structure	48
3.2 Schematic diagram of the creep apparatus	52
3.3 Temperature gradients along the furnace length	54
3.4 Plots of length change with time	56
3.5 Schemetic creep curve	59
3.6 Ray diagram of the transmission electron microscope	62

CHAPTER 4 : EXPERIMENTAL RESULTS

4.1 Typical creep curves for CaTiO_3 $\langle 100 \rangle_{\text{pc}}$	66
4.2 Typical creep curves for CaTiO_3 $\langle 110 \rangle_{\text{pc}}$	68
4.3 Typical creep curves for NaNbO_3	70
4.4 Calculation of Q and n using linear regression	72
4.5 Sketch of dislocation configuration in Plate 4.10	
4.6 Schematic representation of colinear partial dislocation	

CHAPTER 5 : COMPUTER SIMULATION OF DEFECTS AND DIFFUSION IN PEROVSKITES

5.1 Shell model	91
5.2 The Mott-Littleton sphere	98
5.3 Oxygen migration path in SrTiO ₃	106
5.4 O migration pathways in CaTiO ₃	109
5.5 Ca migration pathway in CaTiO ₃	110
5.6 Ti migration pathway in CaTiO ₃	111
5.7 Si migration pathways in MgSiO ₃	118
5.8 Si migration with an O vacancy	119
5.9 Experimental and calculated variation of volume with pressure	127

CHAPTER 6: THE RHEOLOGY OF PEROVSKITES

6.1 Structure of the perovskites CaTiO ₃ and MgSiO ₃	134
6.2 Deformation map for CaTiO ₃	140
6.3 Deformation map for CaTiO ₃	142
6.4 Deformation map for CaTiO ₃	143
6.5 Deformation map for CaTiO ₃ at 10 GPa	145
6.6 Deformation map for CaTiO ₃ at 10 GPa	146
6.7 Deformation map for MgSiO ₃ at 60 GPa	150
6.8 Deformation map for MgSiO ₃ at 60 GPa	151
6.9 Deformation map for MgSiO ₃ at 60 GPa	152
6.10 Deformation map for MgSiO ₃ at 60 GPa	153
6.11 Deformation map for MgSiO ₃ at 125 GPa	154
6.12 Deformation map for MgSiO ₃ at 125 GPa	155
6.13 Deformation map for MgSiO ₃ at 125 GPa	156
6.14 Deformation map for MgSiO ₃ at 125 GPa	157
6.15 Deformation map for MgSiO ₃ at 60 GPa	159
6.16 Deformation map for MgSiO ₃ at 60 GPa	160
6.17 Deformation map for MgSiO ₃ at 60 GPa	161

CHAPTER 7: THE RHEOLOGY OF THE LOWER MANTLE

7.1 Viscosity profiles of the lower mantle	171
7.2 Viscosity profiles for grain size of 1.0 mm	172
7.3 The effects of changing V^*	174
7.4 Viscosity profiles using the geotherm of Stacey and grain size of 1.0 mm	175
7.5 Viscosity profile using a large value of V^* and the Stacey geotherm	176
7.6 Viscosity profile using a large value of V^* and the geotherm of Brown and Shankland	176

APPENDICES

A.1 Creep curves for CaTiO_3 with stress parallel to $\langle 100 \rangle_{pc}$	199
A.2 Creep curves for CaTiO_3 with stress parallel to $\langle 110 \rangle_{pc}$	203
A.3 Creep curves for NaNbO_3	208

LIST OF PLATES

4.1 Dark field image of undeformed, unannealed CaTiO ₃	83
4.2 CaTiO ₃ annealed at 1520° C for 2 hours	83
4.3 Dark field image of dislocation from PVCA17	84
4.4 Dark field image from PVCA38	84
4.5 Weak beam image of dislocation PVCA18	85
4.6 Dark field image of the same dislocation	85
4.7 Bright field image of dislocation from PVCA18	86
4.8 Weak beam image of the same dislocations	86
4.9 Bright field image of dislocation pairs	37
4.10 Dislocation network from PVCA17	87
4.11 Bright field image of 'scallop' from PVCA18	88
4.12 Detail of 'scallop' from PVCA18	88
4.13 Two sets of dislocations from PVCA21	89
4.14 The same dislocations as above	89

LIST OF TABLES

CHAPTER 3 : HIGH TEMPERATURE CREEP EXPERIMENTS

3.1 Structure and properties of CaTiO_3 and NaNbO_3	49
3.2 Probe analysis of CaTiO_3	49

CHAPTER 4 : EXPERIMENTAL RESULTS

4.1 Experimental conditions	64
4.2 Results of experiments on CaTiO_3 $\langle 100 \rangle_{\text{pc}}$	55
4.3 Results of experiments on CaTiO_3 $\langle 110 \rangle_{\text{pc}}$	67
4.4 Results of experiments on NaNbO_3	69
4.5 Results of inversion for CaTiO_3 $\langle 100 \rangle_{\text{pc}}$	75
4.6 Results of inversion for CaTiO_3 $\langle 110 \rangle_{\text{pc}}$	76
4.7 Results of inversion for NaNbO_3	

CHAPTER 5 : COMPUTER SIMULATION OF DEFECTS AND DIFFUSION IN PEROVSKITES

5.1 Short range potential parameters used in this study	100
5.2 Comparison of experimental and calculated lattice parameters and elastic moduli for the perovskites SrTiO_3 , CaTiO_3 and MgSiO_3	102
5.3 Calculated lattice energy of phases used in this study	103
5.4 Predicted vacancy and Schottky defect formation enthalpies in SrTiO_3	104
5.5 Equilibrium site fraction of vacancies in SrTiO_3	105
5.6 Predicted vacancy and Schottky defect formation enthalpies in CaTiO_3	107
5.7 Equilibrium site fraction of vacancies in CaTiO_3	108
5.8 Predicted vacancy and Schottky defect formation enthalpies in MgSiO_3 at 0 GPa	113

5.9 Equilibrium site fraction of vacancies in MgSiO_3 at 0 GPa	114
5.10 Predicted vacancy and Schottky defect formation enthalpies in MgSiO_3 at 60 GPa	115
5.11 Predicted vacancy and Schottky defect formation enthalpies in MgSiO_3 at 125 GPa	116
5.12 Activation enthalpies for Si diffusion at zero and simulated high pressure	120
5.13 Activation volumes for Si migration and diffusion	121
5.14 Activation enthalpies for Mg migration and diffusion	121
5.15 Enthalpies of reaction and per vacancy at 0 and 60 GPa	123

Chapter 6 : THE RHEOLOGY OF PEROVSKITES

6.1 Summary of experimental creep data on oxide perovskites	131
6.2 A rheological data set for CaTiO_3	138
6.3 A rheological data set for MgSiO_3	148

CHAPTER 1: INTRODUCTION

1.1 Introduction

Rheology is the branch of physics which deals with the deformation and flow of matter in response to some applied stress. Since deformation occurs on all scales from creep in crystals to convection in the mantle, it is of paramount importance in modelling geophysical processes.

Two broad approaches are used to investigate the rheology of the Earth, phenomenological and atomistic. The first treats the Earth as a continuum and constrains rheological variables such as viscosity by consideration of the bulk properties alone. The atomistic approach in contrast, is concerned with processes occurring on the microscopic level.

The primary aim of this thesis is to investigate the rheological nature of the Earth's lower mantle using the atomistic or microrheological approach. Since this is dependent on a knowledge of the rheology of the minerals present, the secondary aim must be to characterise the deformation behaviour of the major component, $(\text{MgFe})\text{SiO}_3$, with the perovskite structure.

In this introductory chapter, various models of the structure, composition and dynamics of the Earth's interior are reviewed and the main problems identified. From this overview, the importance of rheology to these problems is assessed. Finally, the methods used to carry out the aims of this research will be outlined.

1.2 Earth structure and composition

A first step in understanding the dynamical behaviour of the Earth's mantle is to model its structure and composition. Information on the structure

of the Earth's interior comes primarily from the observation of seismic wave travel times. Two types of wave are important, compressional P-waves and longitudinal S-waves, whose velocities V_p and V_s are a function of the elastic properties and density of the medium through which they pass. By inversion of seismic data, the values of elastic moduli and density of Earth materials can be calculated as a function of depth (Dziewonski and Anderson 1981) thus providing a physical constraint on mantle composition.

Seismology has led to the model of an Earth composed of a spherically symmetrical layers (Figure 1.1). The boundary between each layer is marked by a sharp change or discontinuity in seismic velocities, indicating a change in the physical properties of the materials. The Earth's mantle is then divided into three seismically distinct layers; upper mantle, transition zone and lower mantle.

Since less than 1% of the Earth's mass can be sampled directly, estimates of the chemical composition of the bulk Earth are derived from the examination of meteoritic material and spectral analysis of the Sun's atmosphere. One particular group of meteorites, the carbonaceous chondrites, are widely believed to be representative of the primitive material from which the Earth, sun and planets were formed. Elemental abundances in chondrites combined with geochemical considerations have led to the development of the Chondritic Earth Model (eg. Ganapthy and Anders 1974). The use of such models for bulk Earth chemistry provide a chemical constraint on mantle composition.

Based on the constraints outlined above and experimental evidence, Ringwood (1975) proposed that the mantle has a chemical composition close to that of the hypothetical rock pyrolite (olivine + pyroxene rock). Experimental evidence (eg. Suito 1977, Ito and Takahashi 1987, 1989) has shown that with increasing depth, olivine and other pyrolite minerals undergo a series of phase transitions to successively denser forms as shown in Figure

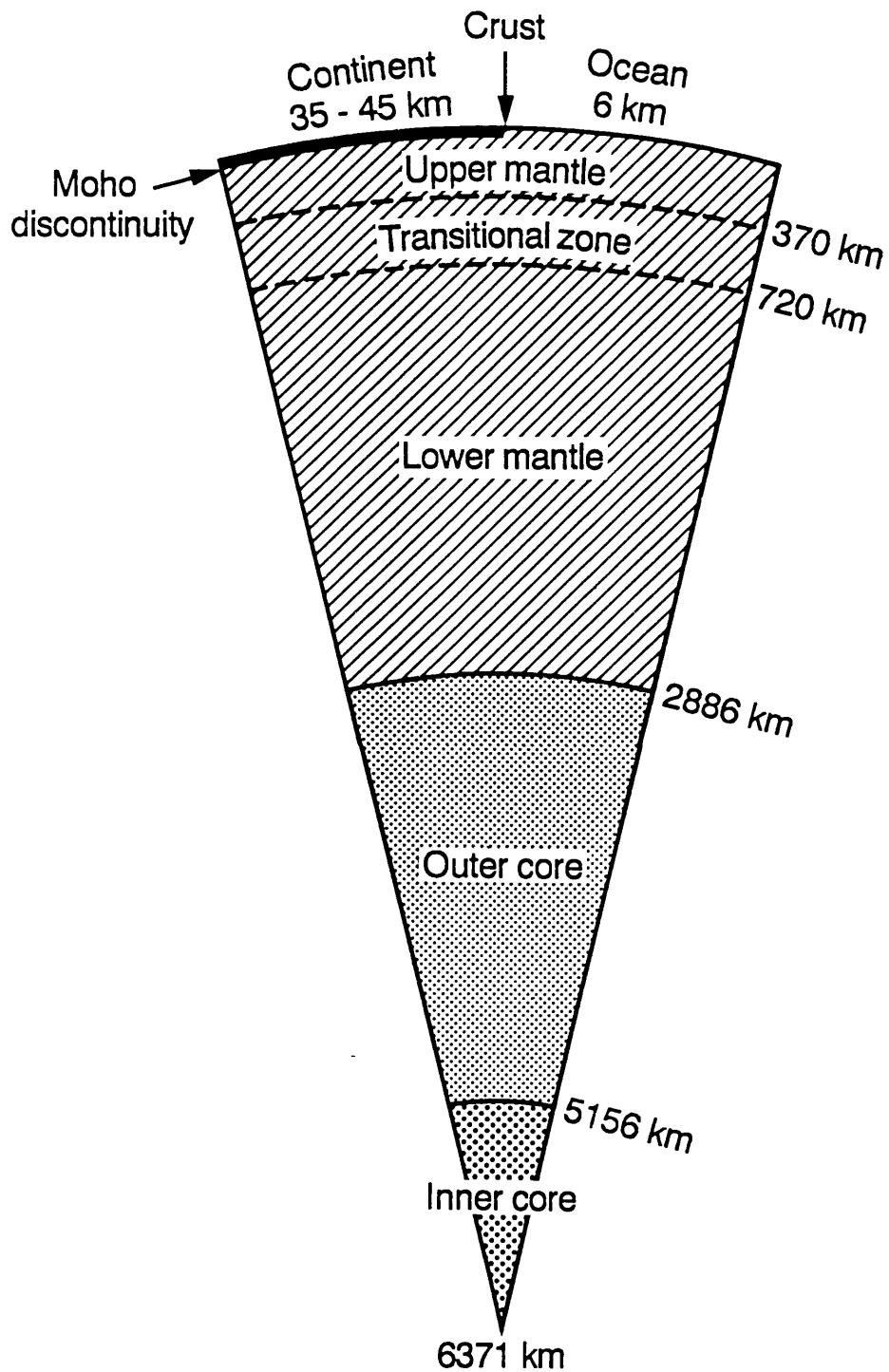


Figure 1.1 Structure of the Earth. After Bott (1982)

1.2. The first major transition of olivine to the β -phase and then to the spinel structure marks the 400 km discontinuity, while dissociation of spinel to the perovskite structure plus magnesiowustite takes place at the 670 km discontinuity. Anderson and Bass (1986) however, have proposed a piclogite composition (eclogite + picrite) for the transition zone thus invoking a change in chemistry to account for the discontinuities at 400 km and 670 km rather than a phase change. The possibility of a chemical boundary between the upper and lower mantle has important implications for the evolution and dynamics of the mantle and has been a subject of much debate.

Weidner and Ito (1987) modeled the acoustic velocities of the transition zone for both pyrolite and piclogite compositions. The above authors found that the pyrolite model of Ringwood (1975) agreed well with the observed seismic velocities while the piclogite model could not reproduce the 670 km discontinuity. The resolution of seismic data is such that it is not possible to discount some changes in composition at this major boundary, so that while the hypothesis of a phase transition at the discontinuity is consistent with present seismic and mineral physics data, it is not required by it exclusively by it.

In summary, on the basis of seismology, the Earth's mantle can be divided into three layers with differing physical properties. The mantle has a composition close to that of pyrolite with the olivine rich phase assemblage of the upper mantle transforming to denser structures with increasing pressure and temperature. The lower mantle is composed of some 70 - 90% $(\text{Mg,Fe})\text{SiO}_3$ perovskite with 10-30% $(\text{Mg,Fe})\text{O}$ magnesiowustite plus small amounts of other high pressure phases (Madon et al. 1989). Changes in chemistry may also occur across the upper-lower mantle boundary which would have a profound affect on the dynamic state of the Earth.

Pressure	Phases	Depth
0 GPa		0 km
	Olivine	
	Pyroxene + Garnet	
	Component	
	Olivine $(\text{Fe,Mg})_2\text{SiO}_4$	
	Pyroxene $(\text{Mg,Fe,Ca})\text{SiO}_3$ + Garnet $(\text{Mg,Fe,Ca})_3\text{Al}_2\text{Si}_3\text{O}_{12}$	
		200 km
10 GPa		
	β -phase $(\text{Mg,Fe})_2\text{SiO}_4$	
	Garnet-majorite $(\text{Mg,Fe,Ca})[(\text{Mg,Fe})\text{Si,Al}_2]\text{Si}_3\text{O}_{12}$	
		400 km
	γ -phase $(\text{Mg,Fe})_2\text{SiO}_4$	
20 GPa	Ilmenite $(\text{Mg,Fe,Ca})(\text{Si,Al})\text{O}_3$	
	Perovskite $(\text{Mg,Fe,Ca})(\text{Si,Al})\text{O}_3$	
		600 km
	Perovskite $(\text{Mg,Fe,Ca})(\text{Si,Al})\text{O}_3$ + Magnesiowustite $(\text{Mg,Fe})\text{O}$	
30 GPa		
		800 km

Figure 1.2 Mantle phase changes with depth.
After Jeanloz and Thompson (1983)

1.3 The thermal state of the Earth

The nature of the geotherm and heat flow within the Earth are closely related to rheological behaviour, but have not yet been determined with any great accuracy. The distribution of heat sources, thermal properties of minerals and the evolution of the system with time are all important factors influencing the thermal state of the Earth, yet are not well understood. There are two basic constraints on thermal models; observed heat flow at the Earth's surface and the solidus temperature of the minerals present. The former can be measured whilst the latter must be extrapolated from conditions obtainable in the laboratory to those appropriate for the mantle.

1.3.1 Heat sources in the Earth

The total heat loss of the Earth is estimated to be of the order of 42.0×10^{13} W (Sclater et al. 1980) with most of the loss occurring over the oceans due to plate formation processes. Radioactive decay of long-lived isotopes such as U, Th and K account for the heat flow over continental regions where these elements are concentrated into granitic type rocks. There is considerable debate as to the distribution of radioactive elements in the Earth. The concentration of U and Th in continental rocks is close to chondritic values while ^{40}K is depleted by some 20% relative to chondrites. Bukowinski (1976) argued that the missing ^{40}K could be present in the Earth's core. If the Earth does contain an abundance of radioactive elements roughly equal to Chondrites, then the heat generated by these sources will be 31.4×10^{12} W (Ranalli 1987), some 20 to 25% less than the total heat loss. Slow cooling of the Earth is the most likely heat source to make up the deficit. During the Earth's early history however, heat generation was probably greater than the present due to decay of short lived isotopes such as ^{26}Al (Brown and Musset 1984).

1.3.2 Temperature gradients in the mantle

Near the Earth's surface, the temperature gradient is, on average, 30 K km^{-1} , however this must fall off considerably in order to comply with a solid Earth. Temperature gradients can be fixed within crustal rocks using techniques of geothermometry but at greater depths this is not possible.

If the major means of heat transport within the Earth is by thermal convection, as seems likely, then the mantle geotherm will be approximately adiabatic. Within convection cells, adiabatic temperature gradients can be expected, but in the thermal boundary layers at the top and base of the cells, a superadiabatic gradient is more likely. The quasi-rigid lithosphere can be considered as the upper thermal boundary layer, while there are strong indications of a superadiabatic thermal boundary layer above the core-mantle interface in the so called D" layer (Olson et al. 1987). A third thermal boundary layer has also been proposed at the 670 km discontinuity (see Jeanloz and Thompson 1983) which would have important implications for mantle dynamical models and is discussed in section 1.5

A number of different geotherms have been proposed, all based on different assumptions. Those of Stacey (1977) and Brown and Shankland (1981) bracket the upper and lower limits respectively of temperature at depth and are shown in figure 1.3. At present, a realistic geotherm cannot be modelled with any great confidence.

1.4 Thermal convection.

The fundamental requirement for the onset of thermal convection in a body of fluid is a *lateral* variation in density. Variations in density due to heating, either from below or within a fluid layer, generate the buoyancy forces which drive convection.

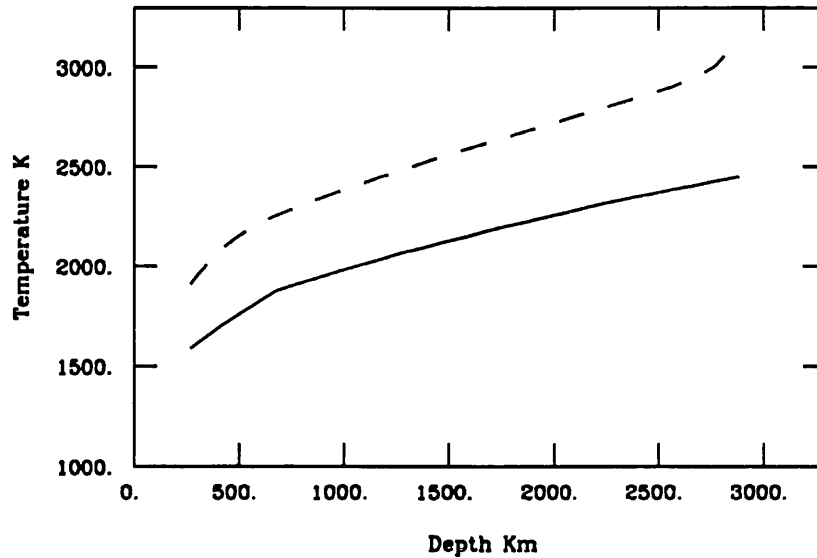


Figure 1.3 The geotherms of Stacey (dashed line) and Brown and Shankland (solid line).

Consider a fluid heated uniformly from below and cooled uniformly at the upper surface. Gentle heating leads to a uniform temperature gradient with no lateral variation in density so that heat transfer is by conduction alone. Increasing the temperature of the heat source reduces the density of the lower layers further. Any slight lateral density variation will cause the lighter material to rise and hence convection begins. Convection cells with an ordered geometry, rather like a honeycomb, are characteristic of stable Bernard convection. But as temperature rises further, this arrangement becomes unstable and begins to disintegrate leading to chaotic turbulent behaviour. In general, the onset of convective transfer depends on the balance of buoyancy forces which favour convection and inhibiting forces which do not. This is expressed by the Rayleigh number, a dimensionless parameter defined as:

$$Ra = \alpha \Delta T g Z^3 / \kappa \vartheta \quad (1.1)$$

where α is the volume coefficient of thermal expansion, ΔT the temperature increase across the layer, g the gravitational acceleration and Z the depth of the layer, κ is the thermal diffusivity and ϑ the kinematic viscosity defined as viscosity divided by density. Equation 1.1 shows that high values of α and a large temperature difference across a deep layer will all serve to promote buoyancy forces and so encourage convection. The value of κ reflects the importance of conduction, and viscosity the mechanical resistance to flow, both of which will inhibit convection if large. The Rayleigh number is therefore the most important parameter in determining whether or not convection will occur. Convection normally starts when Ra reaches a critical value of approximately 10^3 . Vigorous convection, where heat transport by conduction is no longer important, occurs when $Ra = 10^5$ and at 10^6 instability set in and convection becomes chaotic (Ranalli 1987).

A second dimensionless parameter, the Nusselt number can be used to assess the relative importance of convective and conductive heat transfer within a system:

$$Nu = q/q_c \quad \text{or} \quad Nu = \Delta T_c / \Delta T \quad (1.2)$$

where q_c and ΔT_c are respectively the heat flow and temperature change across the layer in the absence of convection and q and ΔT the same for the case where only convection is occurring. The Rayleigh and Nusselt numbers are related by the expression;

$$Nu = m Ra^B \quad (1.3)$$

where m and B are constants depending on cell geometry and the Rayleigh number range studied. A more rigorous treatment of thermal convection can be found in Busse (1989).

1.5 Convection in the Earth's mantle

Convection in the Earth's mantle, as a means of driving continental drift was first proposed by Sir Aulter Holmes in a series of papers published between 1926 and 1928. However, Holmes' ideas were not seriously considered by many geophysicists until the advent of the plate tectonic theory in the late 1960's, since it was believed that the mantle was too viscous to permit convective motion. The exact relationship between convection and plate motion is still not well understood. Plates can be considered to ride along on the upper thermal boundary layer of the convective cell, although there are sufficient forces arising at ocean ridges (ridge push force) and at subduction zones (slab pull forces) to act as a driving force for plate motion (see Brown and Musset (1984) for a discussion). Nevertheless, movement of lithospheric plates and subsequent transfer of mass are ample proof that convection is occurring in the mantle.

Over the past two decades, the principle debate has not concerned the existence of convection but rather the depth of convection cells; ie. whether the mantle convects as a single body (whole mantle model) or in two discretely convecting layers (double layer model). Convection in the Earth's mantle is certainly more complex than in the case of the homogeneous fluid considered in the previous section. The effects of phase transitions, chemical stratification and a highly temperature dependent viscosity must all be considered along with the constraints imposed by geophysical observations (see Chapter 7). The crux of the argument centres around the nature of the 670 km discontinuity. Is it the result of a phase change, a chemical change, or some combination of the two? Evidence to support each of the two convection models is taken from geophysical observation and from experimental and numerical modelling.

The results of experimental fluid dynamics modelling (eg. Richter and McKenzie 1979) indicates that a density difference of between 2 and 5% is

needed to maintain stable double convection. An increase in density can be invoked by increasing the Fe or Si content (see Lees et al. 1983) and/or by a phase change with a sufficiently large, negative Clapyron slope. An exothermic phase change (positive Clapyron slope) has no effect on convection, although an endothermic transition will act as a destabilizing agent (Busse 1989). Both experimental and theoretical work (eg. Ito and Katsura 1989, Ito and Takahashi 1989 and Price et al. 1989) predict a shallow negative Clapyron slope for the spinel to perovskite plus magnesiowustite transition, of $-2 \times 10^{-6} \text{ Pa K}^{-1}$. This is considered to be insufficient to lead to a double convective system in the absence of a chemically derived density increase.

Lees et al. (1983) considered the depth interval over which the transition would take place, and argued that it would be too wide to produce the sharp seismic velocity jump required, but instead would give a steep velocity gradient. However, recent experiments (Ito and Takahashi 1989) show the sp \rightarrow pv+mw transition is essentially univariant and could occur over a depth interval as narrow as 4 km, consistent with seismic observations.

Perhaps one of the strongest arguments against double convection concerns the nature of the geotherm across the 670 km boundary between the convective cells. Invoking a double convective system requires the presence of a double thermal boundary layer (Richter and McKenzie 1981). Estimates of width and temperature increase across such a boundary range from 90 km and 670 K (Richter and McKenzie 1981) to 300 km and 2050 K (Olson 1981). If present, the thermal boundary layer should be accompanied by corresponding changes in physical and rheological properties. Lees et al. (1983) reported that the calculated seismic velocities were within the range of uncertainty for the model of Richter and McKenzie but incompatible with that of Olson. Therefore on the basis of seismic data, the possible existence of a thermal boundary layer cannot be ruled out.

A double convective system favours arguments for two distinct

geochemical reservoirs within the mantle, inferred from the study of Sm-Nd and Rb-Sr isotopic ratios in basaltic material (see O'Nions 1987 for a comprehensive review). Furthermore, a density difference of 3-5% would prevent subducting slabs from penetrating the boundary between upper and lower convective systems (Christensen 1989). The absence of earthquakes from depths greater than 700 km has traditionally been taken as evidence of such a density difference. However, the results of recent studies by Crager and Jordan (1986) have cast considerable doubt on this evidence.

There seems no way then, that a simple double or single convective system can accommodate all the available geophysical and geochemical evidence. Large scale numerical models (eg. Christensen and Yuen 1984, Christensen 1989, Peltier and Jarvis 1989) have had some success in improving our understanding of convective processes in the mantle, although the conclusions do not unambiguously support one model or the other. 'Leaky' double convection with intermittent transfer of mass across the boundary has been suggested (Christensen and Yuen 1985, Machtal and Weber 1991) as a means of accommodating all of the available data. However, it should be appreciated that such models are only as good as the data used in their construction and at the present time there are still many areas of uncertainty, particularly as regards the properties of the major lower mantle phase (Mg,Fe)SiO₃ perovskite.

1.6 The importance of rheology

The most important parameter in all rheological models is that of viscosity; a measure of the resistance to flow. The magnitude of the viscosity in the mantle is dependent on external variables such as pressure, temperature and effective stress, as well as the intrinsic properties of the materials present. Therefore defining the value and variation of viscosity with depth (Chapter 7) could more tightly constrain the above parameters and hence shed some light

on the mode of convection within the mantle. In the case of the lower mantle a number of questions remain unanswered, of which a few are;

What are the rheological properties of the major lower mantle mineral (Mg,Fe)SiO₃ perovskite?

What is the dominant deformation mechanism in the lower mantle?

Is lower mantle rheology Newtonian or non-Newtonian?

How does viscosity vary with depth?

How will a thermal boundary layer at 670 km depth affect the viscosity?

The work presented in this thesis is an attempt to go some of the way towards answering these questions, although the answers may still be somewhat ambiguous. This will be achieved by using a combination of experimental studies on analogue perovskites and computer modelling techniques.

In Chapter 2, theories of creep processes at high temperature are reviewed. Chapter 3 describes the experimental procedures and in Chapter 4, the results of experiments on the perovskites CaTiO₃ and NaNbO₃ are presented. Chapter 5 gives details of the computer simulation techniques used to calculate the energetics of defects and diffusion processes in the perovskites SrTiO₃, CaTiO₃ and MgSiO₃.

In Chapter 6, the rheology of perovskites is discussed and CaTiO₃ put forward as an analogue for MgSiO₃. The results of chapters 4 and 5 are then brought together in order to compile rheological data sets for both perovskites. The data for MgSiO₃ is then used in Chapter 7 to construct a viscosity profile for the lower mantle. Finally, the implications of this work for current models of mantle dynamics is discussed.

CHAPTER 2: THEORIES OF HIGH TEMPERATURE CREEP

2.1 Introduction

The plastic deformation of crystalline solids at high temperatures takes place by the process of creep, where movement on the atomic level over long timescales leads to viscous behaviour. There are a number of different mechanisms by which creep can take place, but all rely on the presence and mobility of defects within the material.

The various creep processes can be described by theoretical constitutive rate equations based on microphysical models. These equations relate the creep rate to stress and temperature. The most general form of the rate equation is (Ranalli 1987):

$$\dot{\epsilon} = f(\sigma, T, P, M, S) \quad (2.1)$$

where $\dot{\epsilon}$ is the strain rate, σ is the applied stress, T is the absolute temperature and P is pressure. M represents the physical properties of the material, and S the state variables such as grain size.

Different creep mechanisms may act singly or competitively although one will normally dominate for a given set of conditions. The dominant mechanism for creep can be found experimentally, by analysis of microstructures produced during controlled deformation, or theoretically by the use of deformation mechanism maps (Frost and Ashby 1982).

In this chapter, the creep mechanisms important at high temperatures will be reviewed along with their constitutive equations and the concepts of deformation mechanism maps and isomechanical series will be introduced.

2.2 Diffusional creep

Diffusion involves the transport of matter in response to some driving force or gradient within a crystal. Such transport can occur either by the movement of ions or atoms through the bulk of the lattice, or along surfaces such as grain boundaries, or indeed by both mechanisms simultaneously.

Diffusion through the lattice requires the presence of point defects which are formed either by the removal of an atom from a lattice site (vacancy), or by the presence of an atom at a non-lattice site (interstitial). In ionic crystals, the introduction of point defects must be balanced so as to maintain neutral charge conditions. So, for each cation vacancy there must be vacant anion site(s) with an equal and opposite charge (Schottky defects) or a cation of the same charge at an interstitial site (Frenkel defect). Defects may also occur as a result of impurities in the crystal. At lower temperatures where impurities are present, the equilibrium number of vacancies will depend on the impurity concentration. However, at high temperatures, or where the crystal contains no impurities, point defect concentrations will be dependent on temperature. These low and high temperature regimes are known as the extrinsic and intrinsic regimes respectively.

When a shear stress, σ_s , is applied to an imperfect polycrystalline material, a vacancy concentration gradient is introduced. This leads to a flow of vacancies through the bulk of the lattice and around the grain boundaries, which respectively act as sources and sinks for vacancies (Figure 2.1). This flux of vacancies, with a corresponding counter flux of atoms or ions, causes strain, and hence deformation, in the crystal grain.

The constitutive equation for diffusional creep can take two forms, depending on whether the flux of matter occurs along grain boundaries or through the bulk of the lattice. For lattice diffusion, the constitutive or rate equation is:

$$\dot{\epsilon}_{SD} = \beta\sigma\Omega D_{SD}/d^2kT \quad (2.2)$$

where $\dot{\epsilon}$ is the strain rate, β is a dimensionless constant, σ is the applied stress, Ω is the atomic volume of the diffusing species, d is the grain size, k is Boltzman's constant, T is absolute temperature and D_{SD} is the diffusion coefficient, where the subscript $_{SD}$ denotes self-diffusion. The diffusion coefficient can be described as the constant of proportionality between the flux and the driving force. It is highly dependant on temperature, and for self-diffusion through the bulk lattice is given by,

$$D_{SD} = D_0 \exp(-\Delta H/kT) \quad (2.3)$$

where D_0 is a pre-exponential factor, ΔH is the activation enthalpy for diffusion and R is the gas constant. The creep that results from this type of bulk or volume diffusion is known as Herring-Nabarro creep.

Strain or creep resulting from diffusion along grain boundaries is termed Coble creep and has a rate equation of the form:

$$\dot{\epsilon}_{GB} = \beta\sigma\delta\Omega D_{GB}/d^3kT \quad (2.4)$$

where the subscript $_{GB}$ denotes grain boundary processes. δ is the effective grain boundary width and D_{GB} the grain boundary diffusion coefficient. D_{GB} has a similar form to D_{SD} in equation 2.3. The effective grain boundary width is the width of the high diffusivity path parallel to the actual grain boundary with a thickness in the order of a few lattice spacings thickness (Frost and Ashby 1982).

Where both types of diffusion occur simultaneously, the combined form of the rate equation is:

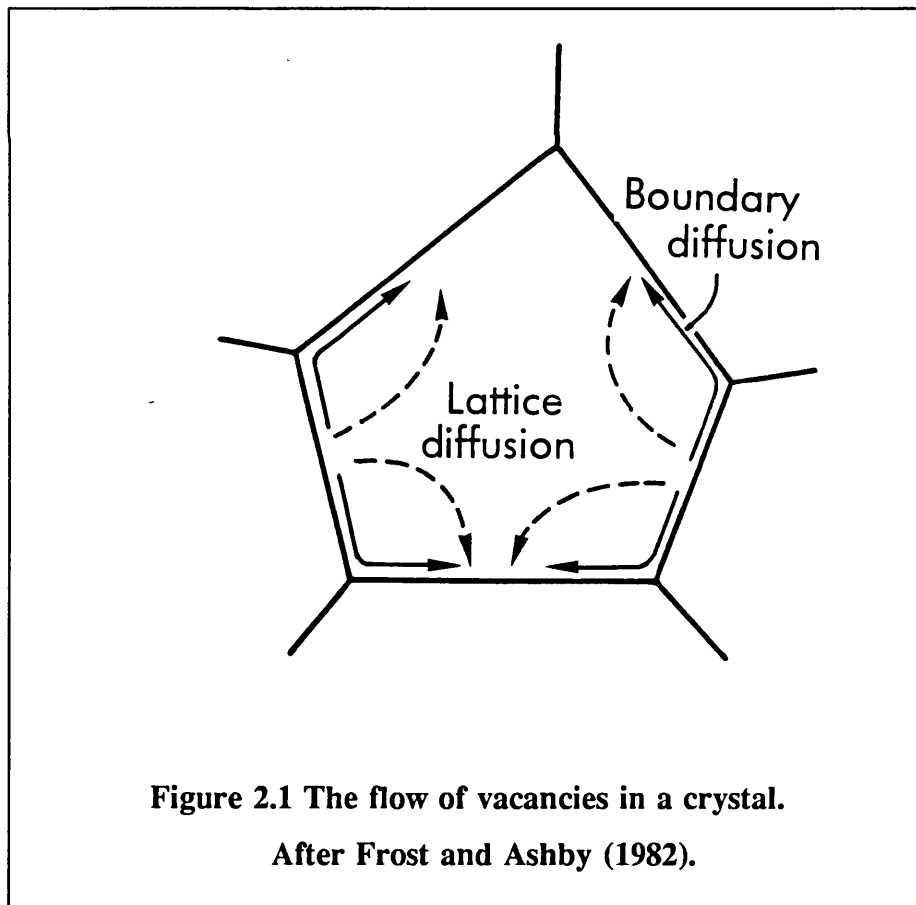
$$\dot{\epsilon}_D = (\beta\sigma\Omega/d^2kT).D_{eff} \quad (2.5)$$

where the effective diffusion coefficient D_{eff} is:

$$D_{\text{eff}} = D_{\text{SD}}[1+(\pi\delta D_{\text{GB}}/dD_{\text{SD}})] \quad (2.6)$$

At higher temperatures, lattice diffusion is normally dominant, with grain boundary diffusion becoming important at lower temperatures and/or when grain size is small.

Creep by either diffusion mechanism has the characteristics of Newtonian viscous behaviour, where the strain rate depends linearly on stress so that $\dot{\epsilon} \propto \sigma^n$ with $n = 1$.



2.3 Dislocation creep

2.3.1 Dislocations

Dislocations are line defects found in all crystalline solids with the exception of some whiskers. Their existence was proposed independently by Orowan, Polanyi and Taylor in 1934 to account for the fact that the actual strength of a crystal is far less than the theoretical strength.

When a crystal undergoes plastic deformation, it commonly does so by the process of slip, where densely packed planes in a crystal slide over each other in the manner of a pack of cards. A slip system is characterised by the plane on which slip takes place and the direction of displacement. The dislocation line represents an area of the crystal lattice which has been displaced relative to the surrounding lattice. Dislocations are characterised by line direction ζ and the displacement vector \mathbf{b} , known as the Burgers vector. Dislocations can have an edge character, where ζ is normal to \mathbf{b} , a screw character where ζ is parallel to \mathbf{b} (Figure 2.2) or some mixture of the two.

Movement of dislocations can occur either by glide, where the dislocation is constrained to move in one plane only, or by climb, which involves the diffusion of vacancies to and from the dislocation and is therefore a thermally activated process. The dislocation line climbs out of its glide plane in a series of steps known as jogs. The relationship between the strain rate and the movement of dislocations can be described by Orowan's equation:

$$\dot{\epsilon} = \rho_m \mathbf{b} \mathbf{v} \quad (2.7)$$

where ρ_m is the density of mobile dislocations and \mathbf{v} their velocity. Both density and velocity can be expressed in as a function of stress, temperature and pressure in an equation similar to equation 2.1. Orowan's equation is valid

for all types of dislocation movement.

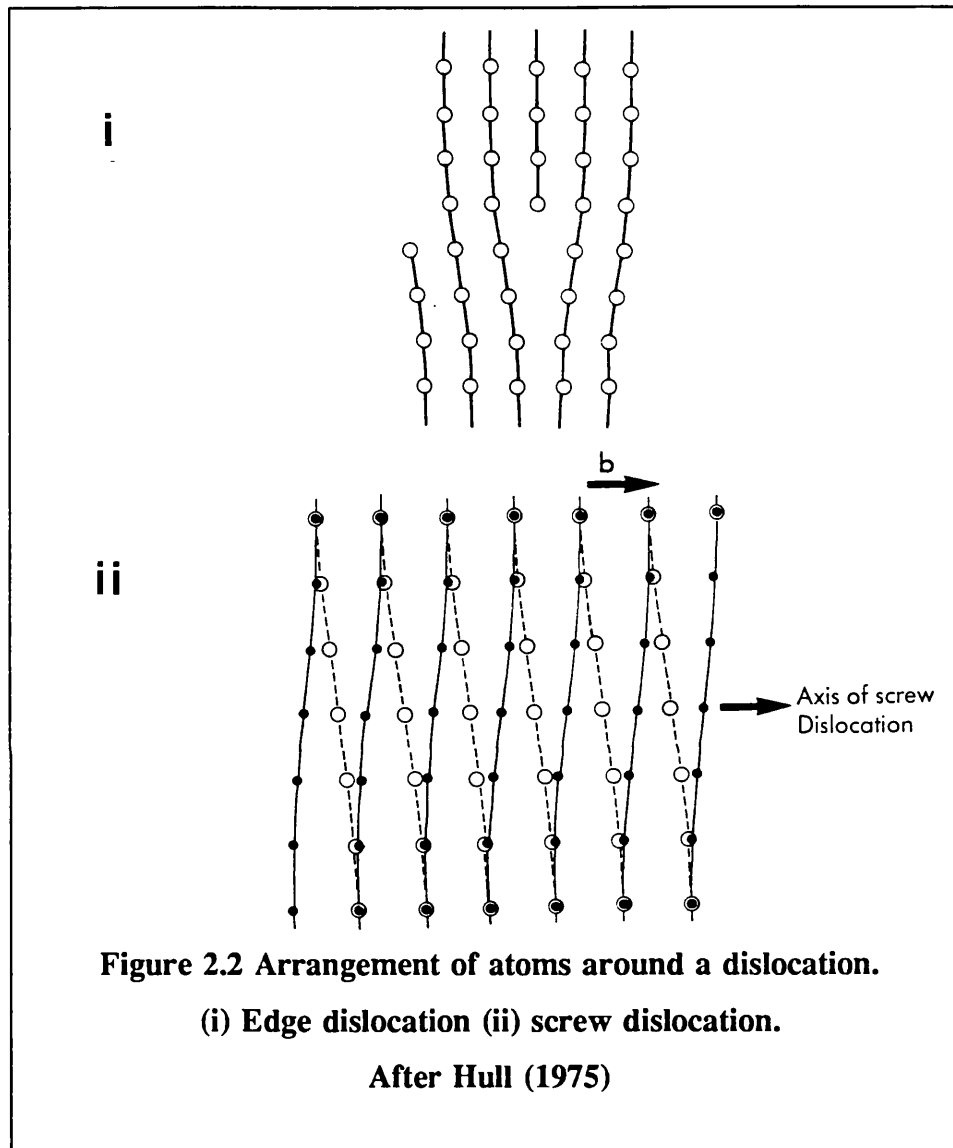


Figure 2.2 Arrangement of atoms around a dislocation.

(i) Edge dislocation (ii) screw dislocation.

After Hull (1975)

2.3.2 Power-Law creep models

The most common creep equation (Poirier 1985) takes the form

$$\dot{\epsilon}_{PLC} = A\sigma^n \exp(-\Delta Q/kT) \quad (2.8)$$

where A is a geometric constant and Q is the apparent activation energy. Strain rate is proportional to some power of σ , hence this type of behaviour is known as power-law creep. For most minerals, n has a value between 2 and 5. Equation 2.8 is known as the Dorn equation (Ranalli 1987) and is commonly used to describe the results of creep experiments on single crystals. Although Dorn's equation is very successful at describing the macroscopic behaviour during creep, it tells us nothing of what is happening at the microscopic level and for this reason cannot be extrapolated in order to predict behaviour at conditions unobtainable in the laboratory. To get away from this important limitations, rate equations based on microphysical models have been developed. Such equation can be extrapolated via the use of deformation mechanism maps (section 2.7) to a whole range of stress, temperature and strain rate conditions.

2.3.2.1 The Weertman model

The Weertman model (Weertman 1970) was put forward as a model for creep in the Earth's mantle and has the form:

$$\dot{\epsilon}_w = (AD_{SD}\mu b/kT) \cdot (\sigma/\mu)^n \quad (2.9)$$

where A is a constant relating shear stress to shear strain rate and μ is the shear modulus. The stress exponent n is generally found to be between 2 and 4.5. Strain is produced by the glide of dislocations, while the rate controlling process is taken to be the climb of edge dislocations. For climb to occur, ions must diffuse towards or away from the dislocation core, hence the need for the self diffusion coefficient for the slowest moving species to be incorporated.

As the density of mobile dislocations increases, recovery processes become important. In this model, the dominant recovery process is

annihilation of dislocations by climb of mutually trapped edge segments of the opposite sign. This climb controlled recovery creep is normally associated with the presence of dislocation networks forming subgrain boundaries.

One of the problems with this model concerns the use of the diffusion coefficient D_{SD} . It is commonly assumed that the activation enthalpy ΔH , for diffusion of the slowest moving species will be equal to the apparent activation energy for creep, Q . This may be the case for metals and some oxides, but is not so for more complex materials. For example, in $(Mg,Fe)_2SiO_4$ olivine, Si is the slowest moving species with an activation enthalpy of 390 kJmol^{-1} (Houlier et al. 1988). The experimentally determined activation enthalpy for creep however is 570 kJmol^{-1} (Kohlstedt and Ricoult 1984). This higher energy needed for creep may be due to coupled, multi-ion diffusion along the dislocation core (Jaoul 1990) or climb taking place by the formation of jogs which require more energy, or some altogether more complex process. Clearly, creep activation energy is not ruled by diffusion of the slowest moving species alone.

2.3.2.2 Cross-slip controlled creep

In the Weertman model, only the recovery of edge dislocations is considered. It assumes that screw dislocations, which cannot climb, can glide freely, but this may not be the case. Screw dislocations can split or dissociate into two partial dislocations separated by a stacking fault. When this occurs, the partials will be constrained to a particular glide plane and can easily pile up and become locked, causing a barrier to deformation. Non-dissociated screws can only move out of the glide plane by cross-slip, which is a method of recovery, but first the partials must recombine. Cross-slip is a thermally activated process, like climb, whose activation enthalpy depends on stress and possibly on pressure and stacking fault energy as well. The rate equation for cross-slip controlled creep is given by (Ranalli 1987)

$$\dot{\epsilon}_{cs} = A_{cs} v_{cs} (\Delta l_{cs}/b) \cdot (\sigma/\mu)^2 \exp(-\Delta H_{cs}(\sigma)/kT) \quad (2.10)$$

where v_{cs} is the frequency of unlocking by cross-slip and Δl_{cs} is the glide distance after unlocking. This type of recovery process may be important in the upper mantle (Poirier and Vergobbi 1978).

Both models for power-law creep however show that the strain rate will not be directly proportional to the stress as with diffusional creep, but will be a function of the stress exponent, n . Power-law creep is therefore characterised by non-Newtonian viscous behaviour.

2.3.3 Harper-Dorn creep

However, at low stresses and low dislocation densities, dislocation creep can have Newtonian characteristics. This is known as Harper-Dorn creep and has been observed in aluminium polycrystals deformed under tension (Harper and Dorn 1957). It has also been seen in the fluoride perovskite $KZnF_3$ (Poirier et al., 1983).

This type of behaviour is poorly understood, but seems to involve dislocation climb where the density of mobile dislocations is independent of stress. The rate equation is given by (Frost and Ashby 1982):

$$\dot{\epsilon}_{HD} = A_{HD} D_{SD} \rho_m \Omega/k T (\sigma/\mu) \quad (2.11)$$

where $A_{HD} = \rho_m \Omega/b$. Harper-Dorn creep may be an important mechanism at low stresses and dislocation densities of less than $10^8 m^{-2}$ as would be expected in the Earth's mantle.

2.4 Superplasticity

Superplasticity is a term used to describe softening of a material during certain types of deformation. Superplasticity occurs at high temperatures in some polycrystals with small grain size. It results in large strains and the development of a very organised microstructure. Two types of superplastic behaviour are known; structural and transformational.

Structural superplasticity involves some form of grain boundary sliding, possibly enhanced by diffusion. The model of Mukherjee (Mukherjee 1973) proposes that this sliding is controlled by the climb and annihilation of dislocations at the grain boundary.

In the model of Ashby and Verral (Ashby and Verral 1978), there is enhanced diffusion between the grains at the boundary leading to sliding. Although the bulk polycrystal is deformed, no deformation takes place within individual crystal grains. The rate equation for this type of behaviour is:

$$\dot{\epsilon} = D_{GB}\mu\Omega/kTd^2(\sigma/\mu) \quad (2.12)$$

Transformational superplasticity is much less well understood. It can occur when a crystal is repeatedly cycled through a phase transformation. Deformation is probably the result of strains set up in the crystal during transformation. This type of behaviour may be important in the Earth's transition zone where a number of phases are believed to undergo transformations (Parmentier 1981).

2.5 Dynamic recrystallization

During creep deformation, highly organised networks of subgrain boundaries can evolve which can in turn lead to partial or total

recrystallization. The subgrain boundaries comprise arrays of dislocations which produce a mismatch of just a few degrees in the lattice on either side of the array. These boundaries are constantly being created, migrated and destroyed. Complete recrystallization occurs by the rotation or sliding of these subgrains into organised structures. The size of subgrains, d^* , is dependant on stress as:

$$d^* = \mu b / \sigma \quad (2.13)$$

This relationship has been used to estimate maximum paleostresses (Mercier 1980) in naturally deformed rocks. However, there is some doubt as to the validity of this method. Dynamic recrystallization is not thought to significantly alter the creep behaviour of polycrystals, although it may lead to a slight reduction in strength (Poirier 1985).

2.6 The effects of pressure

2.6.1 The activation volume

The effects of pressure on the activation processes described above are included in the ΔH term of the diffusion coefficient where ΔH is defined as:

$$\Delta H = E + P\Delta V \quad (2.14)$$

with E being the activation energy and V the activation volume. The activation volume can be defined as the pressure dependence of the activation enthalpy:

$$\Delta V = (d\Delta H/dP)_T \quad (2.15)$$

This parameter is difficult to measure experimentally and so is often assumed to be the same as the atomic volume.

The theoretical determination of activation volumes is based on two methods (see Sammis et al. 1981). The first involves an empirical correlation between activation enthalpy and melting temperature, while the second is based around elastic models of defect structure.

The activation enthalpy can be related to melting temperature T_M , by:

$$\Delta H \approx gRT_M \quad (2.16)$$

where g is an empirical constant with a value of 18 for metals and 30 for silicates (Poirier 1985). So for the activation volume the expression is:

$$\Delta V = gR(dT_M/dP) = \Delta H(d \ln T_M / dP) \quad (2.17)$$

This relationship has been found to be valid for metals, but for more complex structures, ΔV is systematically overestimated (Poirier 1985).

Models based on elasticity assume that the strain energy produced by the introduction of point defects will be either dilational (Zener 1942) or shear (Keyes 1963). For the shear model:

$$\Delta V = \Delta H \{ (d \ln \mu / dP)_T - 1/K_T \} \quad (2.18)$$

where K is the isothermal bulk modulus defined in terms of atomic or molecular volume as:

$$-1/K = d \ln \Omega / dP \quad (2.19)$$

Keyes' model has been shown to lead to an underestimation in ΔV , while the corresponding dilational model of Zener gives a slight overestimation. Sammis et al. (1981) take the values of Keyes' and Zener's models to be representative of upper and lower limits respectively.

However, all models are strictly applicable only to creep processes that are rate controlled by diffusion. The estimation of activation volume for dislocation creep models not controlled by diffusion are likely to be even more uncertain.

2.6.2 Material parameters

In addition to activation volume, the material parameters will also change with pressure. The pressure dependence of elastic moduli can be calculated with some confidence using an appropriate equation of state, such as the Murnaghan equation, while those of structural parameters such as the Burgers vector can be determined using linear elastic theory.

2.7 Deformation mechanism maps and isomechanical series

Provided that the parameters in the rate equations are well known, the type of creep behaviour for any material under given conditions of stress, temperature, grain size etc. can be deduced from deformation mechanism maps. Such maps can be used to extrapolate the creep fields to conditions far beyond those obtainable in the laboratory. This makes them a particularly useful tool for the investigation of materials occurring in the Earth's mantle where flow processes occur over very large timescales and strain rates are of the order of $10^{-15} \text{ sec}^{-1}$. However, inferences made from extrapolated data must be treated with caution since mechanisms other than those considered in the extrapolation may operate at extreme conditions.

Information from laboratory experiments can be combined with the constitutive rate equations to define a three-dimensional deformational space with axes of variables such as temperature, stress and strain rate. Pressure is not considered directly, but through its effects on the volumetric material parameters. A two-dimensional slice of this space constitutes a deformation

mechanism map (Figure 2.3). The maps are divided into fields by boundaries separating one mechanism from another, and within each field, except close to the boundary, the total strain rate will be due to one mechanism only.

The most common maps are those in normalized stress - temperature space with contours of constant strain rate (Frost and Ashby 1982). However, it is also possible to construct maps with contours of constant viscosity and axes of stress and grain size (Ranalli 1982).

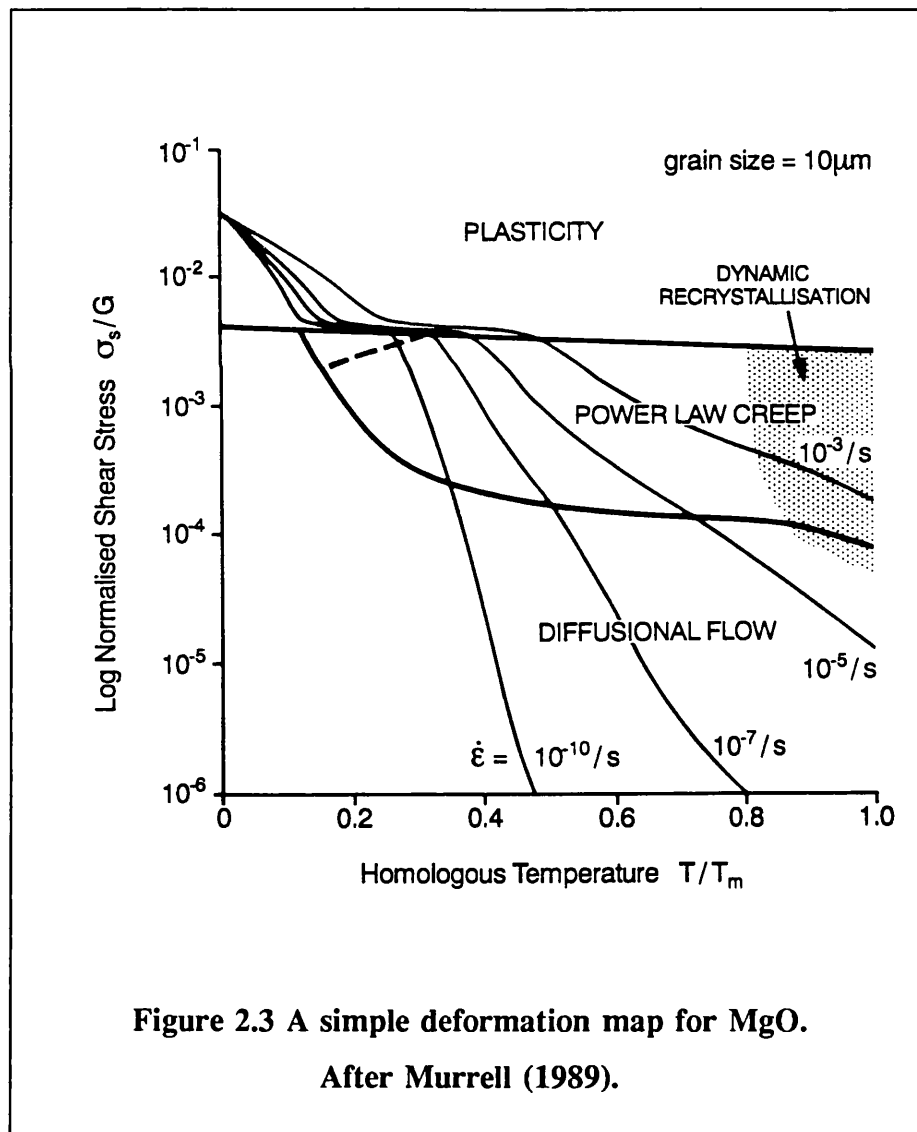


**Figure 2.3 A simple deformation map for MgO.
After Murrell (1989).**

Central to the idea of deformation mechanism maps is the concept of normalizing the chosen axes in order to make them dimensionless, thereby highlighting the intrinsic similarities and differences between groups of materials. Normalization of the maps can be handled in one of two ways. The first is by empirically normalizing the data itself, and the second is by normalizing the constitutive equations. (See Frost and Ashby (1982) for a full discussion.) The normalizing parameters used can be roughly divided into those based on temperature (eg T/T_M), those which are modulus based (eg σ/σ_0) and those based on energy parameters (eg $\Delta H/\Omega$).

If a group of solids shows similarities in mechanical behaviour when normalized and plotted on a deformation mechanism map, then they can be said to belong to an isomechanical series or group. The known behaviour of one member of the group can then be used to constrain some unknown properties of other members of the same group. For example, Frost and Ashby (1982), show that f.c.c. metals all belong to one isomechanical group, while materials with the rocksalt structure form four different groups. This highlights the fact that chemistry and bonding as well as structure will be important in defining isomechanical behaviour.

2.8 Summary

High temperature deformation of crystalline solids takes place by the movement of point defects and dislocations within the crystal. Creep mechanisms can be roughly divided into those which are diffusion dependant and those which are dislocation dependant.

Experiments on single crystals can be adequately described by the Dorn equation (Equation 2.8) although it does not describe the atomistic processes involved. The limitations of Dorn's equation can be circumvented by using constitutive rate equations derived from microphysical models.

- Deformation mechanism maps provide a useful way of displaying creep behaviour and can be used to show the similarities and differences between materials and so help to define isomechanical groups.
-

CHAPTER 3: HIGH TEMPERATURE CREEP EXPERIMENTS

3.1 Introduction

In order to model the rheology of the lower mantle it is necessary to understand the rheological behaviour of the phases present. All models agree that (Mg,Fe)SiO₃ perovskite makes up at least 70% of the lower mantle and therefore this material is virtually certain to control flow behaviour. Because of the high pressures and temperatures needed to enter the stability field of (Mg,Fe)SiO₃ perovskite, in situ rheological experiments of the type necessary to directly determine flow properties are at present beyond the limits of technology.

One alternative to direct experiments is to use the analogue approach, where the trends shown by suites of materials with the same structure but differing chemistries, can be extrapolated to predict the behaviour of the material of interest. In some cases it is possible to define an isomechanical series (section 2.7) with members of the same series showing similarities in their creep behaviour.

To use this approach for (Mg,Fe)SiO₃ perovskite, the following questions need to be answered:

- 1) what are the creep properties of perovskites?
- 2) do they represent an isomechanical series?
- 3) if not, which perovskite, if any, will be the most suitable analogue for MgSiO₃?

A large number of materials with the perovskite structure are stable at ambient conditions, although few have been rigorously investigated for their

creep behaviour. Previous single crystal studies have been carried out on KZnF_3 (Poirier et al. 1983) and on the oxide perovskites BaTiO_3 (Beauchesne and Poirier 1989), KTaO_3 and KNbO_3 (Beauchesne and Poirier 1990).

The aim of the experiments reported here was to investigate the creep behaviour of CaTiO_3 and NaNbO_3 with a view to trying to answer the questions posed above.

3.2 Samples

3.2.1. CaTiO_3

The mineral perovskite, CaTiO_3 , is a 2-4 perovskite and is orthorhombic at room temperature with the space group Pbnm . The unit cell is distorted from the ideal cubic structure (Figure 3.1) by a 12° rotation of the TiO_6 octahedra about the trigonal axis. The cell parameters and known physical properties, as determined from experiment, are given in Table 3.1.

Ideally, creep experiments should be carried out on synthetic crystals where the chemistry can be carefully controlled. However the high melting temperature of CaTiO_3 , 2248K, makes growth from a melt both difficult and expensive. As a result of this, all of the experiments on CaTiO_3 reported here have been performed on natural samples.

The mineral perovskite is commonly found in nature as an accessory mineral present in some alkaline igneous rocks and in skarns. Single crystals occur as octahedra and cubes and can have dimensions of up to several centimetres. Substitutions in both cation sites are common, and consequently, natural perovskites can have large deviations from ideal stoichiometry.

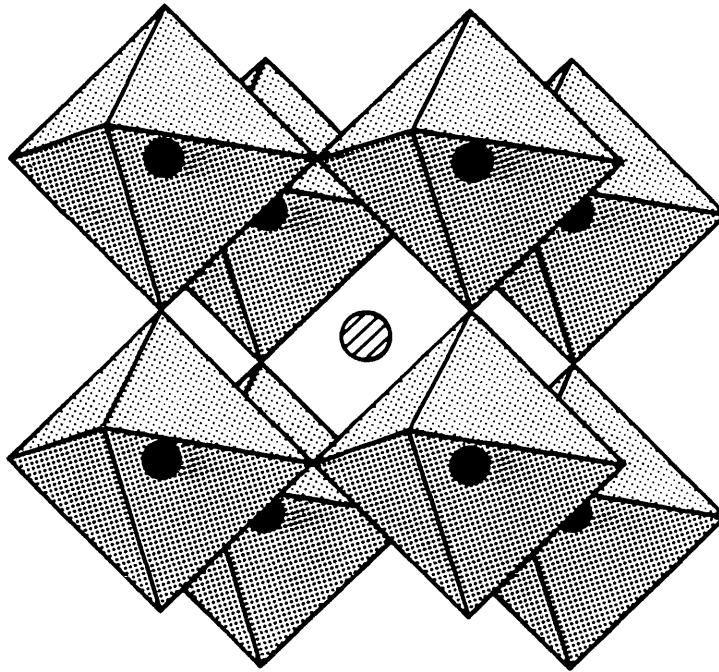


Figure 3.1 The ideal perovskite structure.
After Megaw (1973).

The CaTiO_3 samples used in these experiments were cut from a crystal from the Ural Mountains, U.S.S.R. that was kindly donated by the Natural History Museum London (sample number BM 1909 381).

Probe analysis was carried out prior to experiments, to assess sample purity, using the Hitachi S-2500 scanning microscope in the Mineralogy Department, Natural History Museum. The results of these analyses are given in Table 3.2.

Impurities were found only along microcracks, present as crystallites of sphene, iron oxides, clinocllore and an unidentified iron silicate phase. The bulk of the samples were extremely pure and homogeneous.

Table 3.1. Structure and properties of CaTiO₃ and NaNbO₃ at ambient conditions.

	CaTiO ₃	NaNbO ₃
a Å	5.367 ⁽¹⁾	5.568 ⁽²⁾
b	7.644 ⁽¹⁾	15.518 ⁽²⁾
c	5.444 ⁽¹⁾	5.505 ⁽²⁾
vol Å ³	223.34 ⁽¹⁾	475.65 ⁽²⁾
K GPa	177 x10 ³ ⁽³⁾	?
μ GPa	104 x10 ³ ⁽³⁾	?
T _m K	2348.0 ⁽²⁾	1685.0 ⁽²⁾

References: 1. Kay and Bailey (1957) 2. Landolt - Börnstein (1981)
3. Liebermann et al. (1977)

Table 3.2. Probe analyses of CaTiO₃.

1) Bulk sample. 2) Fe-silicate in cracks.

Element	Oxide % (1)	Oxide % (2)
TiO ₂	57.857	00.165
CaO	41.186	00.443
FeO	00.556	41.024
SiO ₂	00.251	55.150
Al ₂ O ₃	00.051	00.196
MgO	00.075	00.606
Ce ₂ O ₃	00.230	00.000
Na ₂ O	00.000	00.496
MnO	00.000	00.132
K ₂ O	00.000	01.788
Total	100.206	100.0

3.2.2 NaNbO₃

NaNbO₃ is a 1-5 perovskite and is orthorhombic at room temperature. It exhibits a number of distinct phase transformations at various temperatures, three of which are orthorhombic. At temperatures above 693K, NaNbO₃ becomes pseudo-tetragonal; at 833K tetragonal; and cubic at 873K (Landolt and Börnstein 1977). It is more distorted from the ideal structure than CaTiO₃, with the NbO₆ octahedra being both rotated and tilted. This leads to displacement of the Nb cation, as well as the oxygens. The cell parameters and physical properties are given in Table 3.1.

The samples used here were grown from a melt by S. Beauchesne (Beauchesne 1989) and donated by J.P. Poirier. Their composition is given as Na_{0.993}Nb_{1.0025}O_{3.004} (Beauchesne 1989).

3.3 The creep apparatus

A diagram of the basic assembly of the creep apparatus is given in Figure 3.2. The sample (1) is compressed between two rams (3,4) of polycrystalline alumina (99.9% Deranox). Attached to them are two anvils (2) of single crystal alumina oriented with their c-axes parallel to the compression axis to prevent basal glide. The lower ram (3) is fixed, while the upper ram (4) is mobile and can be adjusted by means of glide rollers (5) to ensure that the ram runs parallel.

The static load is applied via the lever arm (7) which multiplies the dead load (8) by a factor of five times. The lever arm and upper ram assembly are prevented from applying any load themselves by means of counter balance weights (6,9).

The Carbolite 1kW tube furnace (10) is capable of achieving a

maximum temperature of 1973K. It can be moved up along the supports (11) so that the sample (1) can be located at the "hot spot" position. A pyrophyllite ring is attached to the base of the furnace and alumina wool wrapped around the top to reduce air-flow and convection within the furnace tube. Temperature is controlled by a Eurotherm 3-term controller which can be adjusted to produce a smooth heating curve and reduce temperature fluctuation.

A type R Pt:Rh mineral insulated thermocouple (14) is used to measure temperature at the sample. This was purchased with a grant from the London University Central Research Fund. The thermocouple is fixed to the top plate of the apparatus to ensure that the sensor is always at the correct position. Temperature at the sample is displayed on a RKC AF-48 readout unit connected to the thermocouple. In addition the thermocouple is connected to a TCS conditioning unit which linearly amplifies the signal to the range 0 - 10 volts for data-logging purposes.

Changes in length of the sample are measured by a Sangamo AC linear variable differential transducer (LVDT) which has a range of -1 to +1 volts over 1mm of displacement. The LVDT core is attached to a 3mm diameter polycrystalline alumina rod (16) (97% Deranox) while the sensor (15) is fixed to the upper ram assembly. The alumina rod rests atop the fixed lower ram so that as the sample is compressed and the upper ram moves down, the LVDT measures the displacement between the two. Use of the alumina rod compensates for any displacement due to thermal expansion or contraction of the rams during an experiment. The linear thermal expansion coefficients of the rams and rod are $8.5 \times 10^{-6} \text{K}^{-1}$ and $8.2 \times 10^{-6} \text{K}^{-1}$ respectively. Therefore, the displacement measured will be almost entirely due to changes in sample length.

The LVDT is connected to a C31 conditioning unit which amplifies the signal to a range of -10 - +10 volts. The unit has a digital readout so that the progress of deformation can be easily monitored during an experiment.

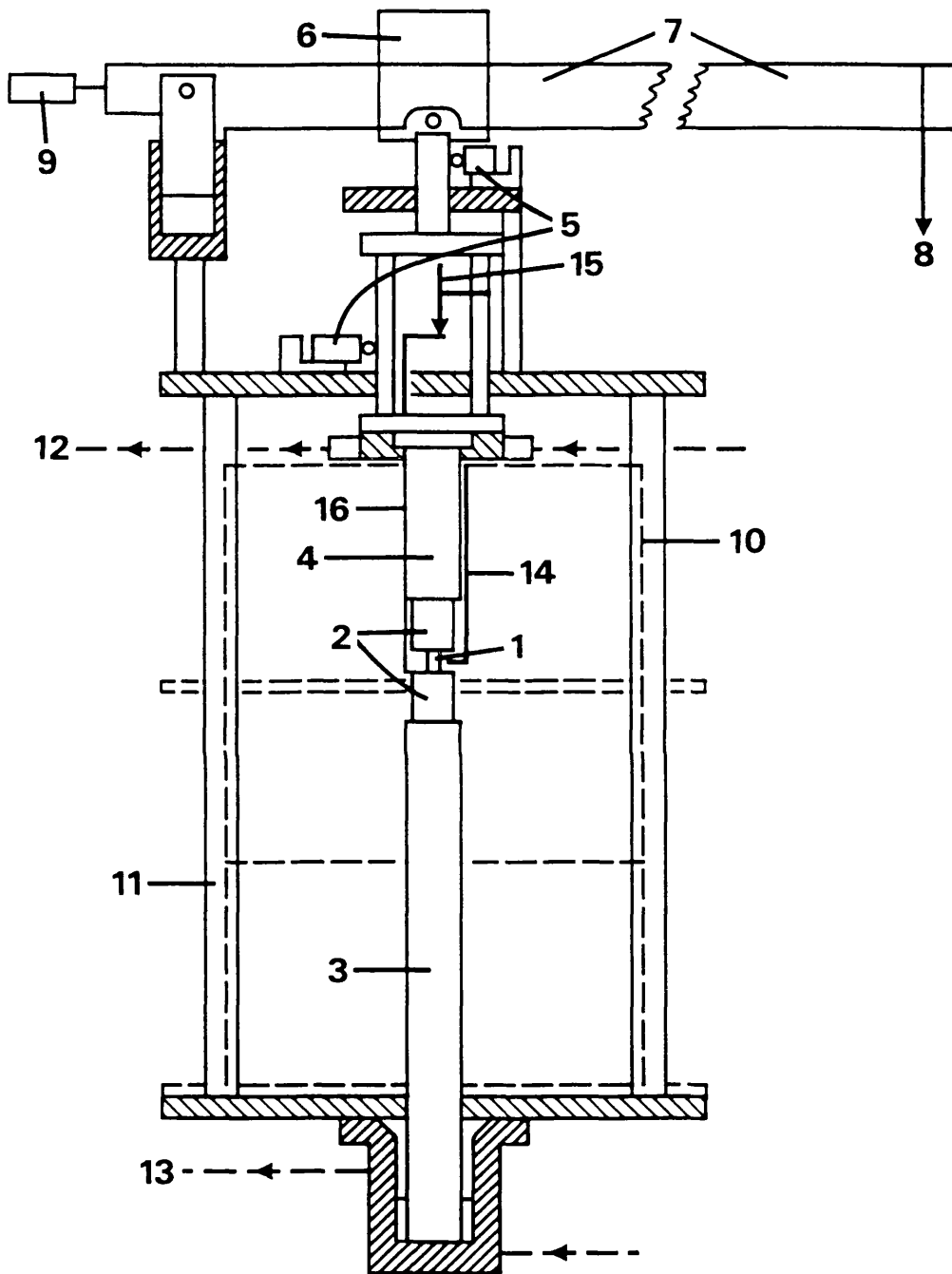


Figure 3.2 Schematic diagram of the creep apparatus.
Not to scale. Numbers are referred to in the text.

Both the upper and lower rams are cooled by water running through brass/copper cooling rings (12,13). The whole apparatus is mounted on an optical bench to minimise vibration from outside sources.

Output from the thermocouple and LVDT conditioners are converted to a digital signal by a 12 bit OASIS MAD12 data acquisition unit. The data are collected and stored on disc using a BBC Master computer running OASIS data logging software.

3.4 Calibration procedures

3.4.1 Calibration of the furnace

The furnace was calibrated to assess the temperature gradients within the tube, to find the position of the 'hotspot' and to find the relationship between control temperature and sample temperature. To find the gradient along the length of the furnace, a thermocouple was placed at different positions in the furnace and measurement after equilibrium noted. This was carried out for set temperatures of 1073K, 1273K, 1673K and 1973K. The results, shown in Figure 3.3, give the hotspot position as approximately 10 cm from the top of the furnace.

In order to measure the temperature gradient across the furnace at the hotspot position, the temperature was read simultaneously by two thermocouples, one at the sample position and one at the side of the furnace tube. At 1273K, the difference between the two readings was found to be 6 degrees. At 1763K this temperature difference had fallen to 3 degrees.

No straightforward correlation was found between set temperature and sample temperature. Factors such as room temperature were found to affect the relationship between the two.

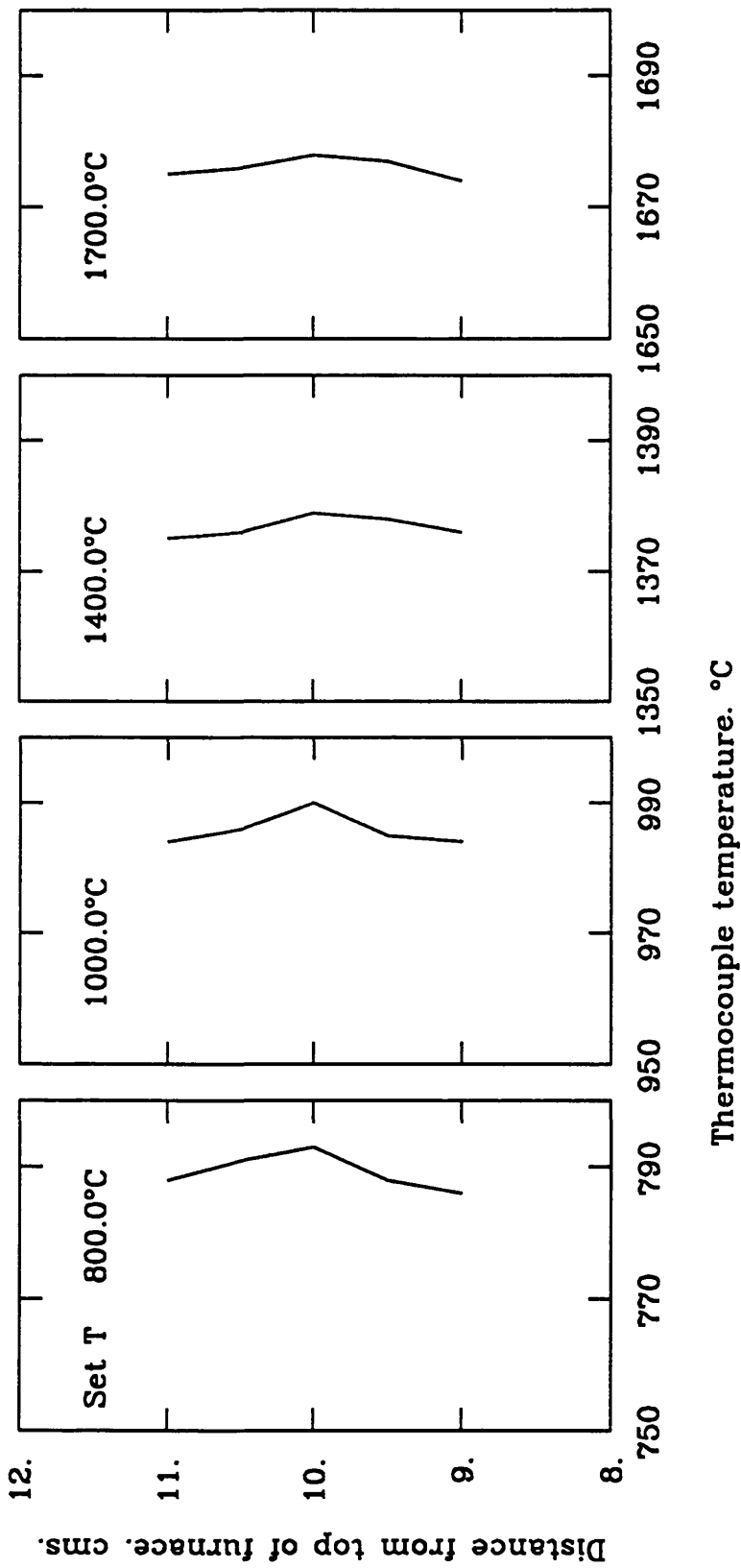


Figure 3.3 Temperature gradients along the furnace length for a range of set temperatures.

3.4.2 Calibration of the LVDT

A series of runs were carried out to assess the effect of ram thermal expansion on the measurement of change in length of a sample. All runs were performed without sample or load.

In the first run, the furnace was set to 1773K and run for 24 hours with the LVDT sensor attached to the mobile upper ram system. The same conditions were then repeated for a second run with the LVDT sensor attached to the alumina rod. The resulting plots (Figure 3.4) show just how effective the rod is in eliminating the 'noise' produced by length fluctuations of the rams due to temperature fluctuations in the laboratory.

3.5 Methodology

3.5.1 Sample preparation

Samples were cut into rectangular prisms of average dimensions 2x2x3mm using a diamond saw. The samples were embedded in Araldyte and the top and base polished with progressively finer grades of carborundum and, lastly, with 6um diamond paste.

After polishing, the bulk of the Araldyte was cut away and the remainder dissolved in TAAB resolve. Finally the samples were cleaned by immersing in an acetone sonic bath for 5 minutes.

3.5.2 Sample orientation

In all references to sample orientation in this and the following chapter, the axes used to describe planes and directions in perovskites will be the pseudo-cubic axes where $a_{pc} \approx b \approx a\sqrt{2} \approx c\sqrt{2}$.

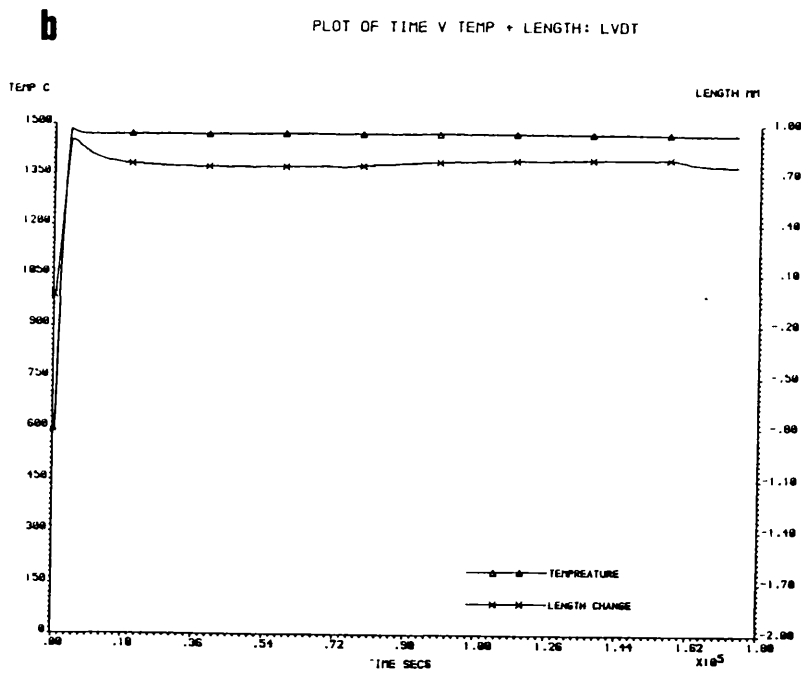
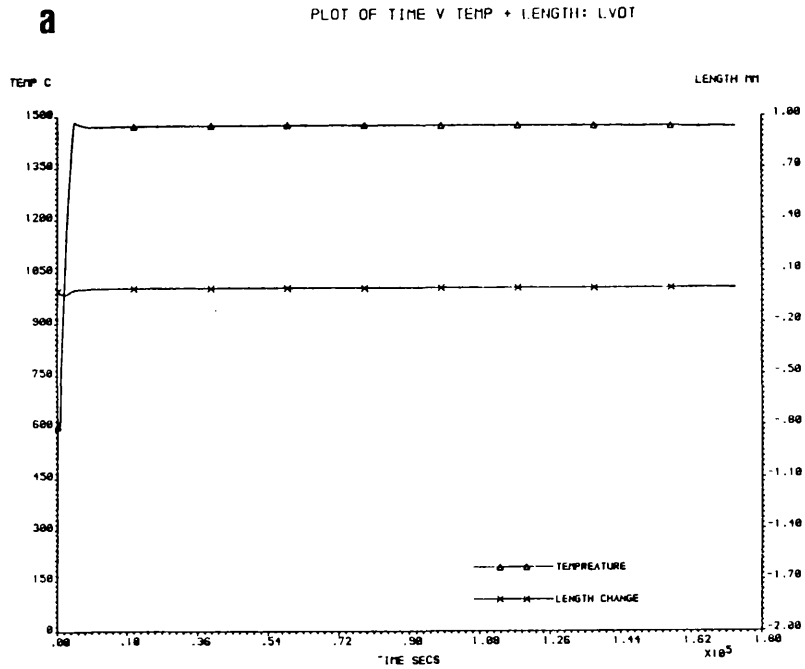


Figure 3.4 Plots of length change with time:

a) without the alumina rod

b) with the alumina rod

The samples of CaTiO_3 were cut from a large single crystal with a cubic habit, whose crystal faces were of the $\langle 100 \rangle$ pseudo-cubic type. One set of samples was cut with edges parallel to the crystal face and another at 45° to the face. Thus the long axes of the samples were the $\langle 100 \rangle_{\text{pc}}$ and $\langle 110 \rangle_{\text{pc}}$ directions respectively.

The NaNbO_3 crystals contained two sets of perpendicular cracks, probably the result of twinning and subsequent strain cracking along the twin composition planes with cooling. Small samples were cut with edges parallel to these cracks. X-ray rotation photographs were taken to determine the orientation of these crystals. However, because of the extensive twinning, a large number of spots were present. The spacing of the layer lines indicated that the rotation axis was one or more of the pseudo-cubic axes.

3.5.3 Calculation of applied stress

The applied stress is related to the load by:

$$\sigma = F/A \quad (3.1)$$

where the force F is equal to the mass multiplied by the acceleration due to gravity and A is the area to which the force is applied. It is assumed that the sample deforms by shear during an experiment, i.e. there is a change in shape without a change in volume. This will lead to a progressive change in the area A . Since this change in A cannot be measured, there will be an error in stress. This error obviously depends on the total strain produced in the sample during an experiment, but was generally of the order of 10%.

3.5.4 Experimental procedure

At the start of each experimental run, the sample was placed between the anvils with thin Pt. foil interposed between sample and anvils at each end

to avoid diffusion between them. The furnace was then raised and set to achieve a predetermined temperature. Once thermal equilibrium had been reached, usually about 2 hours, the load was applied. Temperature and length were then logged at regular intervals of 100 to 300 seconds throughout.

The majority of experiments were performed at constant temperature with increments of stress being made when the quasi steady-state creep regime was assumed to have been reached. Where constant stress tests were carried out, the load was removed when increments of temperature were made and not re-applied until thermal equilibrium had again been reached.

At the end of each run, the furnace was turned off and the load removed. Samples were allowed to cool slowly before being removed for observation under the microscope.

3.6 Analysis of data

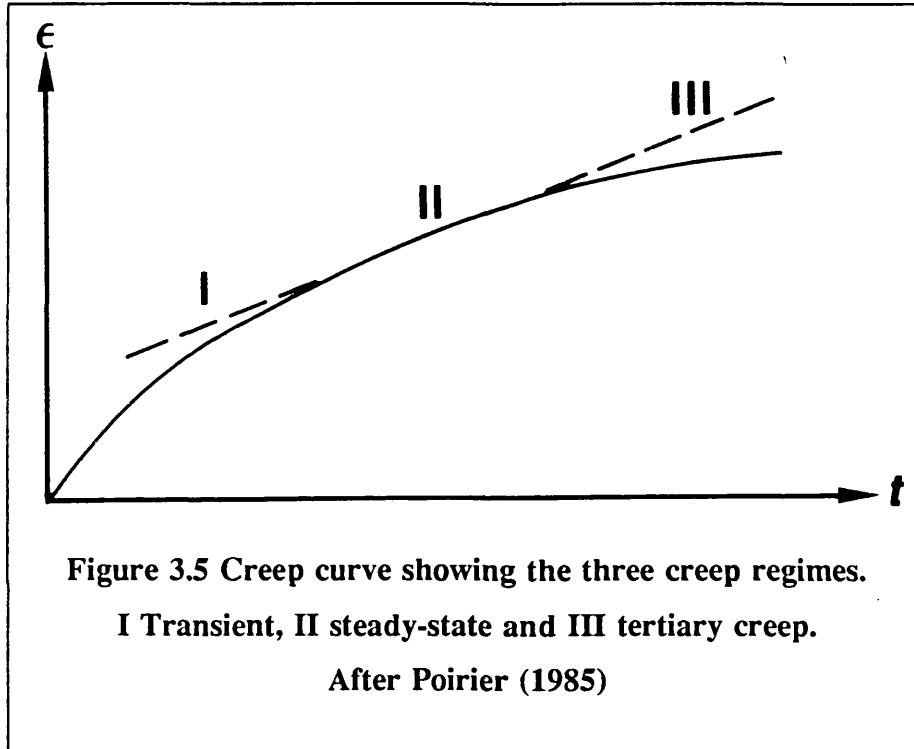
The length change values collected during an experiment are used to calculate the value of true strain ϵ :

$$\epsilon = \ln[1 - (\Delta l_t / l_0)] \quad (3.2)$$

where Δl_t is the change in length at time t and l_0 the original length. Strain is then plotted against time to give creep curves as shown in Figure 3.5. Creep curves can be divided into a primary or transient regime, where the creep rate decreases with time, and a quasi-steady-state regime where the strain rate remains constant for a given stress and temperature. If the creep test continues for a sufficient period of time, the tertiary regime is entered, which eventually leads to failure.

The steady-state regime will correspond to the straight line portion of the creep curve. However, it is often difficult to assess when steady state has

been reached just by examination of the creep curve. A more reliable method is to plot strain rate against true strain; if the strain rate tends asymptotically to a constant minimum, this can be taken as the steady-state creep rate (Poirier 1985).



Once the strain rate for a given stress and temperature range is known, the data are then fitted to a Dorn type creep law:

$$\dot{\epsilon} = \ln A \cdot \sigma^n \cdot \exp(-Q/RT) \quad (3.3)$$

The values of stress exponent, n , and apparent activation energy, Q , can be estimated from the slopes of Arrhenius plots of $\ln \dot{\epsilon}$ vs $\ln \sigma$ and $\ln \dot{\epsilon}$ vs $1/T$ respectively. However, this method is not without limitations. Each Arrhenius plot is constructed for constant temperature or constant stress and the slope

found by linear regression of the data points. The resulting values of n and Q for different stress-temperature regimes may not correlate well. Additionally, if only a few data points are available for a particular stress or temperature then the results obtained are at best dubious. (For a full discussion of these problems see Poirier et al. 1989)

In order to obtain a better fit to the creep law, a generalized non-linear global inversion technique, developed by Sotin and Poirier (1984), was used. The inversion code calculates the values of Q , n and A from the values of stress, temperature and strain rate for each experiment within defined error limits. The residuals are then calculated as the difference between the original and inverted data. The value of these residuals and the number of iterations needed for convergence give a good indication of the quality of the data and the suitability of the creep law chosen. High values of residuals may point to inconsistencies in experimental conditions and in such cases, data points have been rejected from the final inversion.

3.7 Transmission Electron Microscopy

The dislocation structure of deformed samples were examined using a Jeol 200 CX transmission electron microscope (TEM) with an accelerating voltage of 200 kV at the Department of Crystallography, Birkbeck College London. Additional observations were carried out at the Institute du Physique du Globe, Paris, on a Jeol 1200 EX TEM.

3.7.1 General description of TEM

The TEM produces a magnified image of a thin sample by means of an electron gun and a series of electromagnetic lenses. A simplified diagram of the ray paths taken by the electrons is shown in Figure 3.6.

The electron gun produces a beam of electrons which are accelerated by a high voltage and focused onto the specimen by the condenser lens. The image is focused by the objective lens and then magnified by the diffraction and intermediate lenses before being projected onto a viewing screen. The screen can be raised so that the image or diffraction pattern can be recorded onto film.

A series of apertures can be inserted into the path of the beam which control the degree of illumination (condenser aperture), and the number of beams which contribute to the final image (objective aperture). The diffraction pattern, formed in the back focal plane, is projected onto the viewing screen by adjustment of the diffraction lens and the selected area aperture. The specimen sits in a holder which can be tilted about two axes normal to each other and the optic axis of the microscope.

3.7.2 TEM techniques

The TEM can produce either a diffraction pattern or one of several types of image on the viewing screen. The most common imaging mode is termed bright field, and is produced by inserting the objective aperture into the path of the beam so that only the central (transmitted) beam is allowed through. To reduce complexity of the image, the specimen is usually tilted in such a way that only one diffracted beam exactly satisfies the Bragg condition and only this and the transmitted beam form the diffraction pattern. This is the two beam imaging method. If the objective aperture allows only the diffracted beam through, then the resulting image is termed dark field.

Around the dislocation, the lattice planes are bent. A beam striking the bent planes will be reflected at a slightly different angle to those interacting with the perfect crystal and it is this phase difference which causes the dislocation to be visible. A bright spot on the diffraction pattern, which satisfies the Bragg condition, will contain information from a large number of

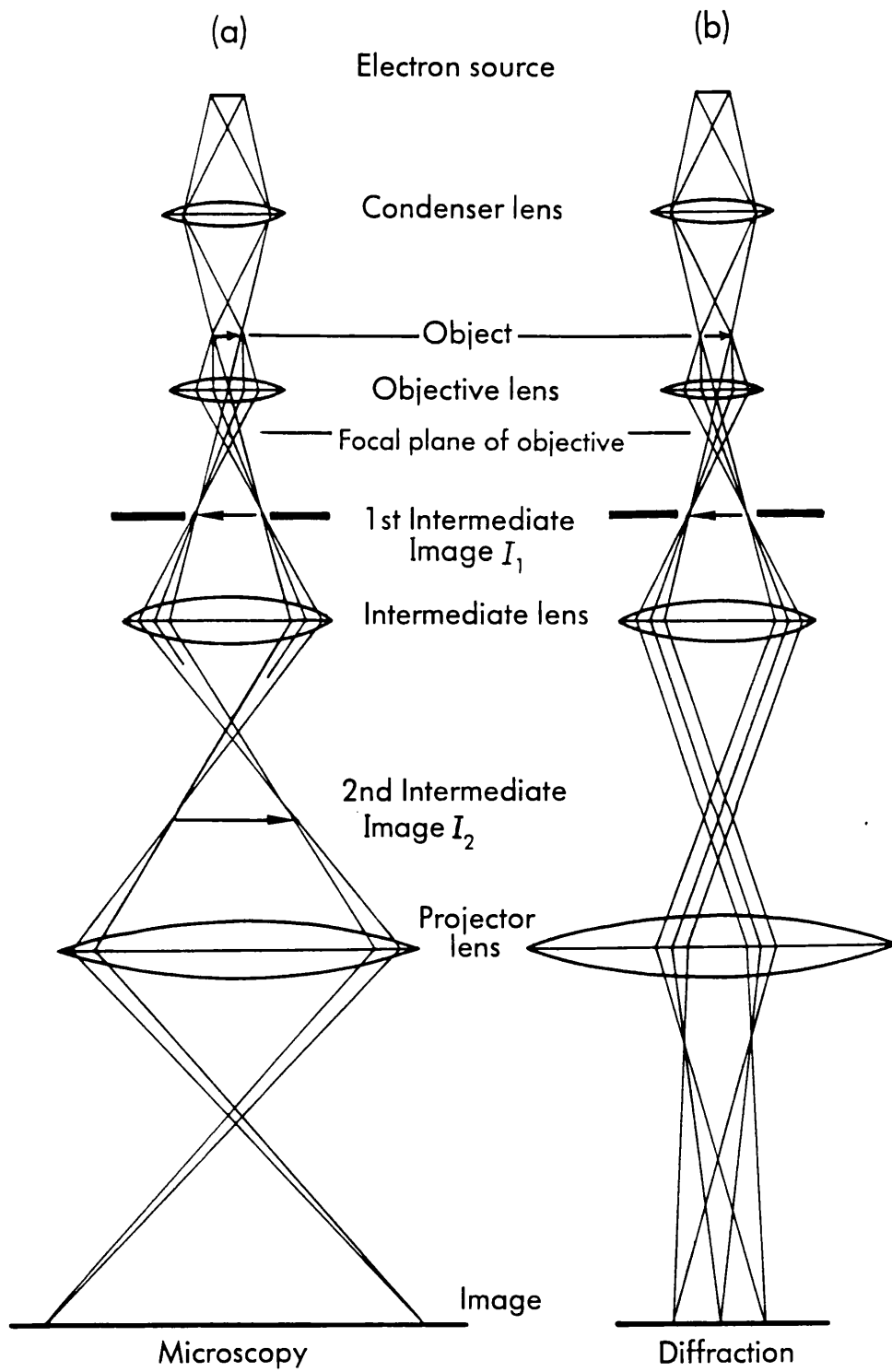


Figure 3.6 Ray diagram of the transmission electron microscope.

planes and hence the dislocation often appears as a diffuse line. If however, the image is formed using a diffracted spot which is far from the Bragg angle, then the image will be much sharper, since the spot will contain information from only a few planes around the dislocation core. This 'weak beam' microscopy is particularly useful for examination of partial dislocations.

A more rigorous discussion of the methods described above can be found in Mineralogical Society of Canada: Short Course in Applications of Electron Microscopy in the Earth Sciences (White 1985)

3.7.3 Sample preparation

After deformation, samples were made into standard 30 μm thin sections. A Ti grid was glued onto the thin section using Araldyte and then the grid and sample removed and thinned using an Ion Tech ion beam thinner.

The sample was first thinned with the ion beam at an angle of approximately 27° until a hole appeared. Final etching was carried out with the beam angle of 14° . The resulting thin foil was then coated with a layer of carbon to avoid build up of charge in the microscope.

CHAPTER 4: EXPERIMENTAL RESULTS

4.1 Experimental conditions

All of the experiments in this study were carried out under uniaxial, unconfined compression in air. Samples of CaTiO_3 and NaNbO_3 were deformed under a range of stress and temperature conditions which are summarized in Table 4.1.

Table 4.1 Experimental conditions

	T/T_m	σ MPa	$\dot{\epsilon}$ sec ⁻¹
CaTiO_3 $\langle 100 \rangle$	0.67 - 0.78	19 - 117	10^{-5} - 10^{-8}
CaTiO_3 $\langle 110 \rangle$	0.67 - 0.78	20 - 70	10^{-5} - 10^{-7}
NaNbO_3	0.70 - 0.98	28 - 83	10^{-6} - 10^{-8}

4.1.1 Experiments on CaTiO_3

26 runs were performed on CaTiO_3 crystals oriented such that the applied stress was parallel to the $\langle 100 \rangle_{pc}$ axis. The results are given in Table 4.2. Typical creep curves (Figure 4.1) were constructed from the time-length data using the procedure outlined in section 3.6. The full set of creep curves for all experiments can be found in Appendix 1.

In general, the creep curves show a fast transitory stage followed by quasi steady-state behaviour. However, plots of strain versus strain-rate indicated that the quasi steady-state regime had not been reached in runs 17A, 18B and 27. Consequently, these results were discarded. Samples 23 and 31 failed shortly after loading, while samples 19 and 26 did not show any significant deformation. These results were also discarded.

Table 4.2 Results of experiments on CaTiO₃ with stress parallel to <100>_{pc}

Run	T C	S MPa	%	t mins	$\dot{\epsilon}$ sec ⁻¹
PVCA17A	1289	57.8	4.3	200	1.74x10 ⁻⁶
PVCA17B	1289	69.4	8.3	1040	5.70x10 ⁻⁷
PVCA17C	1289	92.5	11.2	420	1.14x10 ⁻⁶
PVCA18A	1229	58.4	4.5	1150	3.54x10 ⁻⁷
PVCA18B	1229	82.9	6.0	300	2.79x10 ⁻⁷
PVCA18C	1229	117.0	8.0	175	1.36x10 ⁻⁶
PVCA20A	1402	50.3	3.0	1190	3.04x10 ⁻⁷
PVCA20B	1402	66.0	5.5	350	8.65x10 ⁻⁷
PVCA21	1454	28.5	6.0	256	1.87x10 ⁻⁶
PVCA22A	1289	50.0	3.5	1300	1.23x10 ⁻⁷
PVCA22B	1341	50.0	6.0	1410	3.42x10 ⁻⁷
PVCA22C	1391	50.0	12.6	273	8.86x10 ⁻⁷
PVCA23	1234	75.0			Failed
PVCA24A	1407	50.6	5.0	183	2.17x10 ⁻⁶
PVCA24B	1429	50.6	7.6	67	5.78x10 ⁻⁶
PVCA25A	1398	19.4	2.0	1420	1.50x10 ⁻⁷
PVCA25B	1398	28.6	2.0	306	3.14x10 ⁻⁷
PVAC25C	1398	34.3	2.0	100	3.47x10 ⁻⁷
PVCA27	1347	60.0	45.0	150	2.10x10 ⁻⁵
PVAC28A	1328	48.0	5.0	321	8.83x10 ⁻⁷
PVAC28B	1346	48.0	6.0	130	9.86x10 ⁻⁷
PVCA28C	1378	48.0	7.0	146	5.13x10 ⁻⁶
PVAC29A	1391	57.6	14.0	238	3.29x10 ⁻⁶
PVAC29B	1424	57.6	15.5	75	3.29x10 ⁻⁶
PVCA30	1431	39.6	9.3	180	2.82x10 ⁻⁶
PVAC32	1443	35.5	8.3	435	2.05x10 ⁻⁶
PVCA33	1480	40.5	7.9	243	4.5x10 ⁻⁶

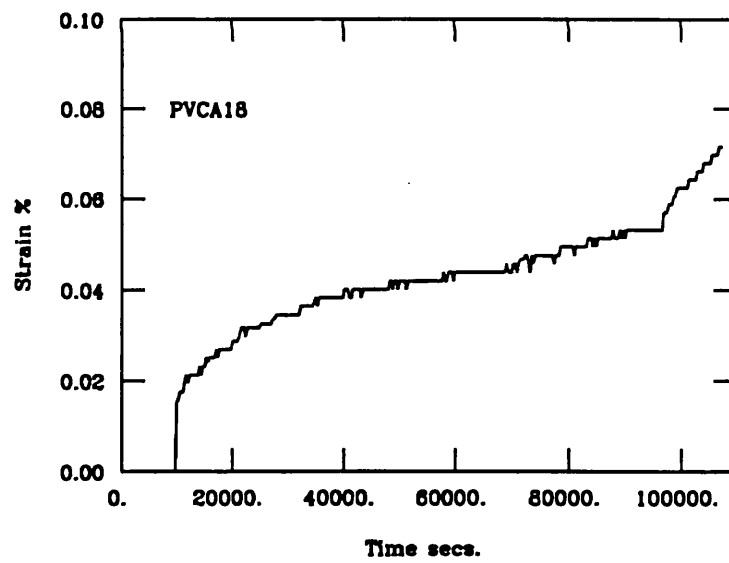
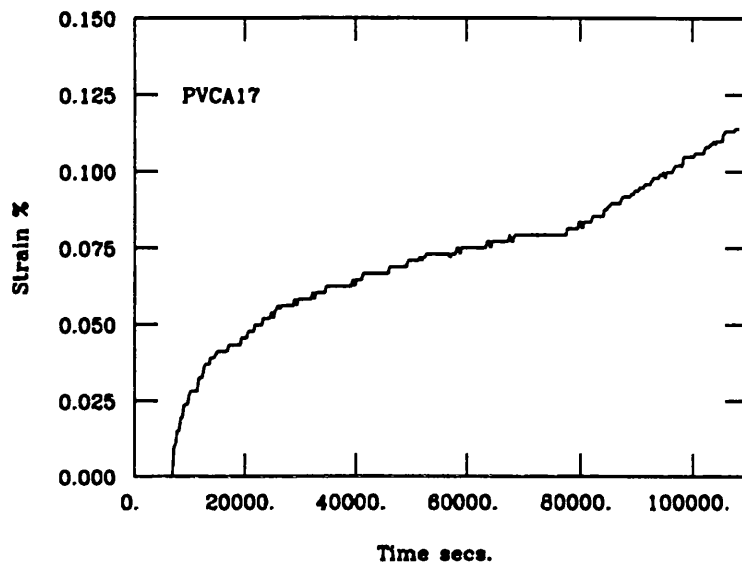


Figure 4.1 Typical creep curves for CaTiO_3 deformed along the $\langle 100 \rangle_{pc}$ compression axis.

A series of 16 experiments was also carried out on CaTiO₃ with applied stress parallel to the $\langle 110 \rangle_{pc}$ axis. The results are presented in Table 4.3 with typical creep curves shown in Figure 4.2. Runs 34 and 40 failed after loading, while 36B did not reach steady-state.

Table 4.3 Results of experiments on CaTiO₃ with stress parallel to $\langle 110 \rangle_{pc}$

Run	T C	MPa	%	t min	$\dot{\epsilon}$ sec ⁻¹
PVCA35	1366	36.1	21.0	180	4.47×10^{-5}
PVCA36A	1313	24.6	5.0	1300	1.00×10^{-7}
PVCA36B	1313	41.0	18.0	118	2.41×10^{-5}
PVCA37A	1282	28.3	4.0	1283	6.43×10^{-8}
PVCA37B	1282	45.4	6.5	1426	6.44×10^{-7}
PVCA37C	1282	62.4	8.4	1435	1.00×10^{-6}
PVCA38A	1366	22.4	3.0	1303	1.32×10^{-7}
PVCA39B	1366	44.8	8.0	1448	5.00×10^{-7}
PVCA38C	1366	67.0	10.5	135	5.26×10^{-5}
PVCA39A	1400	27.5	3.0	1293	2.29×10^{-7}
PVCA39B	1400	40.6	5.8	1460	3.52×10^{-7}
PVCA39C	1400	64.0	8.9	305	1.90×10^{-6}
PVCA41	1418	29.8	15.0	20	8.32×10^{-5}
PVCA42	1416	19.0	16.8	144	2.67×10^{-5}
PVCA43	1384	24.0	15.2	191	1.04×10^{-5}
PVCA44A	1348	22.3	8.0	1251	4.65×10^{-7}
PVCA44B	1348	30.6	15.8	151	9.54×10^{-6}

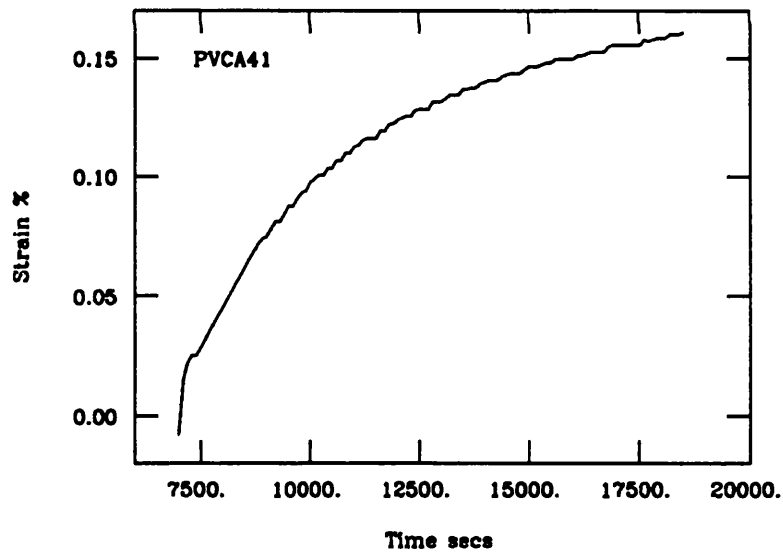
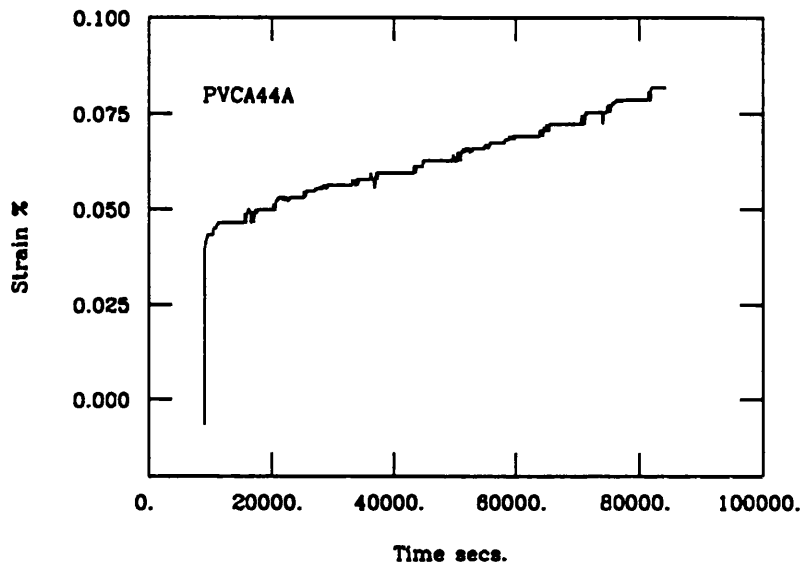


Figure 4.2 Typical creep curves for CaTiO_3 deformed along the $\langle 110 \rangle_{pc}$ compression axis.

4.1.2 Experiments on NaNbO₃

The results of the 18 experiments carried out on NaNbO₃ oriented with the <100>_{pc} parallel to the stress direction are given in Table 4.4 and typical creep curves in Figure 4.3. The behaviour is similar to that observed for CaTiO₃. All runs were assumed to have reached the quasi steady-state regime except for NANB01 which failed shortly after loading.

Table 4.4 Results of experiments on NaNbO₃

Run	T C	MPa	%	t min	$\dot{\epsilon}$ sec ⁻¹
NANB1	908	Fail			
NANB2A	906	41.5	1.0	1280	8.46x10 ⁻⁹
NANB2B	906	69.2	4.5	1411	2.01x10 ⁻⁷
NANB2C	906	83.0	10.5	1400	4.44x10 ⁻⁷
NANB3A	971	41.5	5.0	325	2.94x10 ⁻⁷
NANB3B	971	58.0	8.0	1073	1.77x10 ⁻⁷
NANB3C	971	82.8			Fail
NANB4A	971	55.0	6.1	1301	1.41x10 ⁻⁷
NANB4B	971	70.0	10.4	373	8.98x10 ⁻⁷
NANB5A	1067	42.8	5.0	1305	9.86x10 ⁻⁸
NANB5B	1067	58.7	9.8	386	1.25x10 ⁻⁶
NANB5C	1068	70.0	16.0	200	3.60x10 ⁻⁶
NANB6A	1115	39.3	12.0	1293	3.09x10 ⁻⁷
NANB6B	1115	52.4	13.8	210	4.14x10 ⁻⁷
NANB7A	1164	29.4	6.5	1285	1.71x10 ⁻⁷
NANB7B	1164	44.0	10.5	1438	4.38x10 ⁻⁷
NANB7C	1164	58.7	12.5	1435	6.68x10 ⁻⁷
NANB7D	1164	80.7	15.5	276	1.21x10 ⁻⁶
NANB8	1212	27.0	8.6	1143	1.09x10 ⁻⁶

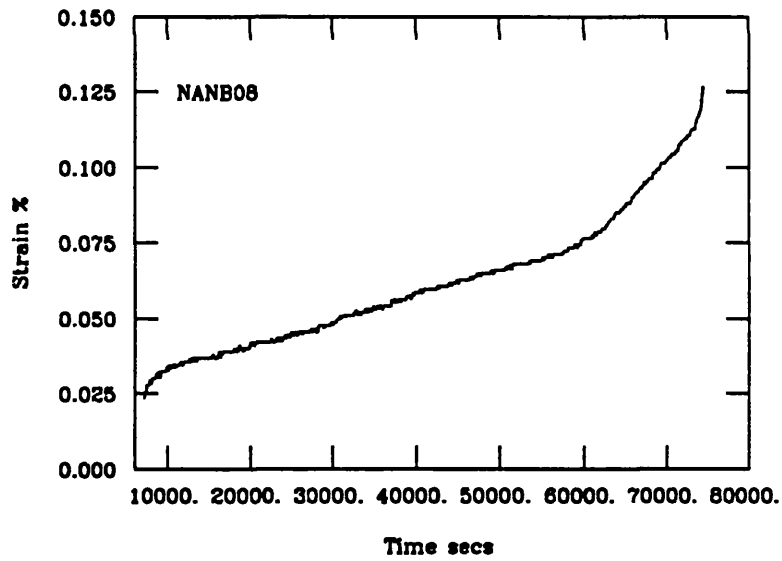
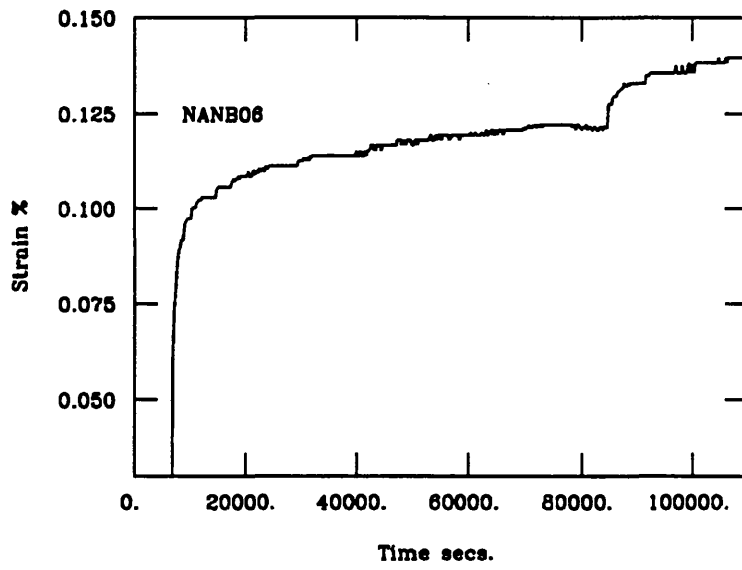


Figure 4.3 Typical creep curves for NaNbO₃

4.2 Data analysis

4.2.1 Analysis of data by linear regression

The classical regression method was used to assess the values of apparent activation energy Q , and stress exponent n using the following relationships:

For Q ,

$$\ln \dot{\epsilon}_{(\sigma)} = f(1/RT) \quad (4.1)$$

and for n ,

$$\ln \dot{\epsilon}_{(T)} = f(\ln \sigma) \quad (4.2)$$

Figure 4.4 shows the results for experiments on CaTiO_3 with stress parallel to $\langle 100 \rangle_{pc}$. The values of Q obtained by this method show a wide variation, while from the values of n , it almost seems as if two processes are at work, one with $n = 2.25$ and one with $n = 4.4$. Problems occur with this method for the following reasons:

- (1) Because of the limited experimental conditions, calculation of Q is only possible for 4 values of stress, therefore it is not possible to assess the possibility of stress dependence on Q .
- (2) The calculation of n is only possible for 4 values of temperature.
- (3) There is no way to obtain a value for the creep constant A .
- (4) The systematic estimation of errors on the results is not possible.

The results obtained using this method can therefore, only be considered as a rough estimate.

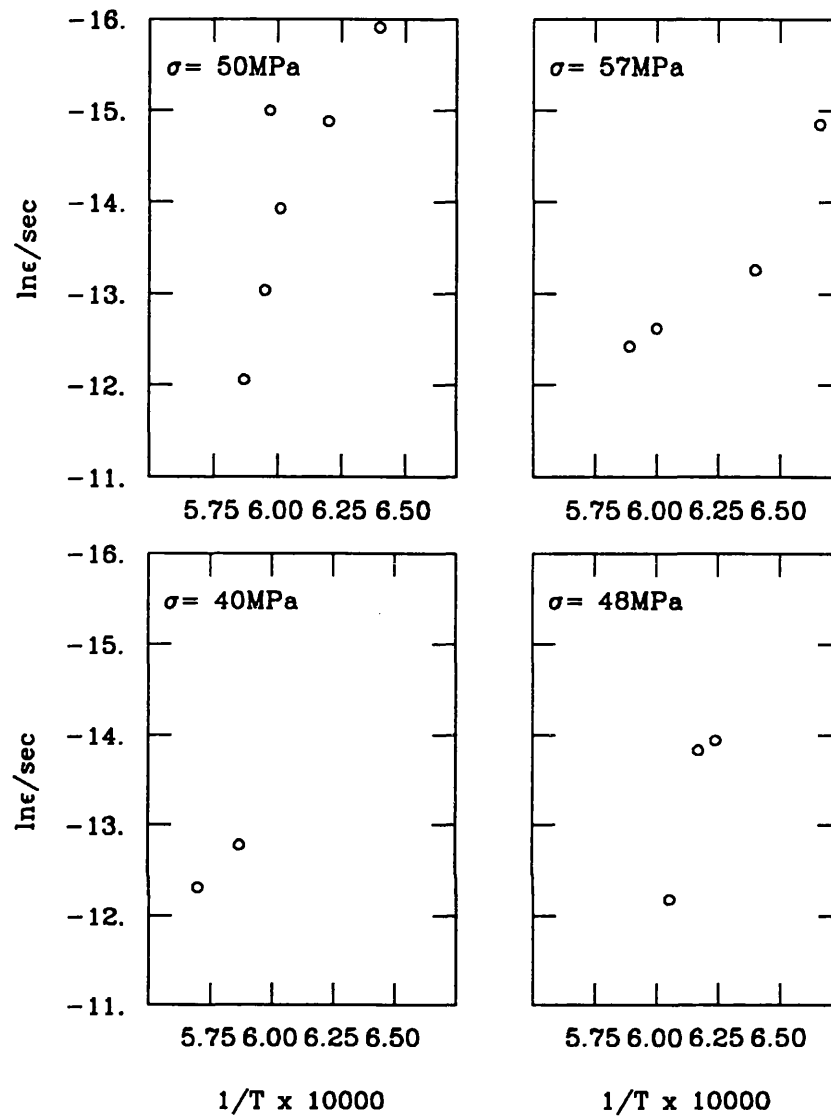


Figure 4.4 Determination of Q and n from linear regression.

$$\sigma = 50 \text{ MPa} \quad Q = 381.5 \text{ kJmol}^{-1}$$

$$\sigma = 57 \text{ MPa} \quad Q = 272.5 \text{ kJmol}^{-1}$$

$$\sigma = 40 \text{ MPa} \quad Q = 235.5 \text{ kJmol}^{-1}$$

$$\sigma = 48 \text{ MPa} \quad Q = 763.0 \text{ kJmol}^{-1}$$

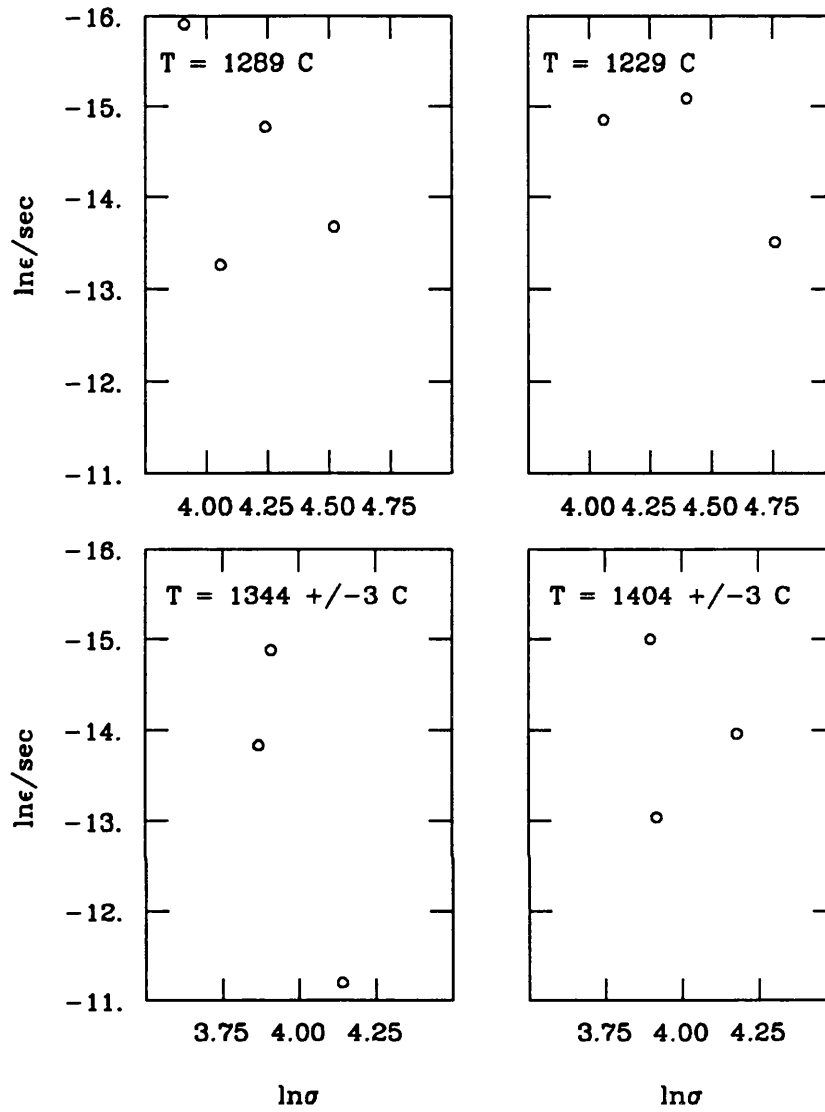


Figure 4.4 continued.

T = 1289.0 n = 4.40

T = 1229.0 n = 2.25

T = 1398.0 n = 2.25

T = 1402.0 n = 4.45

4.2.2 Analysis by inversion

The problems above can be largely overcome by using the generalized non-linear global inversion technique outlined in section 3.6. Uncertainties in the values of temperature, stress and strain rate were assessed and the inversion program (Sotin and Poirier 1986) used to fit the data to two different creep laws. The first, has a stress dependent activation energy:

$$\dot{\epsilon} = A\sigma^n \exp(-QB/RT) \quad (4.3)$$

where B is the stress dependence and the second, has the more usual form of the power-law creep equation:

$$\dot{\epsilon} = A\sigma^n \exp(-Q/RT) \quad (4.4)$$

Experimental errors were varied to assess their effects on the values of Q, A and n and on their respective errors. The errors on temperature and stress were first set to values of +/- 3 and +/-10% respectively. Small changes in these values made little or no difference to the results obtained. The errors on the strain rate however, are more important. These were set to variable values depending on the value of the strain rate and in general, the smaller the strain rate, the larger the uncertainty. Three groups of inversions were performed using the following error sets:-

- A) $\ln \dot{\epsilon}$ +/- 1.5, 1.8, 2.0 for strain rates of 10^{-6} , 10^{-7} and 10^{-8} respectively
- B) $\ln \dot{\epsilon}$ +/- 0.5, 1.2, 1.5 for strain rates of 10^{-6} , 10^{-7} and 10^{-8} respectively
- C) $\ln \dot{\epsilon}$ +/- 0.5 for all values.

In all cases, a maximum of 21 iterations was allowed.

4.3 Results

4.3.1 CaTiO₃ with stress parallel to <100>_{pc}

The data from these experiments were first fitted to the stress dependent creep law. In all inversions, no convergence was obtained and in two cases, a negative activation energy was calculated.

For the second creep law, the first series of three inversions all gave residual values for runs 20A and 20B that were greater than two standard deviations. Therefore these results were removed and the process repeated. All of the second series of inversions converged within 9 iterations (Table 4.5).

The inversion using the second error set had the largest uncertainties in all three variables and a rather high residual value for run 22A. The inversion using the first error set was considered to be the best as it has the lowest residuals inferring a good fit to the data.

Table 4.5 Results of second series of inversions. Values of Q in kJmol⁻¹

Error set	ln A	+/-	n	+/-	Q	+/-
A	-39.09	6	3.28	.48	443.99	57
B	-44.76	5	3.39	.37	392.63	40
C	-38.91	8	3.17	.59	419.84	70

4.3.2 CaTiO₃ with stress parallel to <110>_{pc}

The same process as described above was repeated for the analysis of the CaTiO₃ experimental data in the second orientation. Again, no convergence could be obtained using the stress-dependent creep law.

Using the power law, another series of three inversions was performed using the three error sets above. Using the second set of strain rate errors, the program did not converge, and in all three, the data for runs 44B and 38C did not converge. These were discarded and the procedure repeated for a third time (Table 4.6).

In all cases, the residuals had values of less than 2 standard deviations and all converged in 9 iterations. Error set 1 inverted to give the best fit to the data.

Table 4.6 Results of inversion. Q in kJmol⁻¹

Error set	ln A	+/-	n	+/-	Q	+/-
A	-37.89	11	2.5	.46	273.6	95
B	-49.85	13	3.09	.56	259.1	89
C	-43.7	15	2.75	.68	261.4	99

4.3.3 NaNbO₃

The same error sets were used for NaNbO₃ as for CaTiO₃. With the stress dependent creep law, as in the previous case, the program did not converge. Using the power-law and all of the data, inversions using each of the variable strain rate errors (sets A and B) only converged after 16 iterations. The corresponding residuals for runs 7D and 8 were high for both. However, using the strain rate error set C, ln $\dot{\epsilon}$ +/- 0.5 (inversion 1 in Table 4.6), gave good results and converged within 11 iterations. Another series of inversions was performed after discarding the results for runs 7D and 8 (inversions 2, 3 and 4 in Table 4.6). Inversion 2 was chosen as the best fit to the data. Even though the uncertainties associated with this inversion are large, the values of the residuals were very low.

Table 4.7 Results of inversion. Values of Q in kJmol⁻¹

No.	ln A	+/-	n	+/-	Q	+/-
1C	-64.2	11	3.6	.70	165.9	32
2A	-92.0	15	5.3	.99	192.3	41
3B	-97.1	13	5.67	.85	203.5	36
4C	-93.0	13	5.4	.89	195.9	37

4.4 Examinations of samples

After deformation, samples of CaTiO₃ were examined for external evidence of slip. No traces of slip planes on the faces could be seen, even under a microscope. Many of the CaTiO₃ samples broke apart when removed from the apparatus, therefore examination was limited to a small number of samples. All samples of NaNbO₃ crumbled when removed from the anvils and so could not be analyzed in any detail.

4.4.1 Examination and analysis using TEM

Prior to the examination of deformed samples, both undeformed and annealed samples were examined using TEM to look at the type and density of deformation and twin structures present.

In the undeformed specimen (Plate 4.1), large scale twinning, with {100}_{pc} twin composition planes, was found to be a very common feature. CaTiO₃ commonly twins by either a 90° or 180° rotation about an axis perpendicular to {001} (White et al. 1985). Dislocations were observed to occur singly and were not present in any great number.

After annealing for 2 hours at 1520°C, the density of twins increases

greatly. In Plate 4.2, twins are present with composition planes in two orthogonal directions. These twins are present on a much finer scale than in the non-annealed samples. This has been assumed to be the result of one or more phase transitions during cooling from a high temperature, high symmetry phase. CaTiO_3 is thought to transform from orthorhombic to tetragonal at temperatures above 1200°C (Kay and Bailey 1957, Wang et al 1990) and from tetragonal to cubic at higher temperatures. The temperature at which the tetragonal to cubic transformation takes place is not yet known.

The samples have been subjected to a range of stress - temperature conditions. However, even in highly deformed samples, the dislocation density appears to be low. No correlation was found between the type of structures observed and the degree of deformation.

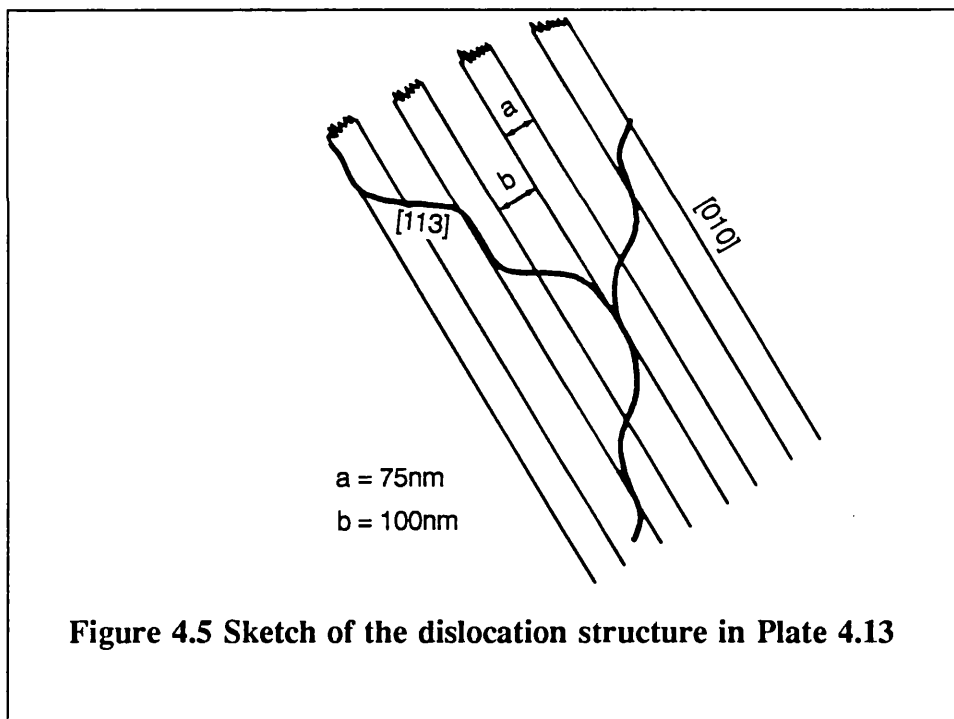
Isolated dislocations, are seen only rarely. The forked dislocation in Plate 4.3 is typical of those observed. This is an edge dislocation with a line direction $\langle 010 \rangle_{\text{pc}}$ and Burgers vector \mathbf{b} of the type $[100]$. The formation of jogs is illustrated in Plate 4.4. Quite often, dislocations are composed of segments having different values of \mathbf{b} . The central part of the dislocation in Plate 4.4 shows only residual contrast for $\mathbf{g} = [044]$ and $[021]$ and therefore the most likely Burgers vector is $[100]$.

This segmentation is shown more clearly in Plates 4.5 to 4.8. In Plate 4.5, the dislocation appears to be quite straightforward, but when tilted (Plate 4.6) reveals that it is composed of a number of segments which are invisible for different values of \mathbf{g} . The same is true for the dislocation in Plates 4.7 and 4.8 which has an even more complex structure. For both of these dislocation structures, the dominant line directions are $\langle 002 \rangle$ and $\langle 110 \rangle$.

Lines of near parallel dislocations with a seemingly regular spacing are more common. In the example in Plate 4.9, the dislocations are arranged in pairs which seem to be mirror images of each other. Wall structures are found

to be a continuation of the parallel dislocation lines which are evolving into highly organised hexagonal boundaries (Plate 4.10), which are indicative of recovery processes at work.

Splitting of dislocations into partials is not common, although two features have been found which have been attributed to this. Plate 4.13 and 4.14 show a series of straight parallel dislocations which dissociated into two partials separated by a stacking fault. Crosscutting these are a second group of dislocations which appear to be alternately attracted to and repelled by the partials. Figure 4.5 is a simplified sketch of this configuration showing that the width of the stacking fault, (a), and the distance between the partials, (b), remains constant.

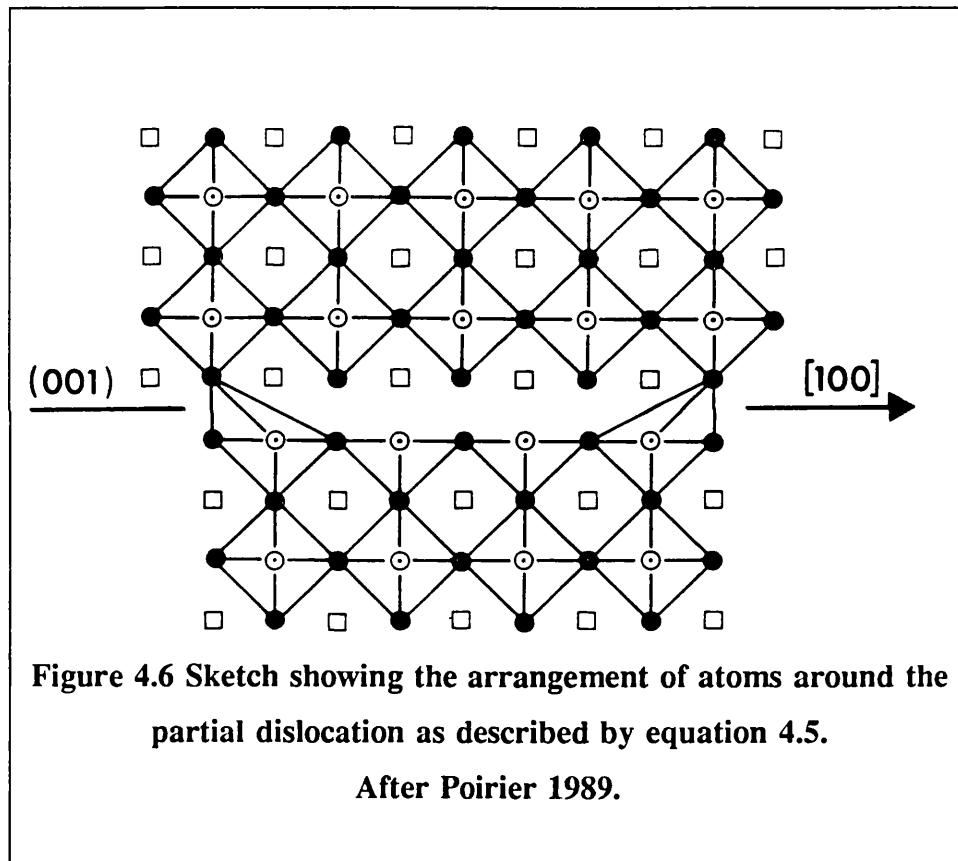


The partials have Burgers vector $[010]$, so this could represent the dissociation of the dislocation into collinear partial vectors as shown in Figure

4.6 and represented by;

$$\mathbf{b} = [010] \rightarrow \frac{1}{2}[010] + \frac{1}{2}[010] \quad (4.5)$$

This type of configuration is considered theoretically possible for CaTiO_3 (Poirier et al. 1989) although this is the first time it has been observed.



The 'scallop' features shown in Plate 4.11 and 4.12 have also been observed in BaTiO_3 perovskite (Doukhan and Doukhan 1988, Beauchesne and Poirier 1989). These have been interpreted as high temperature climb

dissociation of [010] dislocations into 2 partials where

$$[010] \rightarrow 1/2[011] + 1/2[0\bar{1}1] \quad (4.6)$$

4.5 Summary and conclusions

4.5.1 A creep law for CaTiO₃

The combined information from the creep experiments and electron microscopy leads to the conclusion that CaTiO₃ deforms according to a power law where the values of A, Q and n are dependent on the orientation of the crystal.

When stress is applied parallel to the $\langle 100 \rangle_{pc}$ direction the values of the parameters are:

$$\begin{aligned} \ln A &= -39.09 \pm 6 \\ n &= 3.28 \pm 0.48 \\ Q &= 443.99 \text{ kJmol}^{-1} \pm 57 \end{aligned}$$

When stress is parallel to $\langle 110 \rangle_{pc}$ then :

$$\begin{aligned} \ln A &= -37.89 \pm 11 \\ n &= 2.5 \pm 0.46 \\ Q &= 273.60 \text{ kJmol}^{-1} \pm 95 \text{ kJmol}^{-1} \end{aligned}$$

The two values of n suggest that this behaviour can be attributed to climb controlled power law or Weertman creep (section 2.3.2). This is

confirmed by the observation of well ordered dislocation microstructures such as the networks shown in Plate 4.10. Although recovery by cross-slip may be occurring, it will not be the dominant process.

4.5.2 A creep law for NaNbO₃

NaNbO₃ also deforms by a power law mechanism with the variables $\dot{\epsilon}$ and σ in the power-law equation having the following values:

$$\begin{aligned}\ln A &= -92. \pm 11 \\ n &= 5.3 \pm 0.9 \\ Q &= 192.3 \text{ kJmol}^{-1} \pm 41 \text{ kJmol}^{-1}\end{aligned}$$

The exact nature of the dominant mechanism, or of the slip systems involved cannot be ascertained. However, the high value of n would be consistent with cross-slip controlled creep (section 2.3.2.2), although without TEM analyses this is purely speculative.



Plate 4.1 Dark field image of undeformed,
unannealed CaTiO₃. Scale bar = 230 nm.

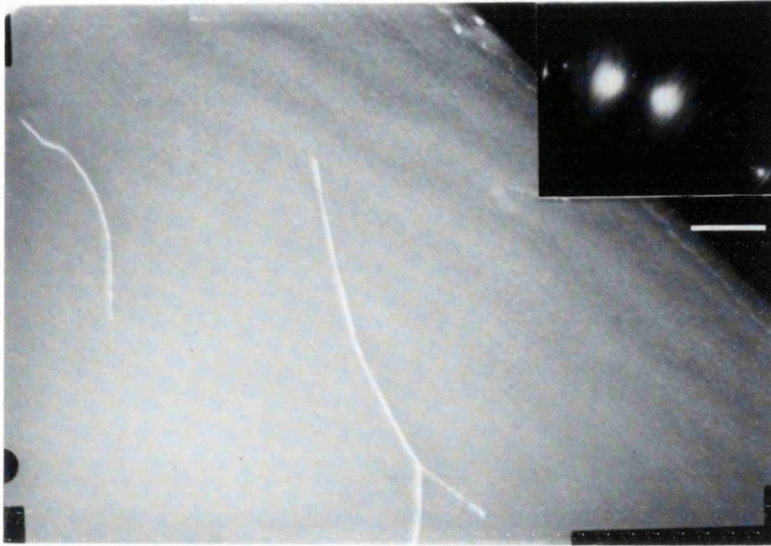


Plate 4.3 Dark field image of dislocation from PVCA17.
 $g = \langle 003 \rangle$. The line direction is $\langle 010 \rangle$.
Scale bar = 110 nm.

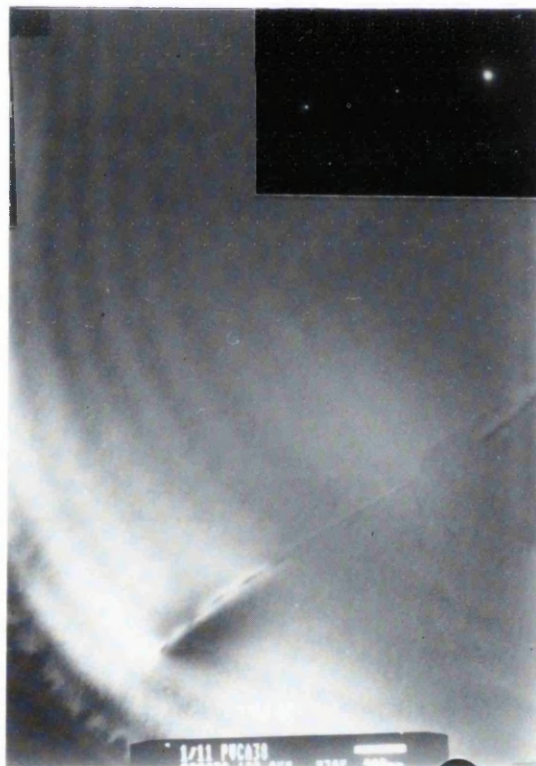


Plate 4.4 Dark field image from PVCA38. $g = \langle 044 \rangle$
The line direction is $\langle 012 \rangle$ Scale bar = 200 nm.

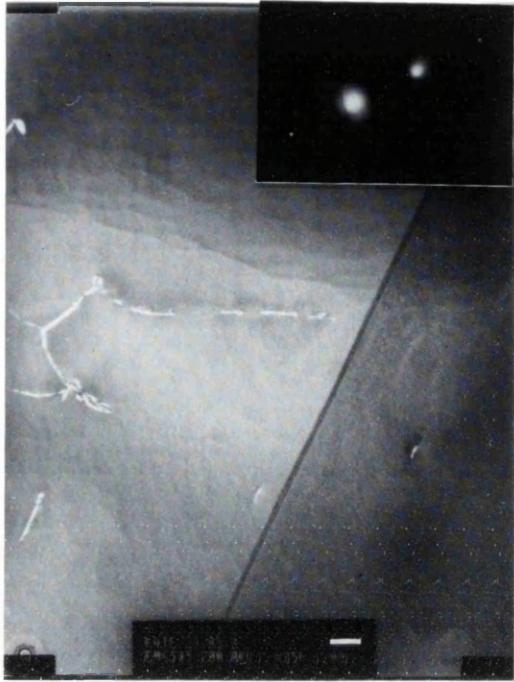


Plate 4.5 Weak beam image of dislocation from PVCA18.
 $g = \langle 002 \rangle$. Scale bar = 200 nm



Plate 4.6 Dark field image of the same dislocation,
but with $g = \langle 022 \rangle$. Scale bar = 200 nm.

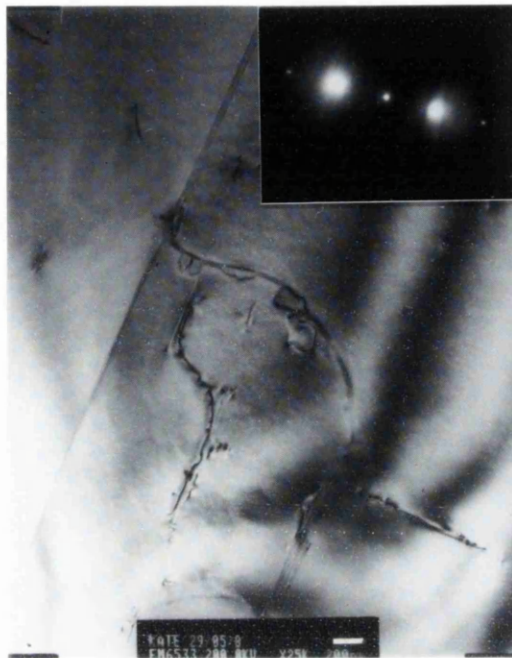


Plate 4.7 Bright field image of dislocations from PVCA18. $g = \langle 200 \rangle$. Scale bar = 200 nm.

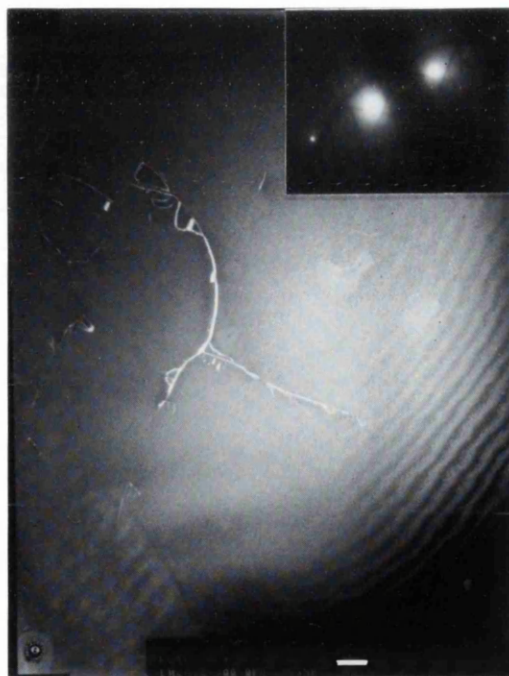


Plate 4.8 Weak beam image of the same dislocation but with $g = \langle 022 \rangle$. Scale bar = 200 nm.

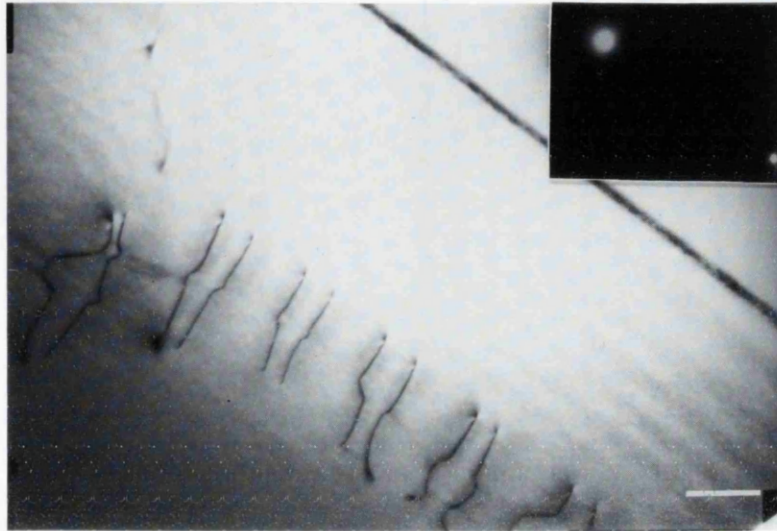


Plate 4.9 Bright field image of dislocation pairs
with line direction $\langle 112 \rangle$ from PVCA17. $g = \langle 024 \rangle$.
Scale bar = 170 nm.

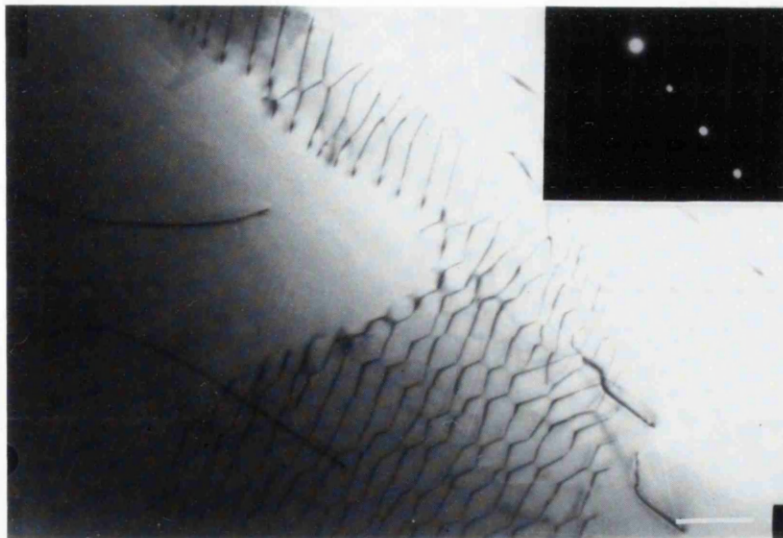


Plate 4.10 Dislocation network from PVCA17.
 $g = \langle 012 \rangle$. Scale bar = 170 nm

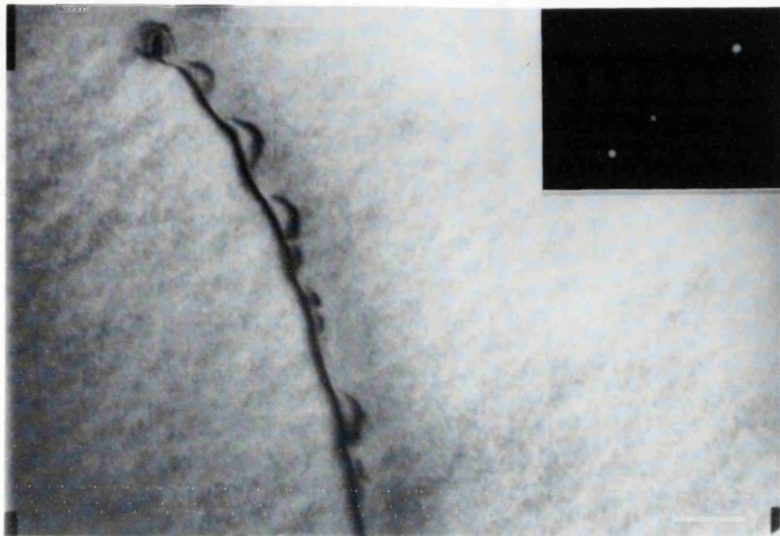


Plate 4.11 Bright field image of 'scallops' from PVCA18. $g = \langle 004 \rangle$. Scale bar = 95nm

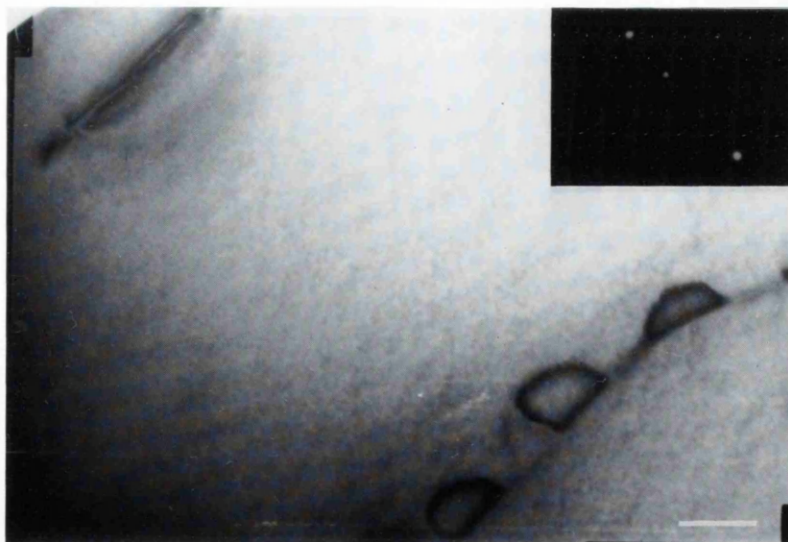


Plate 4.12 Detail of scallops from PVCA18 as above. Scale bar = 95 nm

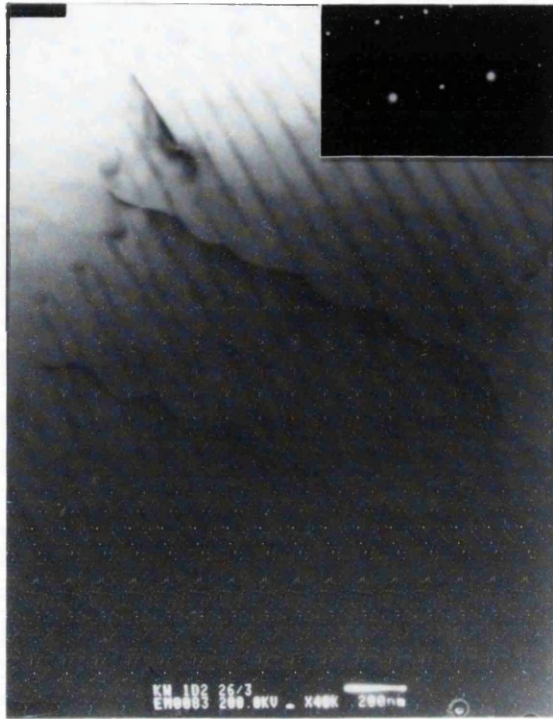


Plate 4.13 Two sets of dislocations from PVCA21.
 $g = \langle 033 \rangle$. Scale bar = 200 nm.

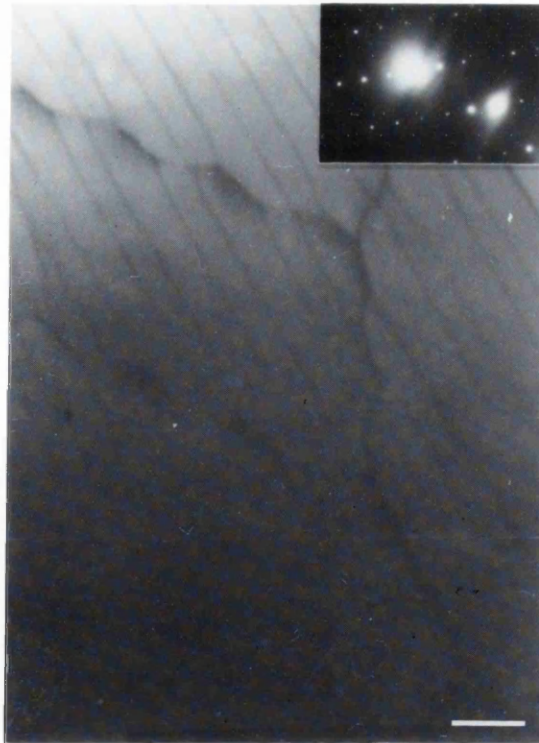


Plate 4.14 The same dislocations as above,
 but with $g = \langle 040 \rangle$

CHAPTER 5: COMPUTER SIMULATION OF DEFECTS AND DIFFUSION IN PEROVSKITES

5.1 Introduction

Over the past decade, enormous advances have been made in the field of computer simulation. The development of supercomputers such as the Cr. v XMP-416 and of more sophisticated codes, means that it is now possible to model many of the physical and thermodynamic properties of a whole range of materials with some confidence (for recent review see Price et al. 1989). Defect calculations on simple oxides (Catlow 1977) and on more complex materials such as titanate perovskites (Udayakumar and Mackrodt 1989, Lewis and Catlow 1986) and garnets (Edwards 1988) are also well established.

Computer simulation techniques can range from quantum mechanical to atomistic type calculations. This latter technique, based on the Born model of solids, has been found to be the most successful when dealing with complex silicates and is used in this study.

In this chapter, the computer simulation methods are briefly described and the basis of the defect energy calculations outlined. Next, the results of a series of defect calculations on the perovskites SrTiO_3 and CaTiO_3 are presented and are compared to data from experiments, where available. The bulk of this chapter, however, deals with simulations of defects and diffusion in MgSiO_3 perovskite which have been carried out at both zero and simulated high pressures. Finally, a model for defect processes in this phase is put forward.

5.2 Simulation Techniques

5.2.1 Interatomic potentials

The atomistic simulation method uses an algorithm or interatomic potential to describe the total energy of the system in terms of atomic coordinates. The most common potentials have a rigid-ion, central force pairwise additive form. For ionic or semi ionic solids, the dominant component of the cohesive energy U_T will be the electrostatic or Coulombic term U_C . However as ions are not point charges, as assumed in the Coulombic term, it is necessary to take into account the short range repulsive interactions U_{ij} , produced by the overlap of nearest neighbour electron clouds. This short range component is well modeled by the Buckingham potential which includes an optional C term:

$$U = \sum_{ij} A_{ij} \exp(-r_{ij}/B_{ij}) - C_{ij} r_{ij}^{-6} \quad (5.1)$$

where the parameters A and B, for each pairwise interaction are obtained either theoretically, by fitting to ab initio energy surfaces, or empirically, by fitting to crystalline properties.

To this basic potential can be added a shell model to simulate polarizability. Here, the electron cloud with charge Y_i is coupled to the core by an harmonic spring (Figure 5.1). The interaction between the core and shell U_s on an ion i will be:

$$U_s = \frac{1}{2} k_i s_i^2 \quad (5.2)$$

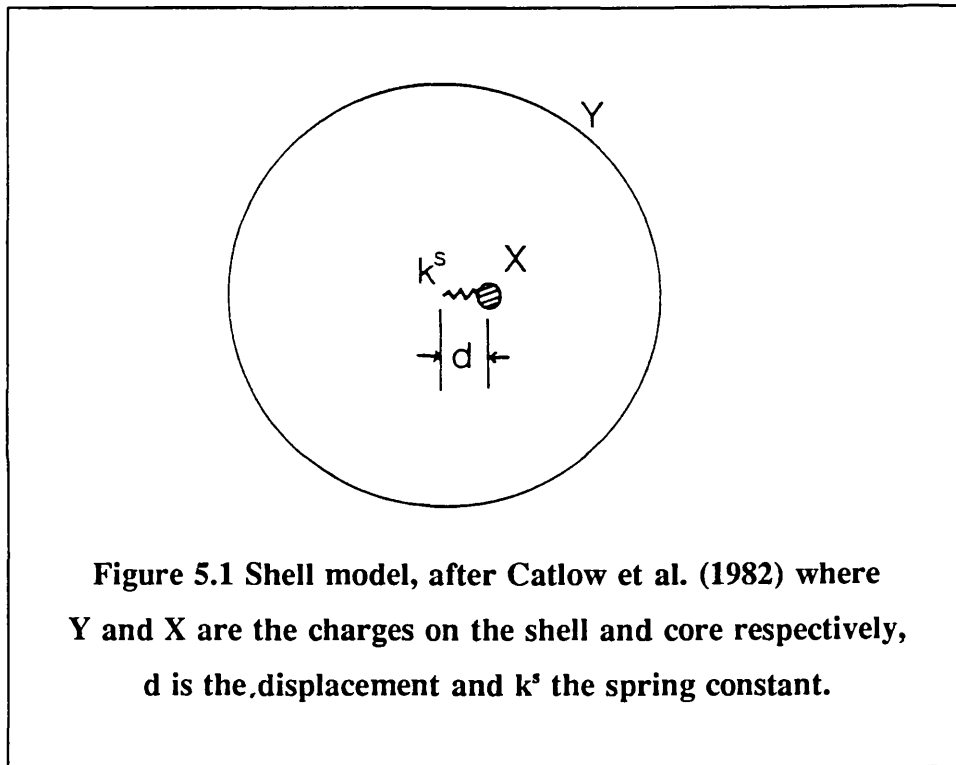
where k_i is the spring constant and r_i^2 the core-shell separation. The electronic polarizability, α_i , of an ion i is then given by:

$$\alpha_i = \frac{(Y_i)^2}{(k_i + r_i)} \quad (5.3)$$

In addition to this, a bond bending term can be used to include the directionality of the O-Si-O bonds. This bond bending is expressed by:

$$U_B = 1/2 \sum_{ijk} k_{ijk} (\theta_{ijk} - \theta_0)^2 \quad (5.4)$$

where k_{ijk} is the spring constant, θ_{ijk} the simulated bond angle and θ_0 the equilibrium bond angle.



5.2.2 Modelling the perfect lattice

The perfect lattice structures and corresponding lattice energies used in this study have been modelled using the code PARAPOCS (Parker and Price 1989), with atomic coordinates minimized to both constant volume and constant pressure. The equilibrium positions of the ions are evaluated by minimizing the lattice energy with respect to both cell parameters and ionic

positions until all strains acting on the crystal are removed. Full details of this method are given by Catlow and Norgett (1978).

PARAPOCS can also be used to evaluate the structure and lattice energy at high pressures by fixing the pressure and minimising cell dimensions and ionic coordinates until the minimum energy configuration is achieved.

5.2.3 Calculating defect energies

The computer code CASCADE (Leslie 1982) allows the calculation of defect energies by simulating the relaxation of the lattice around a defect. In predominantly ionic materials, the defects are charged species and can cause long range disruption in the lattice. The most effective approach to modelling such defects is the two region method, developed by Mott and Littleton (1938), where the crystal is divided into two spherical regions (Figure 5.2).

In region 1, which contains the defect at its centre, an explicit atomistic simulation is carried out to adjust the positions of all ions until they are at positions of zero force, i.e. they are relaxed around the defect. In region 2, the effects of the defect are relatively weak and can be treated by more approximate means.

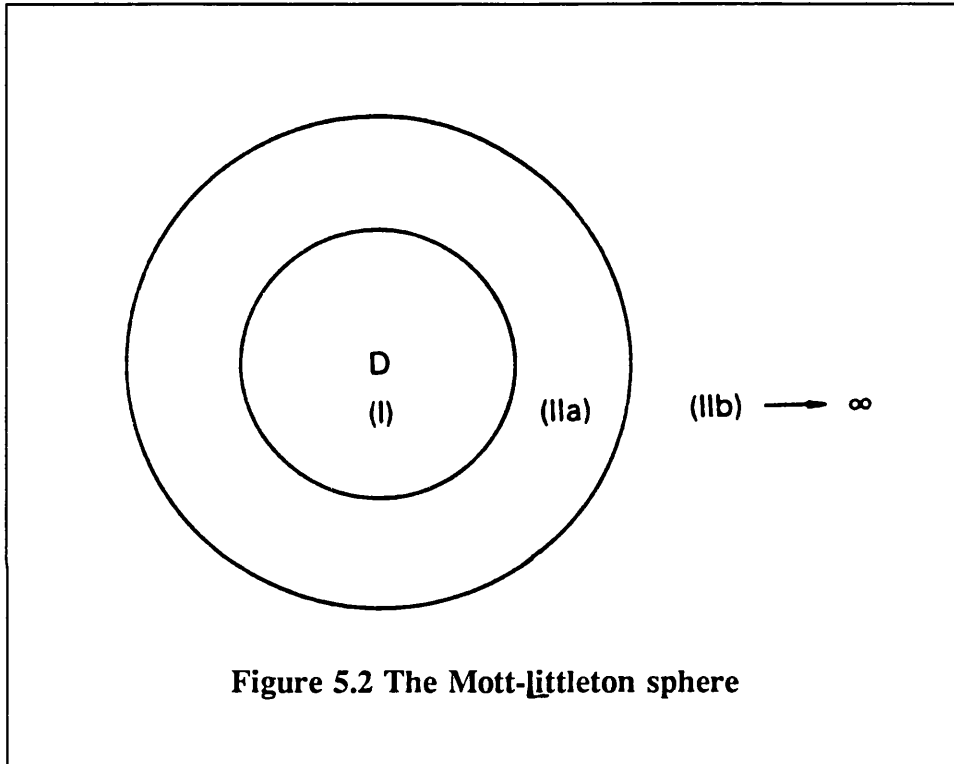
Using the Mott-Littleton method, a defect with charge q causes a polarization P , at a point r according to:

$$P_r = qr/r^3 (1-\epsilon_0^{-1}) \quad (5.5)$$

where ϵ_0 is the static dielectric constant. (This method is strictly only applicable to cubic materials, but see Catlow and Mackrodt (1982) for discussion.) For the two region approximation, the total energy required for the formation of a defect is given by:

$$E_D = E_1(x) + E_2(x,y) + E_3(y) \quad (5.6)$$

where E_1 is the energy of interaction of atoms in region 1 with coordinate vector x , E_3 the energy of ions with displacement y in region 2, and $E_2(x,y)$ describes the interaction between the two regions.



When y is sufficiently small, as is generally assumed, E_3 can be expressed by the harmonic approximation as:

$$E_3 = 1/2 y^T A y \quad (5.7)$$

where A is the force constant matrix. At equilibrium:

$$dE_2(x,y)/dy = -A \cdot y \quad (5.8)$$

Therefore E_D in equation 5.6, can be expressed in terms of E_1 , which is calculated by explicit summation, and E_2 and its derivatives. For this latter term, it is necessary to define a subdivision of region 2, region 2A, where the interaction of ions with the defect in region 1 are considered in more detail. For the remainder of region 2, the Mott-Littleton calculations assume that displacements are due only to the net charge of the defect. The resulting defect energy is then a measure of the perturbation by the defect of the static lattice energy of the crystal. For further details of the method see Catlow (1986).

5.3 The treatment of defects and diffusion

The concept of point defects and their importance in creep processes was introduced in Chapter 2. In this section, the thermodynamics of defects and diffusion will be discussed in relation to the computer simulations. The notation used is that developed by Kröger (1971) where V_A denotes a vacancy of species A and A_B an interstitial of species A at site B.

5.3.1 Defect formation energies

Consider a crystal at equilibrium, where the Gibbs free energy, G , is at a minimum. If defects are introduced, then the free energy changes by an amount ΔG which is defined as:

$$\Delta G_f = \Delta H_f - T\Delta S_f \quad (5.9)$$

and

$$\Delta H_f = \Delta E_f + P\Delta V_f \quad (5.10)$$

where the subscript f is for defect formation, ΔH is the enthalpy, ΔS the entropy, ΔE is the energy, P the pressure and ΔV the volume of formation.

The energy of formation of a Schottky defect is given as the sum of the

free energies of formation of the individual vacancies making up the defect less the lattice energy of the phase removed to the surface:

$$\Delta G_S = \Delta G_{V_1} + \Delta G_{V_2} + \dots + \Delta G_{V_n} - U_{sfce} \quad (5.11)$$

Similarly, the Frenkel defect formation energy is made up of the sum of the composite vacancy and interstitial energies:

$$\Delta G_F = \Delta G_V + \Delta G_I \quad (5.12)$$

At any temperature above 0K, there will be an equilibrium fraction of vacancies, X, given by:

$$X = n_v/n = \exp(-\Delta G_f/RT) \quad (5.13)$$

where n_v is the number of vacancies and n the number of sites. This term is highly temperature dependant and as the temperature increases, so will the number of vacancies. This is known as the intrinsic regime. Below some critical temperature T_c , the vacancy concentration will be controlled by the impurity concentration and is therefore temperature independent. This is the extrinsic regime.

5.3.2 Migration and diffusion

The free energy of defect migration ΔG_M can be defined in a similar way to that of defect formation:

$$\Delta G_M = \Delta E_M - T\Delta S_M \quad (5.14)$$

and

$$\Delta H_M = \Delta E_M + P\Delta V_M \quad (5.15)$$

with the subscript M denoting migration and all other terms are as previously

defined. As an ion moves from one site to a vacant site, it crosses over the highest point (saddle point) of the potential energy barrier. The free energy of migration is then the free energy of the interstitial at the saddle point less the free energy of the ground state:

$$\Delta G_M = \Delta G_{SP} - \Delta G_{GS} \quad (5.16)$$

This quantity is the activation energy for diffusion in the extrinsic regime.

In the intrinsic regime, the concentration of vacancies will be dependent on temperature. The greater the number of vacant sites, the more easily an ion can diffuse through the lattice. Therefore the expression for activation enthalpy in the intrinsic regime must contain a component of Schottky defect formation energy. Adding this to Equation 5.16 we have:

$$\Delta G_D = \Delta G_M + (\Delta G_f/n) \quad (5.17)$$

where n is the number of ions in the Schottky defect.

5.3.3 Diffusion coefficients

The coefficient of self diffusion is expressed as:

$$D_{SD} = D_0 \exp(-\Delta H/RT) \quad (5.18)$$

For diffusion in the extrinsic regime ΔH will be the migration enthalpy but for intrinsic diffusion, as in section 5.3.2, ΔH will need to contain part of the defect formation energy. The pre-exponential term D_0 , will be roughly constant for all temperatures and can be defined as:

$$D_0 = ga^2\nu n \exp(-\Delta S/R) \quad (5.19)$$

The geometric constant g , is normally given as $1/6$ (Tilley 1988) while n is the number of important defects, S the entropy and ν the vibrational frequency which can be calculated as follows.

In order to move from one lattice site to another, an ion moves from its stable position through a less stable region and therefore must first overcome a potential energy barrier. If self diffusion takes place by a random walk process, the frequency ν , with which an atom will successfully jump from the potential energy well can be calculated from:

$$\nu = 1/2 \pi \sqrt{K/m} \quad (5.20)$$

where m is the effective mass and K the force constant which is given by:

$$\Delta E = 1/2 K(dx)^2 \quad (5.21)$$

where dx the displacement distance. K is calculated by finding the change of energy, ΔE , with displacement from the equilibrium position. Therefore, if the vibrational frequency, entropy and defect concentration are known, or can be calculated, then the diffusion coefficient for any temperature can be estimated.

5.3.4 Defect energies from CASCADE

The classical definition of disorder due to Schottky or Frenkel defects given in section 5.3.1 assumes that stoichiometry will always be maintained. However, in the following sections, non-stoichiometric Schottky defect formation is also considered. The most favourable defect is taken to be the one for which the energy per vacancy is the lowest.

When calculating defect energies at low pressures and temperatures, the entropy and volume terms in Equations 5.9, and 5.10 will be negligible, therefore the vacancy and interstitial energies output from CASCADE will be

roughly equal to the formation enthalpy, so that $\Delta H \approx \Delta E$. At simulated high pressures the volume term becomes important and cannot be ignored. The validity of calculations at high pressures is discussed in more detail in section 5.8.

Finally, it is important to stress that the majority of calculations have been carried out at simulated temperatures of 0K. Therefore, no account is taken of the zero point energy or, more importantly, entropic effects on lattice energy.

5.4 Choice of potential parameters

The full list of potential parameters used in this study is given in Table 5.1. All of the cation-oxygen short range interactions were derived by fitting to experimental data on the relevant oxides. All were taken from Lewis and Catlow (1985) with the exception of the Si-O potential which is from Sanders et al. (1984). This combining of oxide potentials to use for more complex materials has previously been shown to be valid for the Mg silicate olivine (Price et al. 1988), for titanate perovskites (Udayakumar and Mackrodt 1989) and for MgSiO₃ perovskite (Wall and Price 1989). The O-O short range parameters were derived theoretically using Hartree-Fock methods (Catlow 1977).

The spring constants used to describe oxygen polarizability and O-Si-O bond bending were also taken from Sanders et al. (1984) and were derived by fitting to the structural and elastic properties of quartz. Shell models are available for Ti but were not used as the results obtained using the rigid ion were closer to the measured properties. No bond bending term for O-Ti-O is available. The spring constant for oxygen polarizability in the titanates is taken from Parker (1982). All cation - cation interactions are considered to be simply coulombic only in nature.

Table 5.1 Short range potential parameters used in this study. k^B in $eV\text{\AA}^{-2}$, k^S in $eV\text{rad}^{-2}$, short range cut-off in \AA

Ion	Charge q	Pair	A \AA	B eV	C $eV\text{\AA}^6$
Mg	+2	Mg-O	1428.5	0.2945	
Fe	+2	Fe-O	1207.6	0.3084	
Ca	+2	Ca-O	1228.9	0.3372	
Sr	+2	Sr-O	1400.0	0.3500	
Al	+3	Al-O	1473.3	0.3006	
Fe	+3	Fe-O	1102.4	0.3299	
Ti	+4	Ti-O	754.2	0.3879	
Si	+4	Si-O	1283.9	0.3205	10.66
O _{sh}	-2.848	O-O	22764.3	0.1490	27.88
O _c	+0.848				
Phase		k^S	k^B	Cut-off	
MgSiO ₃		74.92	2.09	11.95	
CaTiO ₃		27.29		10.33	
SrTiO ₃		27.29		7.42	

In all cases the models assume full ionicity. This is well justified for MgSiO₃ since ab initio calculations by Cohen et al. (1989) show little evidence for covalent bonding in this phase. The other oxide perovskite structure investigated by the above authors was BaTiO₃. This was predicted to have a much higher degree of covalency. However, BaTiO₃ is ferroelectric, whereas both CaTiO₃ and SrTiO₃ are not and in this case can be considered to be closer to MgSiO₃. Therefore it is concluded that the assumption of full ionicity in all three phases is a reasonable one.

5.5 Perfect lattice calculations - Results

Calculations using the code PARAPOCS were performed to evaluate the static lattice energies used in the defect calculations and to test the reliability of the interatomic potentials chosen. All perfect lattice calculations were minimized to constant pressure. Table 5.2 shows the calculated and experimental values of the structural and elastic properties of CaTiO_3 , SrTiO_3 and MgSiO_3 perovskites at 0 GPa.

For all three phases, the cell parameters are predicted to within 1 or 2% of those measured, an excellent result. The elastic constants are also in quite good agreement with experiment for CaTiO_3 and SrTiO_3 although for MgSiO_3 the bulk modulus is overestimated by around 40%.

The lattice energies for the various phases used in the defect calculations are given in Table 5.3. In all cases, the minimised atomic coordinates from PARAPOCS were used as starting coordinates in the CASCADE calculations.

5.6 Calculation of defects and diffusion in SrTiO_3

SrTiO_3 has the ideal cubic perovskite structure with 5 ions in the unit cell. For all of the calculations carried out on this phase, a maximum region 1 size of 6.25\AA was used containing around 90 ions or 18 unit cells. In all cases, convergence of better than 5 kJmol^{-1} was obtained.

The vacancy formation enthalpies and corresponding Schottky defect enthalpies were first calculated assuming that vacancies would be isolated and non-interacting. In this case, the SrO Schottky has the lowest enthalpy per defect. Next, the formation enthalpy of vacancy clusters was considered, where

Table 5.2 Comparison of experimental and calculated lattice parameters and elastic moduli for the perovskites CaTiO₃, SrTiO₃ and MgSiO₃ at 0GPa.

CaTiO ₃	Measured	Calculated	Error %
a Å	5.367 ⁽¹⁾	5.49	2
b	5.443 ⁽¹⁾	5.51	1
c	7.643 ⁽¹⁾	7.79	2
vol Å ³	233.33 ⁽¹⁾	235.6	1
K Nm ⁻²	177 ⁽²⁾	198.6	12
μ Nm ⁻²	104 ⁽²⁾	117.5	13
SrTiO ₃			
a Å	3.905 ⁽²⁾	3.985	2
vol Å ³	59.947 ⁽²⁾	62.280	4
K Nm ⁻²	174 ⁽²⁾	193.7	11
μ Nm ⁻²	117 ⁽²⁾	116.6	>1
MgSiO ₃			
a Å	4.775 ⁽³⁾	4.824	1
b	4.929 ⁽³⁾	4.874	1
c	6.897 ⁽³⁾	6.884	>1
vol Å ³	162.32 ⁽³⁾	161.85	>1
K Nm ⁻²	245 ⁽⁴⁾	347	40
μ Nm ⁻²	184 ⁽⁴⁾	213	15

1. Kay and Bailey (1957) 2. Liebermann et al. (1977)
3. Horiuchi et al. (1987) 4. Yaganeh-Haeri et al (1988)

Table 5.3 Calculated values of lattice energy for phases used in this study.Values in kJmol⁻¹.

Phase	P GPa	Lattice energy
MgO	0	-3984.90
MgO	60	-3612.46
MgO	125	-3181.17
FeO	0	-3871.05
FeO	60	-3235.20
CaO	0	-3483.17
SrO	0	-3256.43
SiO ₂ <i>qtz.</i>	0	-12408.20
SiO ₂ <i>stv.</i>	60	-11642.09
SiO ₂ <i>stv.</i>	125	-11049.66
TiO ₂	0	-10854.76
Al ₂ O ₃	0	-12149.62
Al ₂ O ₃	60	-12837.57
Fe ₂ O ₃	0	-14473.02
Fe ₂ O ₃	60	-12832.74
MgSiO ₃	0	-16528.19
MgSiO ₃	60	-15219.82
MgSiO ₃	125	-14165.22
SrTiO ₃	0	-14224.08
CaTiO ₃	0	-14421.88

defects are bound. The formation enthalpy of all Schottky defects were found to be lower when defects were bound. The most favourable defect is now predicted to be the bound SrTiO₃ Schottky quintet with a formation enthalpy of 1024.72 kJmol⁻¹ (204.94 kJmol⁻¹ per defect). The complete set of results are given in Table 5.4.

Table 5.4 Predicted vacancy and Schottky defect formation enthalpies in SrTiO₃. Values of ΔH in kJmol⁻¹.

Isolated vacancy	ΔE	ΔE per defect
V _O	1857.3	1857.3
V _{Sr}	1970.2	1970.2
V _{Ti}	8484.0	8484.0
Vacancy cluster		
V _(O,Sr)	3718.6	1859.3
V _(Ti,2O)	11530.2	3843.4
Schottky (isolated)		
SrO	553.8	267.9
TiO ₂	1344.0	444.6
SrTiO ₃	1834.0	366.8
Schottky (cluster)		
SrO	462.1	231.0
TiO ₂	675.4	225.1
SrTiO ₃	1024.7	204.9

The equilibrium site fraction of defects has been calculated from Equation 5.13 for a range of temperatures (Table 5.5), where ΔH is assumed to be independent of temperature. Table 5.5 shows that even close to the melting temperature, the concentration of defects in SrTiO₃ will be low, only about 4 sites per million will be vacant.

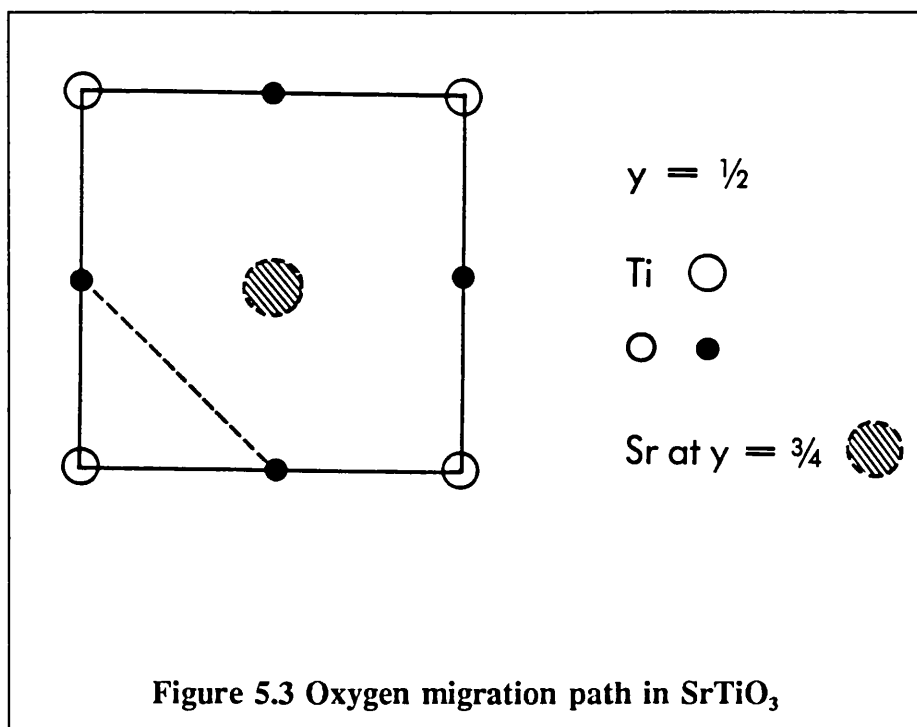
Table 5.5 Equilibrium site fraction of vacancies in SrTiO₃

T K	Site fraction X	n per cm ³
300	2.0×10^{-36}	1.7×10^{-13}
500	3.9×10^{-22}	0.3×10^2
1000	2.0×10^{-11}	1.7×10^{12}
1500	7.3×10^{-8}	6.1×10^{15}
2000	4.4×10^{-6}	3.7×10^{17}

* Assume that $\Delta E \approx \Delta G$

In order to find the diffusion activation enthalpy for oxygen in SrTiO₃, two adjacent oxygen vacancies were introduced and an oxygen interstitial fixed at various points between the two. The lowest energy path taken by the migrating oxygen is sketched in figure 5.3, with the saddle point energy being approximately halfway between the two sites. From Equation 5.16, the migration enthalpy is predicted to be 62 kJmol⁻¹. Adding one fifth of the formation enthalpy for the creation of a SrTiO₃ Schottky defect gives an activation enthalpy for intrinsic diffusion of 266.9 kJmol⁻¹.

The reported activation enthalpies range from 64.9 kJmol⁻¹ to 237 kJmol⁻¹ (Freer 1980) which correlates well with the calculated values, especially those for migration.



5.7 Simulation of defects and diffusion in CaTiO₃

For the simulation of defects and diffusion in CaTiO₃ perovskite, a region 1 size of 9.8 Å was used. In almost all calculations, this gave a convergence of better than 20 kJmol⁻¹, yet was small enough to permit a reasonable turnaround time on the CRAY.

5.7.1 Defect formation

The formation enthalpy for both isolated and bound vacancies were calculated as per the previous section (Table 5.6), as well as defect concentrations (Table 5.7). In CaTiO₃, although there are two distinct oxygen positions, all oxygens appear to have the same vacancy formation enthalpy. For the TiO₂ defects, the titanium was bound to one type 1 oxygen and one type 2.

Table 5.6 Predicted vacancy and Schottky defect formation enthalpies in CaTiO₃. Values of ΔH in kJmol⁻¹.

Isolated vacancy	ΔE	ΔE per defect
V _O	1860.2	1860.2
V _{Ca}	2067.7	2067.7
V _{Ti}	8333.5	8333.5
Vacancy cluster		
V _(Ca,O)	3847.9	1923.9
V _(Ti,2O)	11530.2	3843.4
V _(Ca,Ti,3O)	15378.1	3126.0
Schottky (isolated)		
CaO	444.8	222.4
TiO ₂	1199.3	399.7
CaTiO ₃	1560.2	312.1
Schottky (cluster)		
CaO	364.7	182.3
TiO ₂	675.4	225.1
CaTiO ₃	956.2	191.1

The bound CaO Schottky has a slightly smaller formation enthalpy per defect than the CaTiO₃ quintet. However, as the difference between them is less than the convergence limit, the stoichiometric quintet is taken to be the most likely defect with a formation energy of 956 kJmol⁻¹ (191.1 kJmol⁻¹ per defect).

The equilibrium site fraction of defects in CaTiO₃ (Table 5.7) is still small, only ten vacant sites per million close to the melting temperature at 2000 K, although this is more than in SrTiO₃ which has 4 sites per million vacant at the same temperature.

Table 5.7 Equilibrium site fraction of vacancies in CaTiO₃

T K	X	n per cm ³
300	5.0×10^{-34}	4.2×10^{-11}
500	1.0×10^{-20}	8.6×10^2
1000	1.0×10^{-10}	8.6×10^{12}
1500	2.2×10^{-7}	1.9×10^{16}
2000	1.0×10^{-5}	8.6×10^{17}

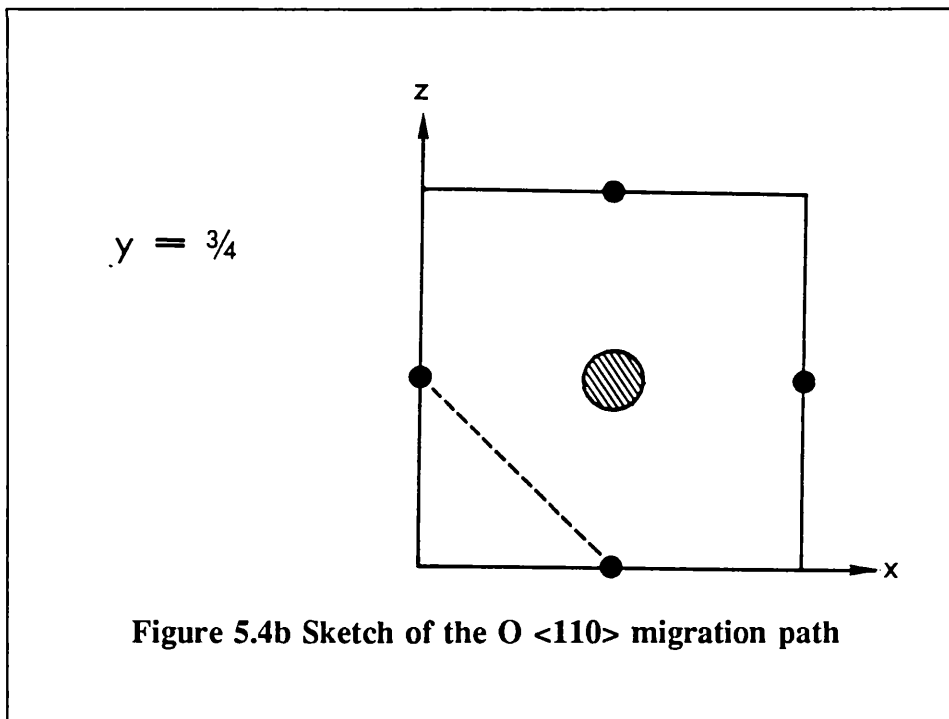
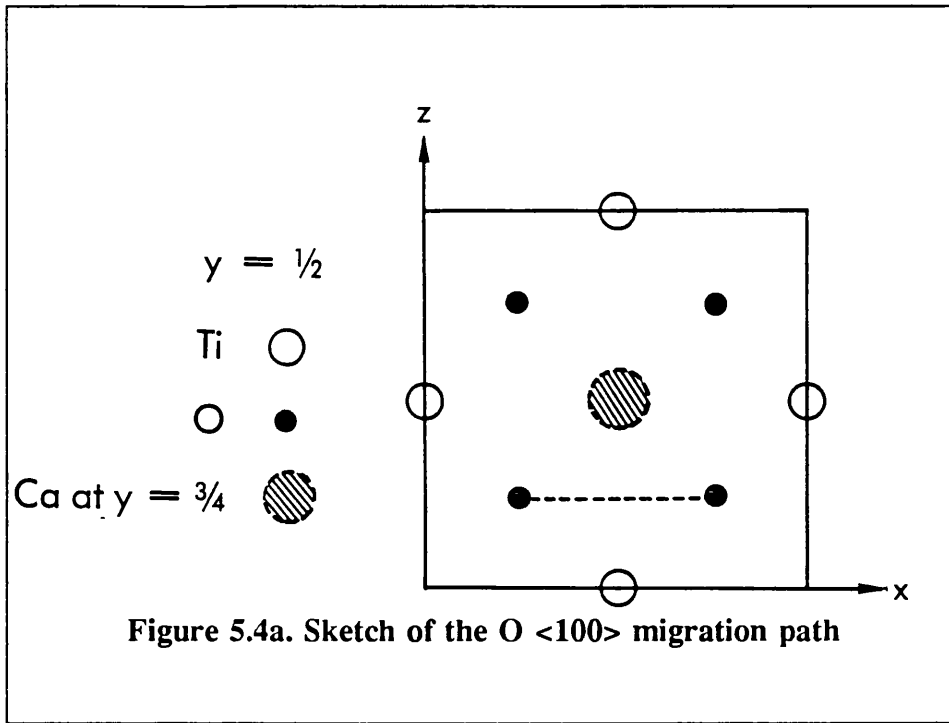
5.7.2 Diffusion in CaTiO₃

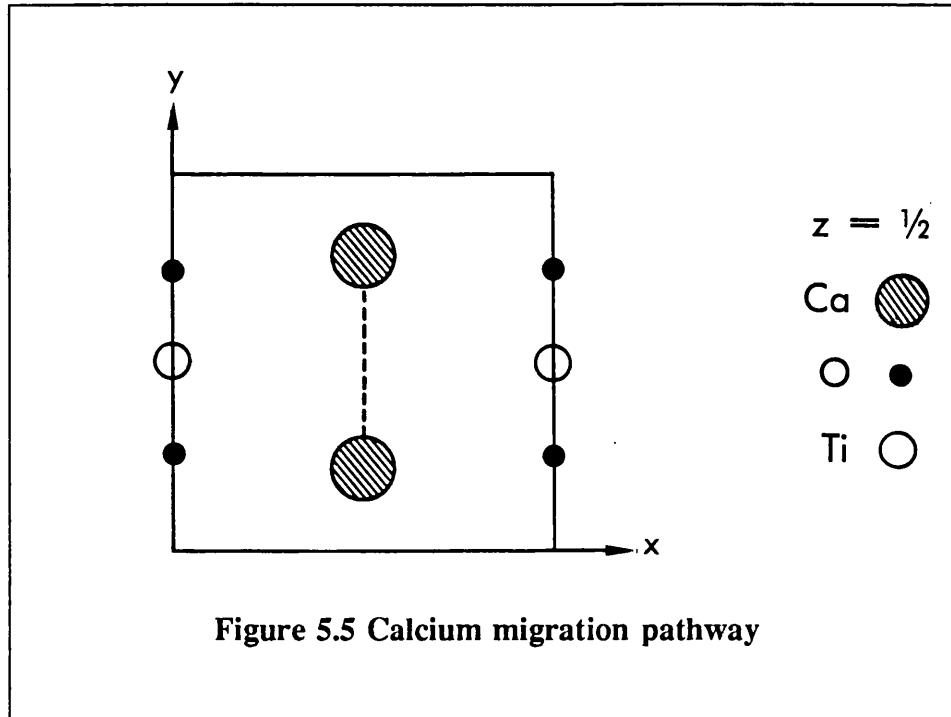
Diffusion activation enthalpies have been calculated for oxygen, calcium and titanium. Because of its orthorhombic symmetry, there are two likely diffusion pathways for the oxygen ion, along the $\langle 100 \rangle$ and $\langle 110 \rangle$ orthorhombic directions (Figure 5.4).

Diffusion in the $\langle 100 \rangle$ direction is predicted to be the most favourable with an activation enthalpy of 55.9 kJmol⁻¹ for migration and 247 kJmol⁻¹ for intrinsic diffusion. For the $\langle 101 \rangle$ direction, an activation enthalpy of 288.5 kJmol⁻¹ is required for migration and 479.0 kJmol⁻¹ for intrinsic diffusion, reflecting the greater jump distance.

Ca diffusion is assumed to take place along the $\langle 001 \rangle$ axis as sketched in figure 5.5. The saddle point is situated approximately half way between the two sites and, with Ca at this point the system has an enthalpy of 2426.6 kJmol⁻¹, giving an activation enthalpy for migration of 359 kJmol⁻¹ and 550.0 kJmol⁻¹ for intrinsic diffusion.

The diffusion of Ti through the lattice represents a somewhat more complex situation. Due to its 4⁺ charge, the Ti will be more attracted to or repelled by the ions it passes close to and therefore more limited in the path

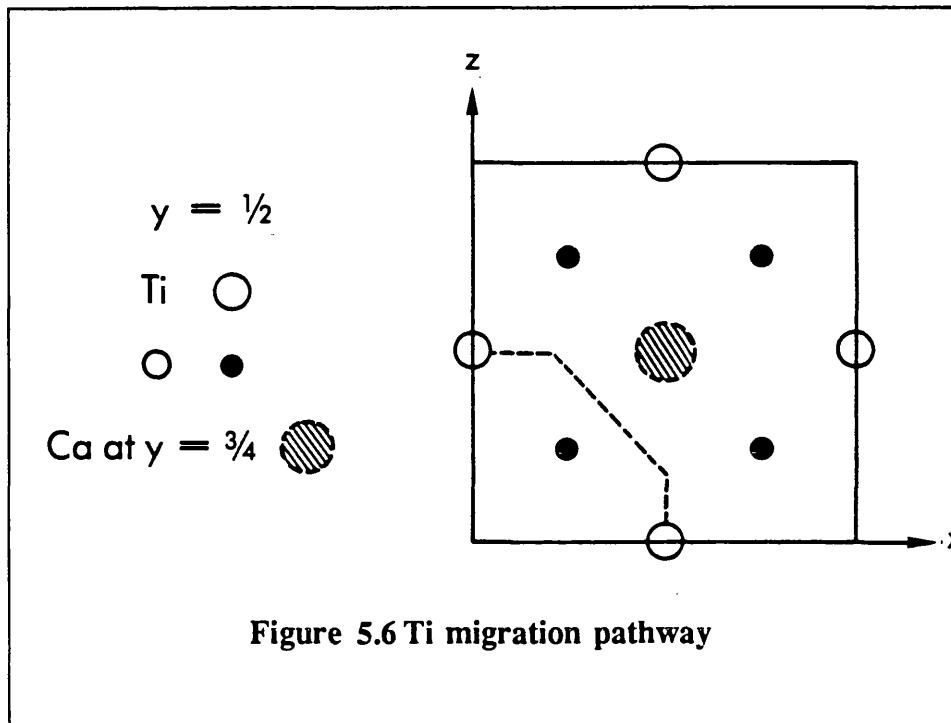




it can follow. The $\langle 110 \rangle$ migration direction has been investigated as the most likely path. An interstitial Ti was placed at some 15 positions between the two corresponding vacancies in order to find the lowest energy route (Figure 5.6). These calculations give an activation enthalpy of 693.7 kJmol^{-1} for migration and $894.97 \text{ kJmol}^{-1}$ for intrinsic diffusion, considerably higher than the corresponding values for O and Ca.

5.8 Summary of results for SrTiO_3 and CaTiO_3

In general, the defect calculations presented in the preceding sections show that defect formation enthalpies will be lowered by the binding of defects. Furthermore, the bound ABO_3 Schottky quintet will be the most favourable defect in terms of enthalpy per vacancy. Intrinsic defect



concentrations are predicted to be low, even at temperatures close to the melting temperature.

The O diffusion activation enthalpies for SrTiO_3 are predicted to be 62 kJmol^{-1} and 266.0 kJmol^{-1} in the extrinsic and intrinsic regimes respectively. These values compare extremely well with the reported values of 64.9 kJmol^{-1} to 237.0 kJmol^{-1} (Freer 1980).

The simulations of diffusion in CaTiO_3 indicate that Ti mobility will be the rate controlling factor in diffusion processes in this phase. The predicted activation enthalpies are 693.7 kJmol^{-1} and 884.8 kJmol^{-1} for extrinsic and intrinsic diffusion respectively. No comparable experimental data are available, however preliminary experimental data for the deformation of polycrystalline CaTiO_3 gives an activation enthalpy of around 800.0 kJmol^{-1} (Karato pers. comm.), where deformation takes place by some Newtonian creep law. In this situation, if diffusional creep is responsible for deformation, then Ti diffusion

could be expected to be the rate controlling process and this figure compares quite well with the predicted value. It should be noted that the actual diffusional mechanism in the real system could be more complex, hence the activation enthalpies presented here should be considered as upper limits.

On the basis of the above results, it is concluded that defect processes in materials with the perovskite structure can be well modelled using the simulation techniques described. It is then possible to justify using such techniques to model the behaviour of MgSiO_3 perovskite.

5.9 Defects and diffusion in MgSiO_3

Defect formation and diffusion activation enthalpies have been calculated for MgSiO_3 perovskite at 0K and simulated pressures of 0, 60 and 125 GPa. For the zero pressure calculations, a maximum region 1 size of 10 Å was used, containing 198 ions or about 20 unit cells. For the high pressure simulations, the input atomic coordinates were generated by PARAPOCS and the region 1 size reduced to 7Å reflecting the greater density.

5.9.1 Defects in MgSiO_3

Schottky defect formation enthalpies have been calculated for MgSiO_3 perovskite at simulated pressures of 0, 60 and 125 GPa (Table 5.8). Because of its orthorhombic symmetry, MgSiO_3 , like CaTiO_3 , has two distinct oxygen positions. However, the difference in formation enthalpy of the two oxygens was close to the convergence limit, so that the mean value was taken to be representative of both. This symmetry also means that the bound SiO_2 Schottky can have several geometries with differing O-Si bond lengths. The most favourable configuration, with Si bonded to one type 1 and one type 2 oxygen, has a formation enthalpy of 870 kJmol^{-1} . Where the silicon is bonded to two type two oxygens, the formation energy increases to $1030.0 \text{ kJmol}^{-1}$. All of the

high pressure calculations have therefore used the more favourable configuration.

At 0 GPa, the Schottky formation enthalpies are found to be lower when vacancies are bound (Table 5.8), as was the case for CaTiO_3 and SrTiO_3 . Similarly, the stoichiometric Schottky quintet has the lowest enthalpy per defect.

Table 5.8 Predicted vacancy and Schottky defect formation enthalpies in MgSiO_3 at 0 GPa. Values of ΔH in kJmol^{-1} .

Isolated vacancy	ΔE	ΔE per defect
V_{O}	2268.1	2268.1
V_{Mg}	2425.6	2425.6
V_{Si}	9297.2	9297.2
Vacancy cluster		
$V_{(\text{Mg},\text{O})}$	4507.2	2253.6
$V_{(\text{Si},\text{O})}$	11210.1	5606.4
$V_{(\text{Si},2\text{O})}$	13279.1	4426.4
$V_{(\text{Mg},\text{Si},3\text{O})}$	17654.5	3530.9
Schottky (isolated)		
MgO	707.2	353.6
SiO_2	1408.7	469.5
MgSiO_3	1994.5	398.9
Schottky (cluster)		
MgO	521.0	260.5
SiO_2	866.1	288.7
MgSiO_3	1126.4	225.3

The equilibrium site fraction of vacancies (Table 5.9) indicates that the number of intrinsically generated vacancies will be similar to CaTiO_3 close to the melting temperature. This is still a small number and implies that many defect processes could be controlled by the extrinsically generated vacancies.

Table 5.9 Equilibrium site fraction of vacancies in MgSiO_3 at 0 GPa.

T K	X	n per cm^3
300	6.1×10^{-40}	7.5×10^{-17}
500	2.9×10^{-24}	3.5×10^{-1}
1000	1.7×10^{-12}	2.1×10^{11}
1500	1.4×10^{-8}	1.7×10^{15}
2000	1.3×10^{-6}	1.6×10^{17}
2500	2.0×10^{-5}	2.5×10^{18}

At simulated high pressure, the defect formation enthalpies still show the bound defects to be more favourable. At 60 GPa (Table 5.10) the bound MgO Schottky has the lowest enthalpy per defect although this is only 23 kJmol^{-1} less than for the bound quintet. Since this is close to the convergence limit, the stoichiometric MgSiO_3 quintet is taken to be the more favourable.

At 125 GPa however, the MgO Schottky has an enthalpy per defect of 60 kJmol^{-1} less than that of the quintet (Table 5.11). This may indicate a tendency to move away from stoichiometry, or may be some artifact of the method at these simulated high pressures. However, as we are assuming a stoichiometric system, the energy per defect of the quintet will still be used in all of the diffusion calculations.

Table 5.10 Predicted vacancy and Schottky defect formation enthalpies at 60 GPa. Values of ΔH in kJmol^{-1}

Isolated vacancy	ΔE	ΔE per defect
V_{O}	2244.5	2244.5
V_{Mg}	2409.3	2409.3
V_{Si}	9573.4	9573.4
Vacancy cluster		
$V_{(\text{Mg},\text{O})}$	4407.5	2203.7
$V_{(\text{Si},2\text{O})}$	1335.4	4445.1
$V_{(\text{Mg},\text{Si},3\text{O})}$	17343.5	3468.7
Schottky (isolated)		
MgO	1040.1	520.0
SiO_2	2417.9	806.0
MgSiO_3	3469.6	693.9
Schottky (bound)		
MgO	795.1	397.5
SiO_2	1673.1	557.7
MgSiO_3	2102.4	420.5

Table 5.11 Predicted vacancy and Schottky defect formation enthalpies at 125 GPa. Values of ΔH in kJ mol^{-1}

Isolated vacancy	ΔE	ΔE per defect
V_{O}	2149.3	2149.3
V_{Mg}	2303.1	2303.1
V_{Si}	9625.5	9625.5
Vacancy cluster		
$V_{(\text{Mg},\text{O})}$	4187.5	2093.7
$V_{(\text{Si},2\text{O})}$	13063.3	4354.4
$V_{(\text{Mg},\text{Si},3\text{O})}$	17010.6	3402.1
Schottky (isolated)		
MgO	1271.3	635.6
SiO_2	2924.7	974.9
MgSiO_3	4203.7	840.7
Schottky (bound)		
MgO	1014.1	507.0
SiO_2	2013.7	671.2
MgSiO_3	2845.4	569.1

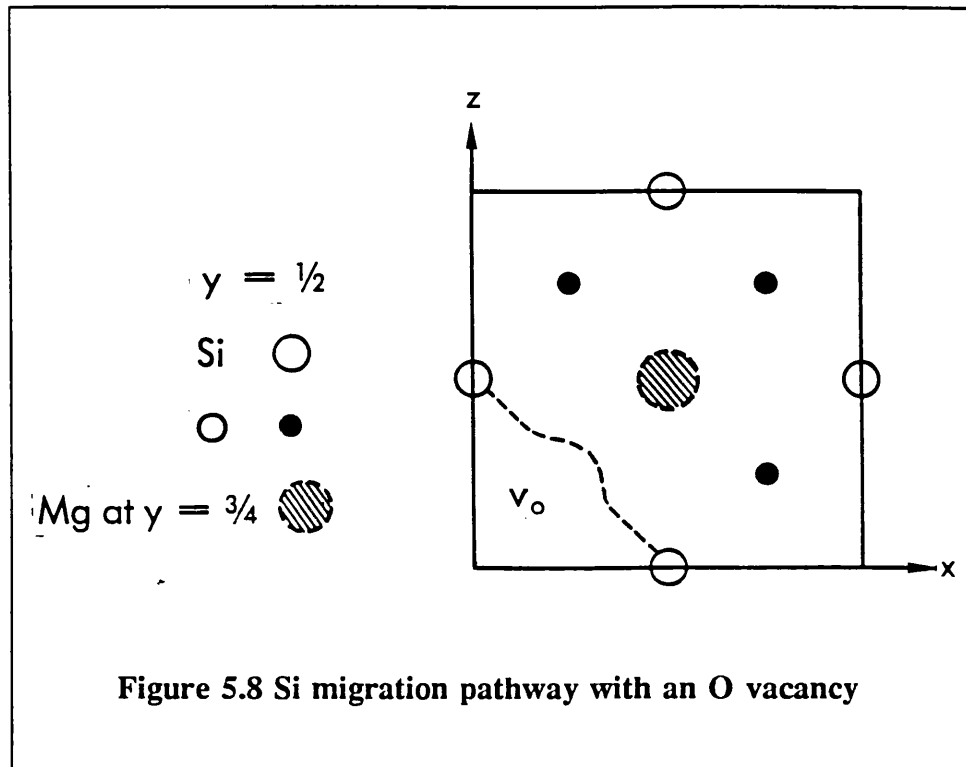
5.9.2 Diffusion in MgSiO₃ at 0GPa

The diffusion pathways of oxygen and magnesium at 0GPa have been calculated by Wall (1988) who found that oxygen would migrate along the $\langle 100 \rangle$ direction and magnesium along the $\langle 001 \rangle$ direction through the Mg₂O₄ octahedron. The activation enthalpies were predicted to be 93 kJmol⁻¹ and 464 kJmol⁻¹ for oxygen migration and intrinsic diffusion respectively. For magnesium, the migration enthalpy was found to 440 kJmol⁻¹ and for intrinsic diffusion 811 kJmol⁻¹. This section deals with the migration of silicon through the lattice at 0 GPa.

The migration of Si, like Ti in CaTiO₃, is likely to take place in the $\langle 110 \rangle$ orthorhombic direction. However, the more dense structure of MgSiO₃ will further restrict the route that Si can take. In order to determine this pathway, some 25 interstitial positions were sampled. Those with a convergence greater than 15 kJmol⁻¹ were rejected, although the majority converged in less than 7 kJmol⁻¹.

The Si migration pathway is sketched in Figure 5.7. The saddle point is 10180 kJmol⁻¹ giving a migration activation enthalpy of 887.6 kJmol⁻¹. Adding a fifth of the Schottky quintet enthalpy, gives an intrinsic diffusion activation enthalpy of 1112.8 kJmol⁻¹.

The value calculated for intrinsic diffusion is too high to be realistic and implies that bulk diffusion of silicon will not occur over geological timescales. Even in the extrinsic regime, movement of silicon will be difficult. However, in real systems diffusion may take place by more complex methods than those so far investigated, i.e. by coupled diffusion or diffusion in the presence of vacancies. It was therefore considered important to investigate such possibilities in MgSiO₃. The availability of computer time and memory limit the complexity of defect configurations which can be considered, so the simplest case of migration in the presence of an oxygen vacancy was chosen.



5.9.3 Silicon diffusion at high pressure

Since MgSiO_3 is stable only at depth in the Earth, the pressure dependence of diffusion processes is needed to extrapolate these results to meaningful values. Therefore silicon diffusion activation enthalpies have been calculated for simulated pressures of 125 GPa without an oxygen vacancy, and at 60 and 125 GPa for the case where an oxygen vacancy is present. In both cases, the migration paths were considered to be the same as for the zero pressure situation so less positions were sampled. The results are presented in Table 5.12 along with the zero pressure results for comparison.

Table 5.12 Activation enthalpies for Si diffusion at zero and simulated high pressure. Values of ΔH in kJmol^{-1}

Defect configuration	P GPa	ΔH_M	ΔH_D
$2V_{\text{Si}} + \text{Si}_i$	0	887.6	1112.8
	125	995.3	1564.4
$2V_{\text{Si}} + V_{\text{O}} + \text{Si}_i$	0	733.0	1183.4
	60	704.3	1545.3
	125	468.9	1037.98

For the situation where no O vacancy is present, values of migration and intrinsic diffusion activation enthalpies increase quite slowly over the pressure range 0 to 125 GPa. However, for the second configuration where an O vacancy is present, what is most surprising is that the activation enthalpies are actually decreasing. Over the pressure range 125 GPa, ΔH_M decreases by almost 275 kJmol^{-1} . For intrinsic diffusion, the value of ΔH first increases, but at pressures greater than 60 GPa begin to decrease. One possible reason for this behaviour is that the increasing pressure causes local rearrangement of ions around the defect cluster creating a more favourable pathway.

With these results it is now possible to calculate the pressure dependence of the activation processes, i.e. the activation volume V^* which is defined as:

$$V^* = d\Delta H/dP \quad (5.22)$$

For the case where diffusion occurs without any oxygen vacancies, the activation volumes are $0.86 \text{ cm}^3\text{mol}^{-1}$ for migration and $3.61 \text{ cm}^3\text{mol}^{-1}$ for intrinsic diffusion. Where an oxygen vacancy is present, the activation volume has been calculated for three pressure intervals (Table 5.13). All values of V^*

Table 5.13 Activation volumes for Si migration and diffusion with an oxygen vacancy present.

dP GPa	V^*_M cm ³ mol ⁻¹	V^*_D cm ³ mol ⁻¹
60	-0.66	6.03
65	-3.62	-7.8
125	-2.2	-1.16

are negative in the case of migration and for intrinsic diffusion at high simulated pressures. A negative activation volume was unexpected, as it implies that diffusion is actually becoming easier as the pressure increases and the structure becomes more dense. The effects of pressure are considered in more detail in section 5.10.

5.9.4 Diffusion of Mg at high pressures

At simulated pressures of 60 and 125 GPa, Mg is assumed to migrate along the <001> direction, as Ca in Figure 5.5. At both pressures, the saddle point was found to be at approximately halfway between the two sites. The results are shown in Table 5.14 along with the zero pressure results of Wall (1988) for comparison.

Table 5.14 Activation enthalpies for migration and diffusion of Mg at different pressures.

P GPa	ΔH_M kJmol ⁻¹	ΔH_D kJmol ⁻¹
0	440.6	811.0
60	591.4	1011.9
125	716.9	1285.9

At 125 GPa, the predicted activation enthalpies are now greater than those for Si at the same pressure. The corresponding values of activation volume are all positive and over the entire pressure range have values of $2.1 \text{ cm}^3\text{mol}^{-1}$ for the extrinsic regime and $4.96 \text{ cm}^3\text{mol}^{-1}$ for the intrinsic regime.

5.10 Defect reactions in MgSiO₃

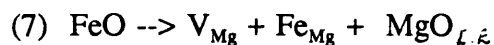
The results presented in section 5.8 show that the site fraction of intrinsic defects will be small, even at high temperatures. Furthermore, many of the intrinsic defect processes considered in the previous sections have extremely high activation enthalpies, therefore, the possibility of predominately extrinsic processes occurring in the real system should be thoroughly investigated.

In the extrinsic regime, the defect concentration is dependent on the concentration of impurities rather than temperature. In the Earth's lower mantle, MgSiO₃ coexists with (MgFe)O magnesiowustite and may incorporate a substantial amount of Fe into the system, up to (Mg₇₅,Fe₂₅)SiO₃ (Guyot et al. 1989). Small amounts of Al are also likely to be present (Madon 1990). In this section, the energetics of possible extrinsic reactions leading to vacancies in MgSiO₃ are assessed.

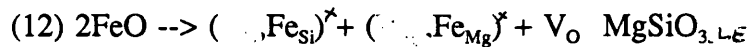
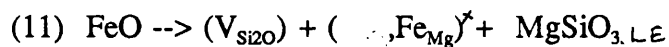
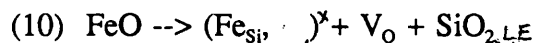
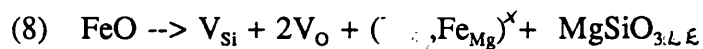
If excess MgO is incorporated into the system, then the following reactions are possible.

- (1) $\text{MgO} \rightarrow \text{Mg}_i + \text{O}_i$
- (2) $\text{MgO} \rightarrow 2\text{V}_\text{O} + \text{V}_\text{Si} + \text{MgSiO}_3 \quad \text{L.E.}$
- (3) $\text{MgO} \rightarrow \text{V}_{(\text{Si},2\text{O})} + \text{MgSiO}_3 \quad \text{L.E.}$
- (4) $2\text{MgO} \rightarrow \text{Mg}_i + \text{V}_\text{Si} + \text{V}_\text{O} + \text{MgSiO}_3 \quad \text{L.E.}$
- (5) $2\text{MgO} \rightarrow \text{Mg}_i + \text{V}_{(\text{SiO})} + \text{MgSiO}_3 \quad \text{L.E.}$
- (6) $3\text{MgO} \rightarrow 2\text{Mg}_i + \text{V}_\text{Si} + \text{MgSiO}_3 \quad \text{L.E.}$

The Fe in (MgFe)O can substitute directly by:



or in the manner of reactions 2 to 6 where



The energetics of reactions 1 - 12 have been calculated for pressures of 0 and 60 GPa and are given in table 5.15. The lowest enthalpy per vacancy by intrinsic Schottky defect formation is 225.3 kJmol⁻¹ at 0 GPa (Table 5.8).

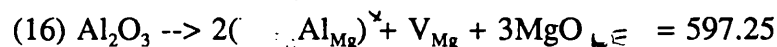
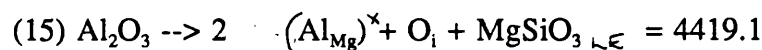
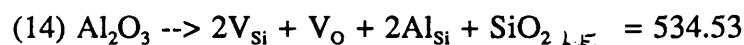
Table 5.15 Enthalpies of reaction and per vacancy at 0 and 60 GPa. Values in kJmol⁻¹

Reaction	ΔH reaction 0GPa	ΔH per vacancy	ΔH reaction 60 GPa	ΔH per vacancy
1	1786.9	none	1967.3	none
2	1288.1	429.0	2452.7	817.5
3	733.3	244.4	1707.8	569.3
4	1998.2	999.1	3074.1	1537.0
5	1643.2	821.6	2003.1	1001.5
6	2708.4	2708.4	3695.4	3695.4
7	198.7	none	27.0	none
8	1486.8	495.6	2479.7	826.57
9	2079.3	1039.6	2723.8	1361.9
10	667.7	667.7	1438.6	1438.6
11	932.1	310.68	1734.8	578.27
12	379.2	379.2	1500.3	1500.3

Of the reactions with MgO, only reaction 3 has a comparable enthalpy per vacancy created in this manner. At 60 GPa, this is still the most favourable reaction but is higher than the 420.5 kJmol⁻¹ of the intrinsic case (Table 5.,10).

The most favourable reaction for the incorporation of Fe into MgSiO₃ is the direct Fe - Mg exchange (reaction 7). At 60 GPa, this has an enthalpy of only 27 kJmol⁻¹, close to the convergence limit for the calculations. Reaction 11 combines the substitution with the formation of an SiO₂ Schottky triplet and has the lowest enthalpy per vacancy produced for all of the reactions involving FeO. At 60 GPa, it is comparable to the intrinsic case. All of the other reactions give high values for vacancy formation and so are considered unlikely to occur.

In the case of Al³⁺, the situation is more complex, since coupled substitution is required to maintain charge balance. Here, the case where MgSiO₃ is reacting with the oxide Al₂O₃ is considered. Some possible reactions and their respective enthalpies in kJmol⁻¹ for 0 GPa are given below.



At 0 GPa, Al³⁺ is most easily incorporated into the system by coupled substitution as in reaction 13. The creation of vacancies by reactions with Al₂O₃ are not well favoured compared to those with (MgFe)O. However, this may not be the case as pressure increases. No calculations for reactions with Al₂O₃ have been performed for simulated high pressures.

5.11 Discussion of results

The calculations performed at 0 GPa show that, like SrTiO₃ and CaTiO₃, the bound ABO₃ quintet will be the most favourable defect, and that the concentration of defects is low at all temperatures. At simulated pressures of 60 and 125 GPa, the binding of defects still leads to a reduction in the overall Schottky formation enthalpy, but at 125 GPa, the MgSiO₃ quintet is no longer the most favourable in terms of enthalpy per vacancy. The Mg \square Schottky has the lower enthalpy.

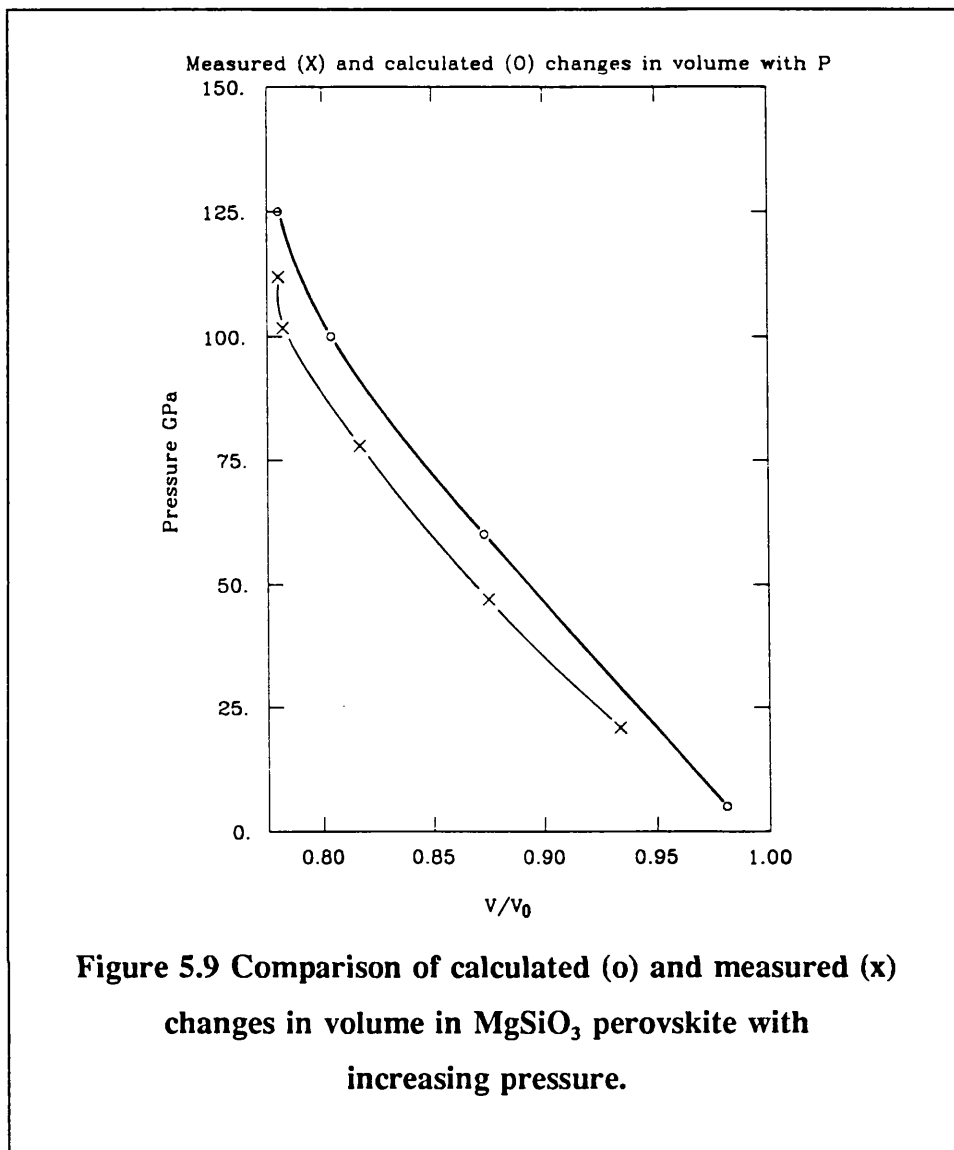
At zero pressure, Si has the highest diffusion activation enthalpy of all the species present. However, these values are reduced if the Si is allowed to migrate in the presence of an O vacancy. The results of the diffusion calculations at simulated pressures of 60 and 125 GPa show a number of interesting trends. Firstly, the intrinsic diffusion activation enthalpy for Si continues to have a high value, much higher than would be considered acceptable for mantle processes. Even if Si diffusion occurred by some more complex method, such as coupled diffusion, the high defect formation enthalpies involved would be unlikely to significantly reduce the intrinsic diffusion activation enthalpy. Furthermore, because of the compact structure of MgSiO₃ it is difficult to envisage how any coupled diffusion through the bulk lattice could be accommodated. Alternatively, the magnitude of ΔH could be a reflection of an unrealistic potential although the defect formation and diffusion activation enthalpies are on a par with those calculated for CaTiO₃, and in the case of O, for those associated with SrTiO₃. There is some justification then for concluding that diffusion in MgSiO₃ through the bulk of the lattice is only likely to occur by extrinsic processes.

Secondly, the Si activation parameters are predicted to decrease with increasing pressure giving rise to a negative activation volume. This infers that the movement of Si in MgSiO₃ becomes easier with depth in the mantle. This behaviour could possibly be due to changes in the structural distortion of

MgSiO₃ in response to increasing pressure allowing more freedom of movement for Si within the lattice. Experiments carried out at pressures of up to 30 GPa (Mao et al. 1991) have shown that the orthorhombic distortion actually increases with increasing pressure. Wall (1989) found that at simulated high pressures, the diffusion activation enthalpies for O, also gave a negative activation volume. Furthermore, the lowest enthalpy migration pathway for O changed from <100> at zero pressure to <110> at 100 GPa which could also be the result of increased structural distortion. Alternatively, the predicted negative activation volumes could be some artifact of the method caused by breakdown of the potential. It should be recalled that the short range parameters were fitted to oxides at room pressure conditions, far from those simulated here. Testing the reliability of the potential at such conditions is difficult since there are very few high pressure data for MgSiO₃ to use for comparison. One parameter which has been measured to pressures in excess of 100 GPa is the cell volume (Knittle and Jeanloz 1989). Figure 5.9 shows the change in V/V_0 with increasing pressure for both the experimental and calculated values. The resulting curve shows that the values calculated in this study are in good agreement with those measured and thus these high pressure calculations are likely to be showing real trends.

The final feature of note, is the change in the rate controlling species from Si to Mg at some pressure above 60 GPa. Such behaviour has also been postulated for (MgFe)₂SiO₄ Olivine (Stocker and Ashby 1978) where oxygen takes over from silicon as rate controlling species at depth in the upper mantle. Therefore at depth in the lower mantle, Mg will be the rate controlling species in the diffusional creep of MgSiO₃.

The extrinsic defect reaction calculations show that Fe substitutes easily for Mg in silicate perovskite and that this reaction becomes more favourable with increasing pressure. Jackson et al. (1987) proposed that Fe would substitute for Mg by entering the octahedral site thus displacing the Si to the dodecahedral site. The results of the simulations show that this situation is



extremely unlikely, since the configuration envisaged by the above authors has an enthalpy of 957 kJmol⁻¹ (Wright and Price 1989), far greater than for the simple Mg - Fe exchange.

The coupled Al substitution in reaction 13 is also an extremely favourable way of introducing impurities into the system. However the creation of vacancies by the introduction of Al is extremely unfavourable. The situation is somewhat more complex in the case of reactions involving Mg and Fe. At

60 GPa, the formation enthalpy per defect by reactions 3 and 11 is approximately 30% greater than that for the intrinsic case. However, both reactions lead to the formation of an SiO_2 pseudo Schottky defect. Looking back at Table 5.10, the formation enthalpy per defect of a bound SiO_2 Schottky is given as 557.7 kJmol^{-1} which is the same as that for reactions 3 and 11 within the limits of convergence! Therefore, it may well be as energetically favourable to create defects by extrinsic means at this pressure as by intrinsic means.

In conclusion, the calculation of defect enthalpies in MgSiO_3 perovskite show that defect populations at lower mantle conditions could well be controlled by reactions with co-existing $(\text{Mg,Fe})\text{O}$ magnesiowustite. The calculation of extrinsic and intrinsic diffusion activation enthalpies also supports predominately extrinsic processes. At depth in the mantle, probable distortions in the structure of MgSiO_3 perovskite allow easier movement of both O and Si, while restricting movement of the larger Mg ion. Movement of Mg is therefore predicted to be the rate controlling factor in the diffusional creep of MgSiO_3 perovskite at depth in the lower mantle.

CHAPTER 6: THE RHEOLOGY OF PEROVSKITES

6.1 Introduction

In Chapter 4, the results of creep experiments on two oxide perovskites were presented. It now seems appropriate to review the experimental findings for other oxides perovskites and once all the data are assembled, they can be compared to see if any similarities in behaviour are apparent. It may then be possible to make some comments on the behaviour of perovskites in general, thus attempting to answer the questions posed at the start of Chapter 3. In the following discussion, all crystallographic planes and directions will be referred to in pseudocubic indices unless otherwise stated.

6.2 Review of experiments

Beauchesne and Poirier have investigated the creep behaviour of three oxide perovskites: BaTiO₃ (Beauchesne and Poirier 1989), KTaO₃ and KNbO₃ (Beauchesne and Poirier 1990). A summary of the results are given in Table 6.1 along with those from this study for comparison.

The 2-4 perovskite BaTiO₃, is ferroelectric at room temperature and has tetragonal symmetry up to 373 K where it undergoes a transition to the cubic phase. At 1743 K it becomes hexagonal. BaTiO₃ is distorted from the ideal cubic structure by displacement of the Ti cation within the TiO₆ octahedra.

Beauchesne and Poirier (1989) carried out a series of high temperature creep experiments on this perovskite using the same methods as those described in Chapter 3. The above authors found that at temperatures between 0.75 and 0.92 T_M, BaTiO₃ deforms according to a Weertman type creep law with n = 3.6. From TEM analysis of the dislocation structures, the active slip

systems were found to be $\{100\} \langle 100 \rangle$ with accessory slip on $\{110\} \langle 110 \rangle$. At the higher end of the temperature range, climb processes led to the formation of polygonal dislocation walls. Scallop features, like those observed in CaTiO_3 , were also present in some samples.

KNbO_3 is a 1-5 perovskite which is orthorhombic at room temperature, becoming tetragonal at 593 K and then cubic at 783 K. Like BaTiO_3 , it shows low temperature ferroelectric behaviour and has a similar distortion from the ideal, with the Nb cation being off-centre in the NbO_6 octahedra.

The creep deformation of KNbO_3 (Beauchesne and Poirier 1990) showed similarities in behaviour to that of BaTiO_3 , deforming according to a power-law with $n = 3.7$. The dislocation structure was quite different however. The dominant dislocations were found to be edge with $\mathbf{b} = \langle 001 \rangle$. Abundant evidence for climb of dislocations was observed although the dislocation walls, so prominent in BaTiO_3 , were absent. Beauchesne and Poirier have attributed this latter observation to the low final strains in these samples.

KTaO_3 is cubic at all temperatures and forms a solid solution with KNbO_3 . Experiments on this phase (Beauchesne and Poirier 1990) were performed at temperatures between 0.87 and 0.99 T_M . The results were very different from those for other perovskites. In particular, KTaO_3 was found to deform by a Newtonian mechanism with $n = 1$. Little evidence was found for the climb of dislocations although slip still occurs on $\{100\}$ planes. Beauchesne and Poirier have interpreted this behaviour as being consistent with Harper-Dorn type creep.

No other experiments have been performed at high temperatures on single crystals of either CaTiO_3 or NaNbO_3 to the authors knowledge. There have been studies on polycrystalline CaTiO_3 (Yamada 1984, Karato 1991) and low temperature indentation tests (Doukhan and Doukhan 1986) on single crystal CaTiO_3 . However, since the methods used and experimental conditions

are so different from those of Beauchesne and Poirier and the present study they were not be used in the comparison.

Table 6.1 Summary of experimental creep data on oxide perovskites.

Phase	Compression axis	ln A	n	ΔH kJmol ⁻¹	g
BaTiO ₃	<110>	-38.0	3.6	469	30
KNbO ₃	<110>	-42.5	3.7	415	38
KTaO ₃	<110>	-11.0	1.0	292	21
NaNbO ₃	<100>	-92.0	5.3	192	13
CaTiO ₃	<100>	-39.1	3.3	444	24
CaTiO ₃	<110>	-37.9	2.7	280	15

6.3 Comparability of data.

Certain differences are present as regards the samples in Table 6.1 which must be taken into account when comparing the results. All were deformed at temperatures above the cubic transition except for CaTiO₃, which was probably tetragonal at the experimental temperature range sampled. The exact temperatures of the orthorhombic to tetragonal and tetragonal to cubic transitions are not well known. CaTiO₃ is certainly orthorhombic to 1273 K (Kay and Bailey 1957). Recent experiments by Wang et al. (1990) have indicated that the orthorhombic to tetragonal transition probably occurs at around 1531 K while examination of twin domains points to the cubic phase appearing somewhere above 1723 K. Although there is considerable uncertainty in the cubic case, it is unlikely that the cubic phase was reached during the bulk of the experiments.

Differences are also present as regards crystal orientation. BaTiO₃, KTaO₃ and KNbO₃ were all deformed with the compression axis parallel to the <110> pseudo-cubic direction. NaNbO₃ could only be cut from the boule with the compression axis along <100> while CaTiO₃ was deformed in both orientations. The results of NaNbO₃ and those for CaTiO₃ in the same orientation cannot be compared with the other results as CaTiO₃ clearly shows a dependence of creep rate on orientation.

The systematics approach, requires that conditions be directly comparable. The experiments on CaTiO₃ were performed at lower homologous temperatures than those for the other samples, hence normalization of data by melting temperature may not be appropriate. Similarly other normalization parameters are difficult to use due to the shortage of physical and thermodynamic data for these perovskites. All of the results in Table 6.1 however, were obtained using the same experimental and data analysis techniques. It may therefore be possible to justify making some general comments on the behaviour of perovskites from the above information although to assess them in terms of isomechanical series seems somewhat premature. A great deal more data must be collected before this can be attempted.

6.4 The rheology of perovskites

The first thing which is noticeable from examination of Table 6.1 is how differently these materials seem to behave. This is particularly the case for the three 1-5 perovskites NaNbO₃, KNbO₃ and KTaO₃ which all have very different values of $\ln A$, n , g and ΔH . Similarly CaTiO₃ and BaTiO₃ are both 2-4 perovskites and although they show similar dislocation features values of ΔH and g for comparable orientations are very dissimilar.

Beauchesne and Poirier (1989) concluded from their study of the oxide

perovskites BaTiO_3 , KTaO_3 and KNbO_3 that perovskites did not appear to constitute any obvious isomechanical series. These authors noted that more experiments were needed, particularly on perovskites such as CaTiO_3 and NaNbO_3 , before any possible isomechanical behaviour could be identified. Unfortunately, the data from this study seems only to have reinforced the premise that all perovskites behave in a different manner.

6.5 An analogue for MgSiO_3

Since perovskites do not appear to show isomechanical behaviour, it is necessary to assess which perovskite, if any, could serve as a good analogue for MgSiO_3 . On the basis of cation valence, the 1-5 perovskites are unlikely contenders and although BaTiO_3 is a 2-4 perovskite, its ferroelectric behaviour is not mirrored by MgSiO_3 . Of the perovskites studied, this leaves CaTiO_3 , which Beauchesne and Poirier (1989) have intimated could be a good analogue for the silicate perovskite. Both are 2-4 perovskites, both are orthorhombic and have the same distortion from the ideal structure although this is more pronounced in MgSiO_3 (Figure 6.1). On the basis of structure and cation valence then, CaTiO_3 appears to be the best candidate at the present time.

6.6 Deformation maps for perovskite

In order to investigate the deformation behaviour of perovskites further, it is useful to be able to extrapolate to conditions other than those sampled in the laboratory. Deformation mechanism maps provide the means to do this. The effects of grain size, pressure and activation parameters on deformation can then be assessed over a wide range of conditions. In this section, the methods used to construct the maps are described and then the maps and the data used in their construction presented.

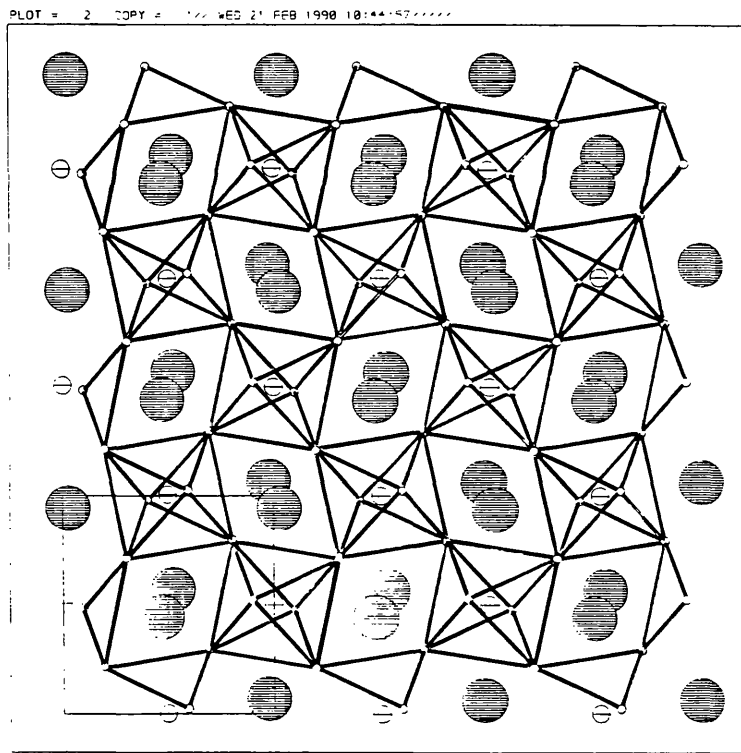
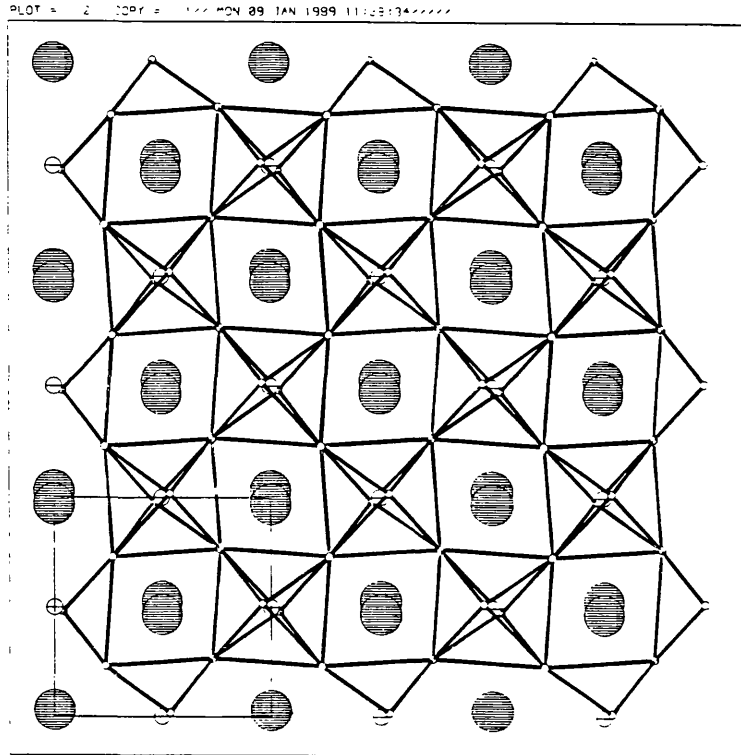


Figure 6.1 Structure of the perovskites (a) CaTiO_3 and (b) MgSiO_3 viewed down the y axis.

6.6.1 Method of construction

All of the deformation mechanism maps presented here were constructed following the method outlined by Frost and Ashby (1982) and using the Fortran program in Appendix 2. Only the fields for Herring-Nabarro creep (bulk diffusion), Coble creep (grain boundary diffusion) and power-law creep (dislocation movement) have been explicitly considered, since these are the most important mechanisms known at high temperatures.

The boundary between diffusional creep and dislocation creep mechanism is calculated by finding the points at which

$$\dot{\epsilon}_{\text{Diff}} = \dot{\epsilon}_{\text{plc}} \quad (6.1)$$

where the subscript Diff refers to bulk diffusion plus grain boundary diffusion and the subscript plc refers to power law creep. Solving for stress as a function of temperature, the position of the boundary is given by:

$$\sigma = [(b^2\mu^2\beta/Ad^2D_{\text{plc}}) D_{\text{Diff}}]^{(1/n-1)} \quad (6.2)$$

where b is the Burgers vector of dislocations, μ is the shear modulus, β the diffusional creep constant, A the Dorn constant and d the grain size. D_{Diff} is the effective diffusion coefficient for diffusional creep as defined by equation 2.6 in section 2.2, and D_{plc} the effective diffusion coefficient for power-law creep given by:

$$D_{\text{plc}} = D_{\text{Oplc}} \exp((-\Delta H_{\text{plc}} + P\Delta V)/RT) \quad (6.3)$$

The boundary between Herring-Nabarro and Coble creep is highly dependent on both grain size, d , and grain boundary width, δ , but is independent of stress. Therefore solving for temperature, the strain rate due to bulk diffusion equals that for grain boundary diffusion when

$$T = -\Delta H^*/R \ln(\delta/d) \quad (6.4)$$

where ΔH^* is the difference in activation enthalpy for the two processes.

To find the strain rate, the theoretical rate equations given in Chapter 2 are used (equations 2.2 to 2.6 for diffusion controlled creep and equation 2.9 for dislocation controlled creep). The program steps through values of stress and temperature solving the rate equations at each step for each mechanism. The values of strain rate are then summed to give the net strain rate for each stress/temperature value. By dividing the stress by twice the net strain rate, the viscosity (Chapter 7) can also be calculated. The boundary between each field is then plotted and the map contoured with either constant strain rate or constant viscosity contours.

6.6.2 Including the effects of pressure

In order to extrapolate the conditions to high temperatures and pressures, the elastic and volumetric parameters must be adjusted using the appropriate equations of state. For the bulk modulus (K), the pressure and temperature dependencies can be calculated by (Frost and Ashby 1982):

$$K_{(P,T)} = K_0[1+(1/K_0)K'(T-300)+(P/K_0)K^*] \quad (6.5)$$

where K_0 is the zero pressure bulk modulus, K' the temperature derivative and K^* the pressure derivative of the bulk modulus. The pressure and temperature dependence of the shear modulus can be calculated using the same equation and substituting the values of K and its derivatives for μ and its derivatives.

The effects of pressure on the magnitude of the Burgers vector is given by Frost and Ashby (1982) as;

$$\mathbf{b} = \mathbf{b}_0 \exp(-P/K_0) \quad (6.6)$$

where K is the bulk modulus. The pressure and temperature of the molecular and activation volumes can be calculated using the Murnaghan equation (Akaogi et al. 1984):

$$V_{TP} = V_0[1 + \alpha(T - 300)] * (PK^*/K_0 + 1)^{(-1/K^*)} \quad (6.7)$$

where V_0 is the zero pressure volume and α the volume coefficient of thermal expansion. Therefore, using equations 6.5, 6.6 and 6.7, the maps can be used to extrapolate data to any pressure and temperature.

6.7 Deformation mechanism maps for CaTiO₃

6.7.1 A rheological data set for CaTiO₃

Any maps produced by the methods outlined in the preceding sections will ultimately only be as reliable as the data used in their construction, therefore particular care is needed when compiling a rheological data set. The data used for construction of maps for CaTiO₃ is given in Table 6.2. For many of the required parameters, no data were available, and in these cases values for other similar materials were substituted or "guesstimates" made. The notes attached to Table 6.2 show how most of these were arrived at, but some require greater explanation and so are dealt with in more detail below.

The results of the creep experiments from Chapter 4, were refitted to the more complex Weertman creep law (equation 2.9) used in construction of the maps. The major uncertainty was in the value of the pre-exponential term for the diffusion coefficient. Equation 2.9 was rearranged to give:

$$AD_{Oplc} = RT\mu^2b^2\dot{\epsilon}/\Omega\sigma^n \exp(-\Delta H/RT) \quad (6.8)$$

Setting A to unity, gives a value of D_{Oplc} of $4.3 \times 10^{-7} \pm 0.4 \times 10^{-7} \text{ m}^2\text{s}^{-1}$.

Table 6.2 Rheological data set for CaTiO₃ perovskite.

Parameter	CaTiO ₃	Notes/refs.
Ω m ³	5.578x10 ⁻²⁹	Liebermann et al. 1977
b m	5.399x10 ⁻¹⁰	<100> distance.
T _m K	2248.0	Landolt Bornstein 1982
α K ⁻¹	4.0x10 ⁻⁵	Mean of BaTiO ₃ and SrTiO ₃ values (Williams et al. 1989)
Bulk diffusion	Ti diffusion	
ΔH Jmol ⁻¹	693000.0	This study - Chapter 5
D _o m ² s ⁻¹	5.0x10 ⁻⁶	See text
V* m ³	7.5x10 ⁻³⁰	See text
Grain boundary diffusion		
ΔH Jmol ⁻¹	465000.0	Assumed to be 0.6 ΔH_{bulk}
D _o m ² s ⁻¹	5.0x10 ⁻⁶	As D _{obulk}
δ	1.14x10 ⁻⁹	No data - value for olivine (Ranalli and Fischer 1984)
Power-law creep		
ΔH Jmol ⁻¹	280000.0	This study - Chapter 4
D _o m ² s ⁻¹	7.5x10 ⁻⁷	See text
V*	3.0x10 ⁻²⁹	See text
n	2.75	This study - Chapter 4
A	1.0	See text
Elastic moduli		
K Nm ⁻²	1.77x10 ¹¹	Liebermann et al. 1977
dK/dT Nm ⁻² K ⁻¹	-16.0x10 ¹¹	No data - estimated
dK/dP	3.5	No data - estimated
μ Nm ⁻²	1.04x10 ¹¹	Liebermann et al. 1977
d μ /dT Nm ⁻² K ⁻¹	-30.0x10 ⁶	No data - estimated
d μ /dP	2.5	No data - estimated

Of the diffusional parameters, the pre-exponential diffusion coefficient is also the most difficult to evaluate since no data are available for D_0 for a 4+ cation in any 2-4 perovskite. The so called compensation law is an empirical relationship between the pre-exponential and the activation enthalpy and is expressed as:

$$\Delta H = a + b \log D_0 \quad (6.9)$$

where a and b are constants. The compensation law should be valid all species in a material (Lasaga 1982). Using the data for perovskites given by Freer (1980), an attempt was made to find the values of a and b for perovskite. However, the spread of values was so large that it was concluded that in these materials, no clear correlation between ΔH and D_0 exists. Therefore the value of D_0 must be 'guesstimated'. The values of D_0 for Ti in single crystal rutile as given by Freer (1980) lie in the range 4.6×10^{-6} to 6.8×10^{-7} . Using these figures as a guide, a value of D_0 for Ti in CaTiO_3 of 2.6×10^{-7} was used as a starting point for both lattice and grain boundary diffusion. The estimation of the activation volume is dealt with in the following section.

6.7.2 A deformation mechanism map for CaTiO_3

Figure 6.2 is a simple deformation mechanism map for CaTiO_3 with a grain size of 2.5mm, close to that used in the experiments. The data points are those from experiments with the compression axis parallel to the $\langle 110 \rangle$ axis. Fine tuning of the value of D_{Oplc} was performed to bring the strain rate contours in line with the experimentally observed values. This final value of 7.5×10^{-7} was within the error range calculated in the previous section. At this grain size, the whole of the map is dominated by dislocation controlled creep. At the lower end of the temperature range, climb will not be active and therefore the creep rate will be controlled by the glide of dislocations. The current version of the program does not explicitly include low temperature mechanisms and therefore the position of the boundary is not calculated.

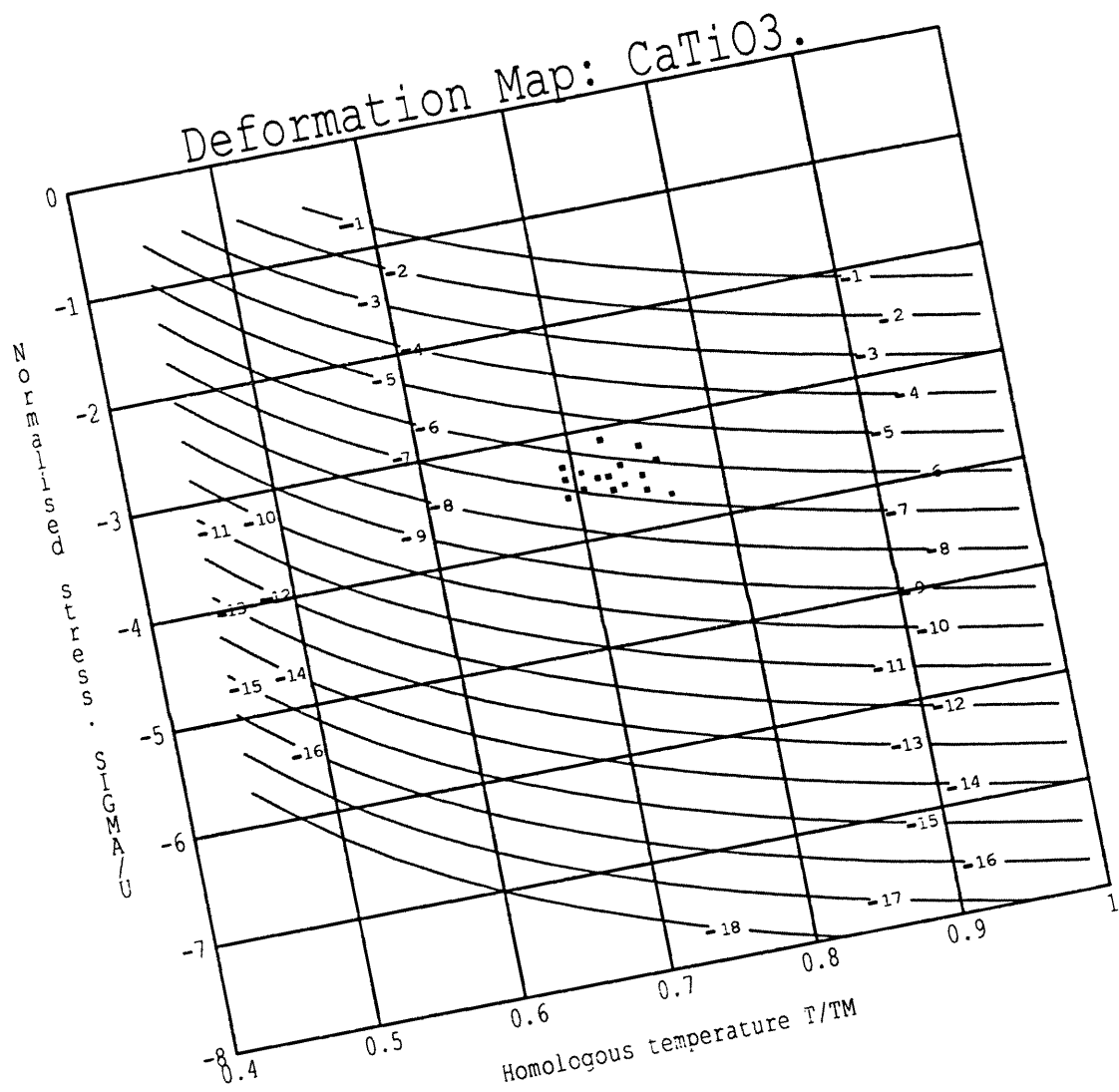


Figure 6.2 Deformation map for CaTiO₃, $d = 2.5$ mm
Contours are labelled with log strain rate.

The diffusional creep field does not appear until the grain size is reduced to $10\mu\text{m}$ (Figure 6.3) and even then does not cover much of the map. Increasing the values of D_0 for diffusion has a significant effect on the map at this grain size. Figure 6.4 shows a map computed with D_{OGB} increased to 2.5×10^{-3} , the boundary between power-law and diffusional creep has now moved up, increasing the field of importance of diffusional processes. At this grain size, Coble creep dominates the diffusional field. One feature of note is the downward curve of the diffusion/power-law boundary, which can be explained in terms of the relative values of activation enthalpy for dislocation and diffusion creep mechanisms

6.7.3 The effects of pressure

At ambient pressure, the value of the activation volume has no effect on the maps, but if the maps are to be extrapolated to higher pressures, then the magnitude of the activation volume, V^* , will be very important. The value of V^* for diffusion is usually taken to be some fraction of the molecular volume close to the volume of the rate controlling ionic species. In the case of metals and some simple oxides, the activation volumes for both diffusion and dislocation climb are assumed to be equal, however, this assumption is unlikely to be valid for more complex materials (Poirier 1978) and so each must be estimated separately.

The creep activation enthalpy is close to that calculated for intrinsic O diffusion in section 5.6.2. Therefore, it is possible that the climb of edge dislocations could be controlled by the mobility of O, in which case the activation volume would be close to that of O. Alternatively, diffusion processes along the dislocation core could be controlled by more complex coupled or molecular diffusion as proposed for olivine by Jaoul (1990). As a starting point, V_{plc}^* is taken to be $1/5$ of the molecular volume while V_{Diff}^* is assigned a value some 25% smaller.

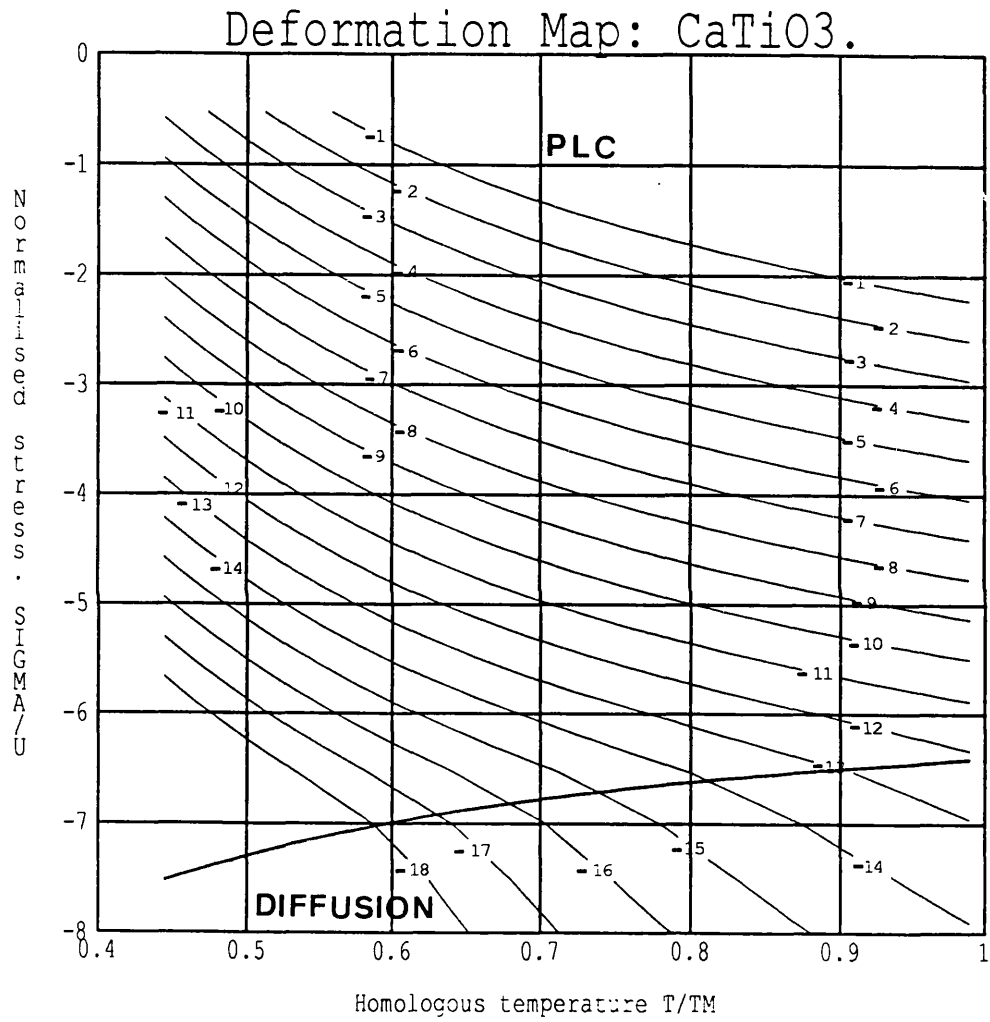


Figure 6.3 Deformation map for CaTiO₃ with a grain size of 10 μm. Contours labelled with log strain rate.

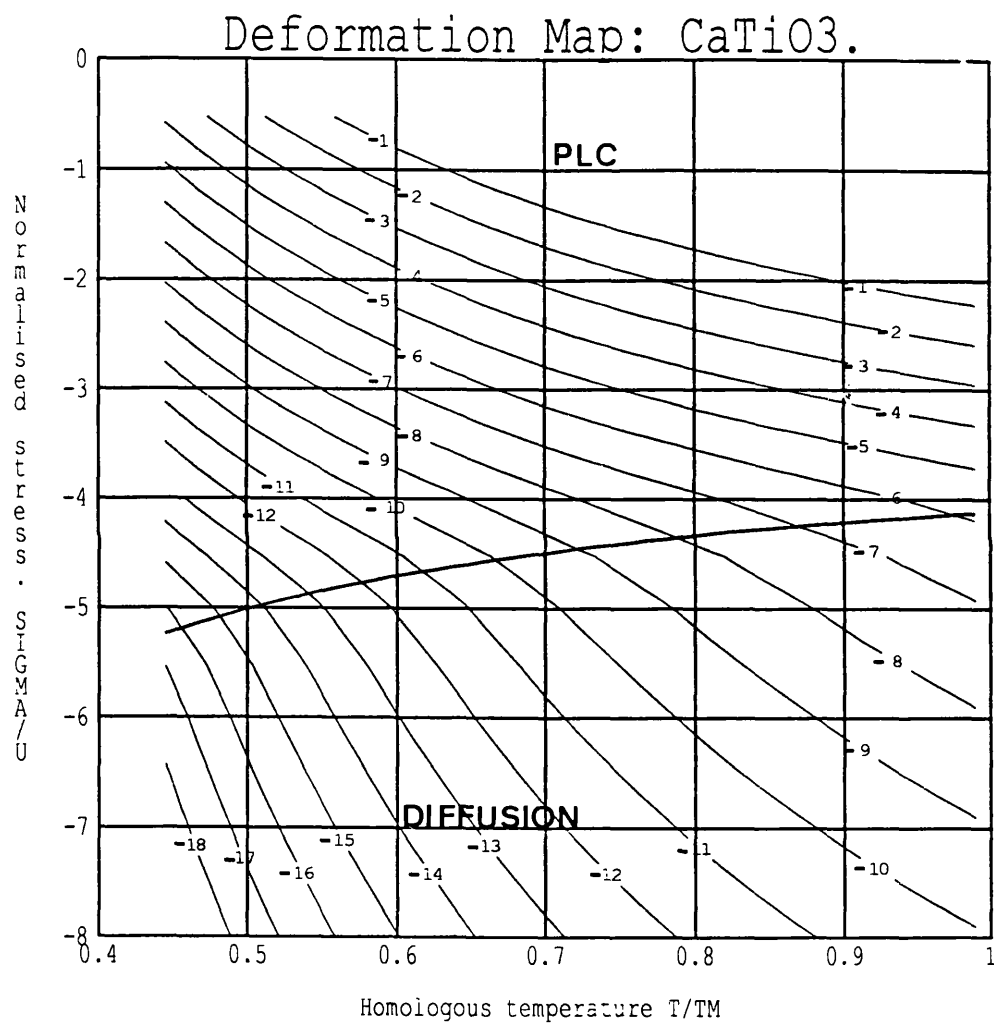


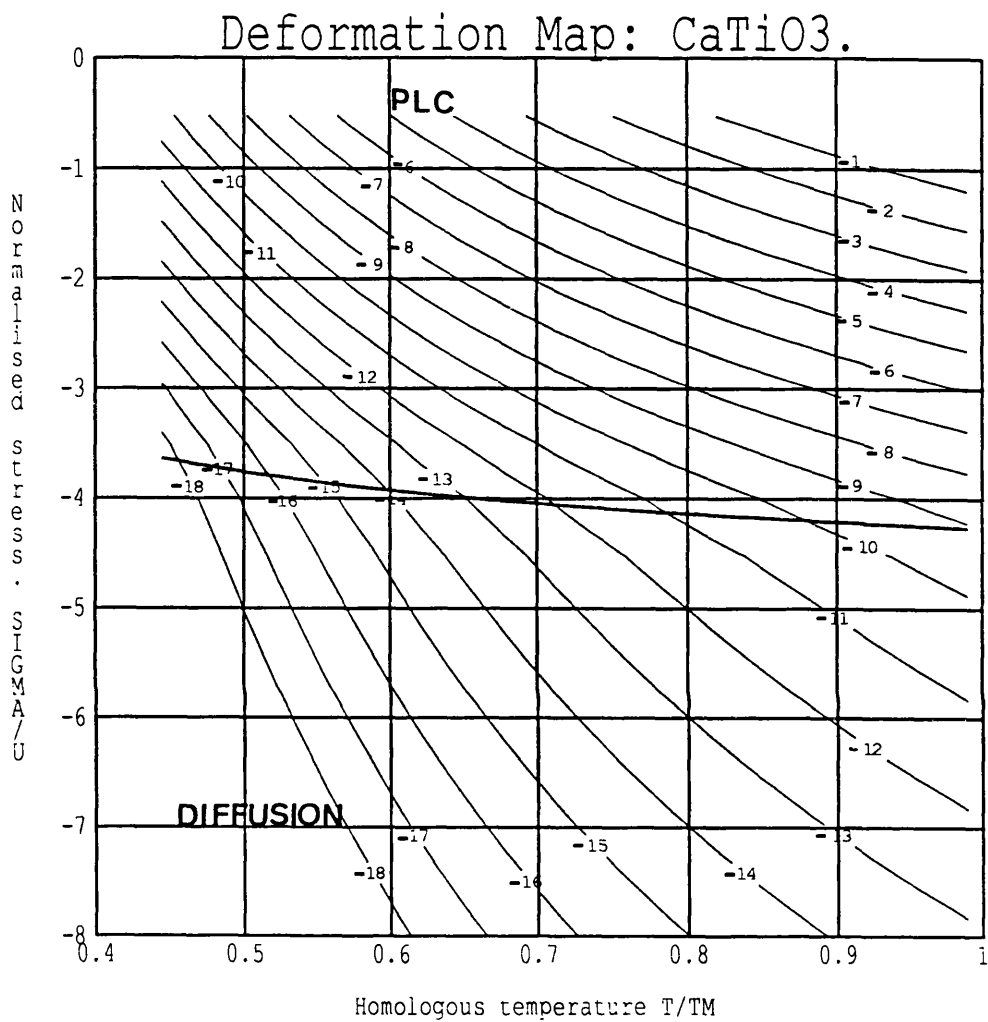
Figure 6.4 Deformation map for CaTiO₃ computed using $D_{Oplc} = 2.5 \times 10^{-3} \text{ m}^2 \text{ s}^{-1}$. Contours labelled with log strain rate.

Figure 6.5 shows a map computed using the above values of V^* and pressure of 10 GPa. The strain rate contours have been shifted up the map and the boundary now has a positive slope which still bisects the map despite the increased grain size of 0.1 mm. This behaviour can be understood in terms of the relative activation volumes for diffusion and dislocation creep mechanisms, the former being smaller than the latter. The larger power-law creep activation volume serves to reduce the size of the power-law field. When the activation volume for creep is decreased, as in Figure 6.6, the boundary again has a negative slope and a much higher pressure is needed to reverse it. Decreasing V_{plc}^* also changes the position of the boundary and strain rate contours. Increasing the value of V_{diff}^* has the same effect.

6.7.4 Discussion

The values of V^* as well as those of D_0 have a considerable effect on the maps and until these values have been determined, the maps presented here can only be speculative. Similarly, the calculated values of diffusion activation enthalpy, as noted in Chapter 5, must be considered as upper limits since diffusion in the real system may occur by some lower enthalpy process.

The maps presented here, show that deformation in CaTiO_3 will take place by some dislocation controlled mechanism at all grain sizes above 10 μm at zero pressure. With increasing pressure, low temperature dislocation creep is replaced by Coble creep. The slope of the boundary separating dislocation and diffusional mechanisms has a negative slope, which reverses at some pressure, depending on the value of the activation volume.



**Figure 6.5 Map for CaTiO₃ at 10 GPa with $d = 0.1\text{mm}$
and $V_{\text{plc}}^* = 2.05 \times 10^{-29} \text{ m}^3$. Contours labelled with
log strain rate.**

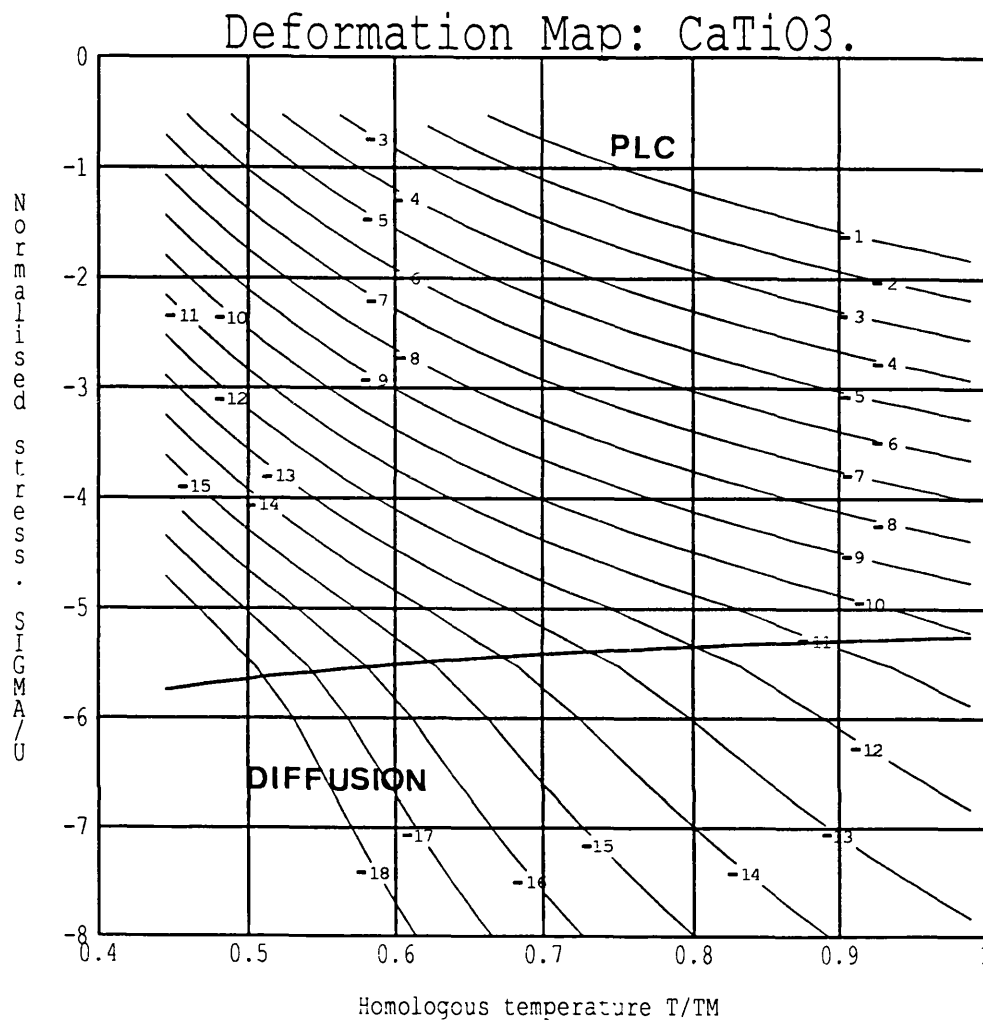


**Figure 6.6 Map for CaTiO₃ at 10 GPa with $d = 1\text{mm}$
and $V_{\text{plc}}^* = 8.5 \times 10^{-30} \text{ m}^3$. Contours labelled with
log strain rate.**

6.8 Deformation mechanism maps for MgSiO₃

6.8.1 A rheological data set for MgSiO₃

Compiling a rheological data set for MgSiO₃ presents similar problems to those associated with CaTiO₃. Once again, the lack of data for parameters such as D_0 means that guesstimates must be made, and in general, the same approach is made in making these guesses. All of the values for bulk diffusion have been taken from Chapter 5, with the exception of D_0 . Diffusion of the 4+ cation in MgSiO₃ is expected to be much slower than in CaTiO because of the greater density. In the absence of any other data, the value for Si diffusion in olivine (Jaoul 1990) is used as a starting point.

Assessing the values of dislocation creep parameters is somewhat more difficult. If MgSiO₃ follows CaTiO₃, then the activation enthalpy for creep should be close to that of the activation enthalpy for O diffusion. The activation enthalpy for creep is then the activation enthalpy for O diffusion as calculated by Wall (1988). The activation volume for creep is again taken to 1/5 of the molecular volume.

Several trial maps were constructed to assess the validity of the above values and assess the effect of increases and decreases in the values of D_0 and V_{plc}^* . The values chosen as most representative were then used to construct the maps.

6.8.2 Deformation mechanism maps with contours of constant strain rate

The maps for MgSiO₃ have been constructed for pressures of 60 and 125 GPa, representative of the middle and base of the lower mantle respectively. Grain size in the lower mantle is one of the great unknowns, but is assumed to be in the order of 1.0 to 0.1mm, the dominant grain size of upper mantle xenoliths. Accordingly, maps have been produced for a range of

Table 6.3 Rheological data set for MgSiO₃

Parameter	MgSiO ₃	Notes/refs
Ω m ³	4.069x10 ⁻²⁹	Horiuchi et al. 1987
b m	4.77x10 ⁻¹⁰	<100> distance
T _m K	3000	Heinz and Jeanloz 1987
α K ⁻¹	2.2x10 ⁻⁵	Ross and Hazen 1989
Bulk diffusion	Si diffusion	
ΔH Jmol ⁻¹	744000.0	This study - Chapter 5
D ₀ m ² s ⁻¹	3.5x10 ⁻¹⁰	See text
V* m ³	-2.2x10 ⁻³⁰	This study - Chapter 5
Grain boundary diffusion		
ΔH Jmol ⁻¹	478000.0	Assumed to be 0.6 ΔH_{bulk}
D ₀ m ² s ⁻¹	3.5x10 ⁻¹⁰	As D _{Obulk}
δ m	1.14x10 ⁻⁹	No data - as CaTiO ₃
Power-law creep		
ΔH Jmol ⁻¹	465000.0	See text
D ₀ m ² s ⁻¹	3.7x10 ⁻⁷	See text
V* m ³	6.5x10 ⁻³⁰	See text
n	3.0	No data - estimated
A	1.0	As for CaTiO ₃
Elastic moduli		
K Nm ⁻²	1.77x10 ¹¹	Yeganeh-Haeri et al. 1988
dK/dT Nm ⁻² K ⁻¹	-20.0x10 ⁶	Yeganeh-Haeri et al. 1988
dK/dP	4.0	Yeganeh-Haeri et al. 1988
μ Nm ⁻²	1.83x10 ¹¹	Yeganeh-Haeri et al. 1988
d μ /dT Nm ⁻² K ⁻¹	-36.0x10 ⁶	Yeganeh-Haeri et al. 1988
d μ /dP	2.6	Yeganeh-Haeri et al. 1988

grain sizes. In Chapter 5, the simulation results indicated the possibility of Mg becoming the rate controlling species in MgSiO_3 , and therefore, maps have been constructed using both Mg and Si diffusion activation enthalpies. Lower mantle conditions are shaded on each of the maps assuming mantle stresses in the range 1 to 10 MPa (Ranalli 1987) and with temperatures taken from the Brown and Shankland (1981) and Stacey (1977) geotherms for the appropriate depths.

Figures 6.7 and 6.8 show maps constructed at 60 GPa assuming Si and Mg to be the rate controlling species respectively. Strain rates in the mantle are assumed to be constant with a value of 10^{-15} to 10^{-16} s^{-1} (Ranalli 1986), and both of these maps have reproduced mantle conditions well. Both predict that power-law creep will be the dominant deformation mechanism at this depth. The only difference between the two is the position of the boundaries. Decreasing the grain size to 50 μm changes the position of the boundaries so that for Si diffusion (Figure 6.9) mantle conditions just overlap the boundary between Coble and power-law creep. For Mg diffusion however (Figure 6.10), Herring-Nabarro creep appears to be the dominant mechanism.

The dominant effect of increasing the pressure, is to shift the boundary between dislocation and diffusional creep mechanisms up, thus decreasing the range of the power-law field. At 125 GPa, if Si mobility controls diffusion then for a grain size of 1.0 mm (Figure 6.11), Herring-Nabarro creep is more likely to control deformation. As grain size decreases, Coble creep becomes more dominant and strain rates decrease until at 50 μm (Figure 6.12), a strain rate of 10^{-13} is predicted for mantle conditions. The situation is somewhat different if Mg mobility is rate controlling at this depth. For grain sizes of 1.0 mm (Figure 6.13), mantle conditions straddle the boundary between power-law and Herring-Nabarro creep, with strain rates being an order of magnitude higher than at 60 GPa. Reducing the grain size to 50 μm , lowers strain rates and places mantle conditions well within the Herring-Nabarro field.

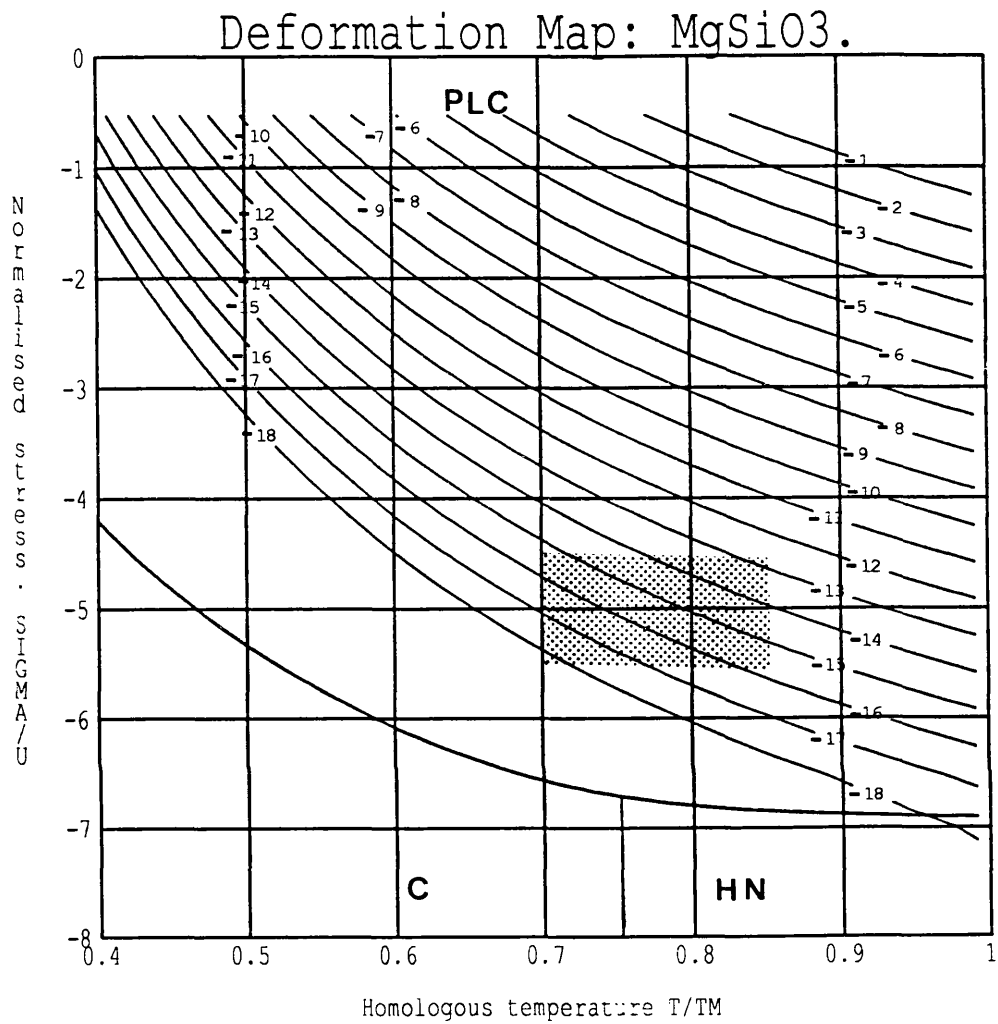


Figure 6.7 Map for MgSiO₃ at 60 GPa with Si as the rate controlling species and $d = 0.5$ mm. Contours are labelled with log strain rate.

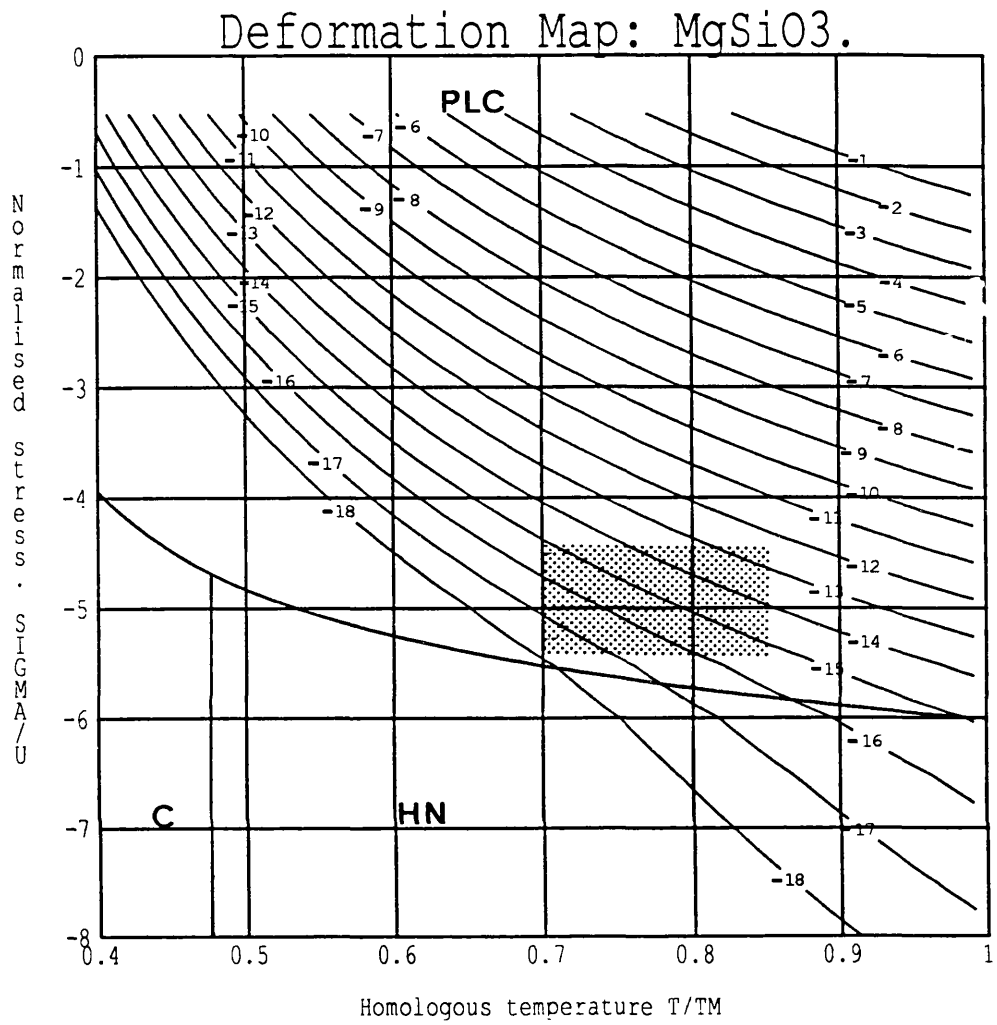


Figure 6.8 Map for MgSiO₃ at 60 GPa with Mg as the rate controlling species and $d = 0.5\text{mm}$. Contours labelled with log strain rate.

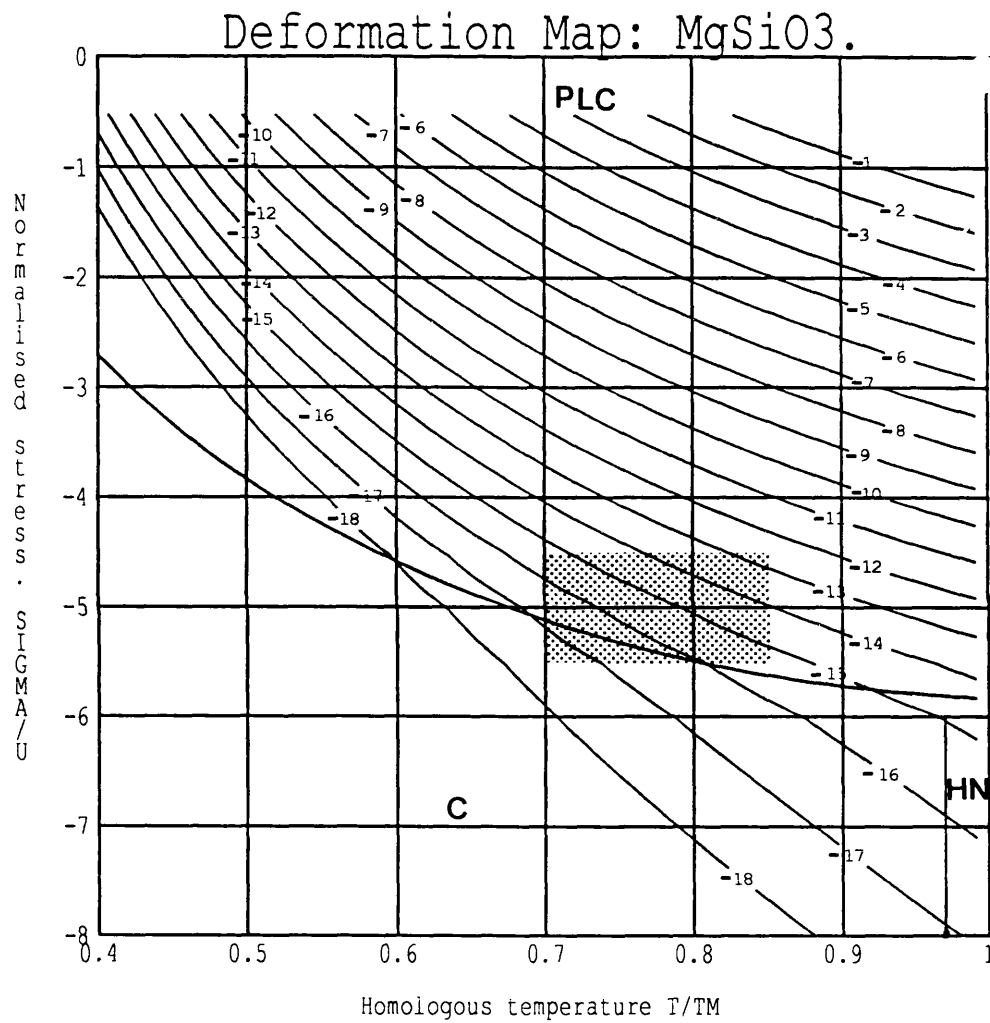


Figure 6.9 Map for MgSiO₃ at 60GPa with Si as the rate controlling species and d = 50 μm. Contours labelled with log strain rate.

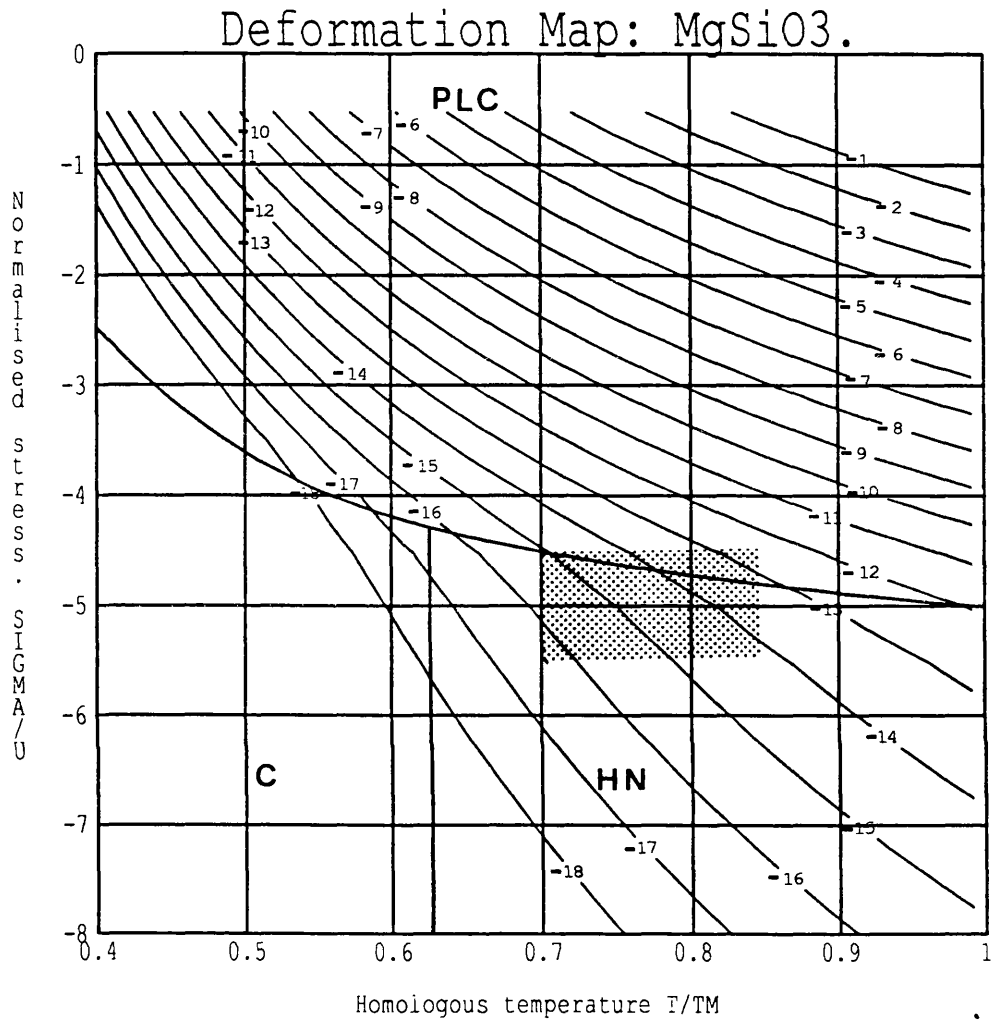


Figure 6.10 Map for MgSiO₃ at 60 GPa with Mg as the rate controlling species and $d = 50 \mu\text{m}$. Contours labelled with log strain rate.

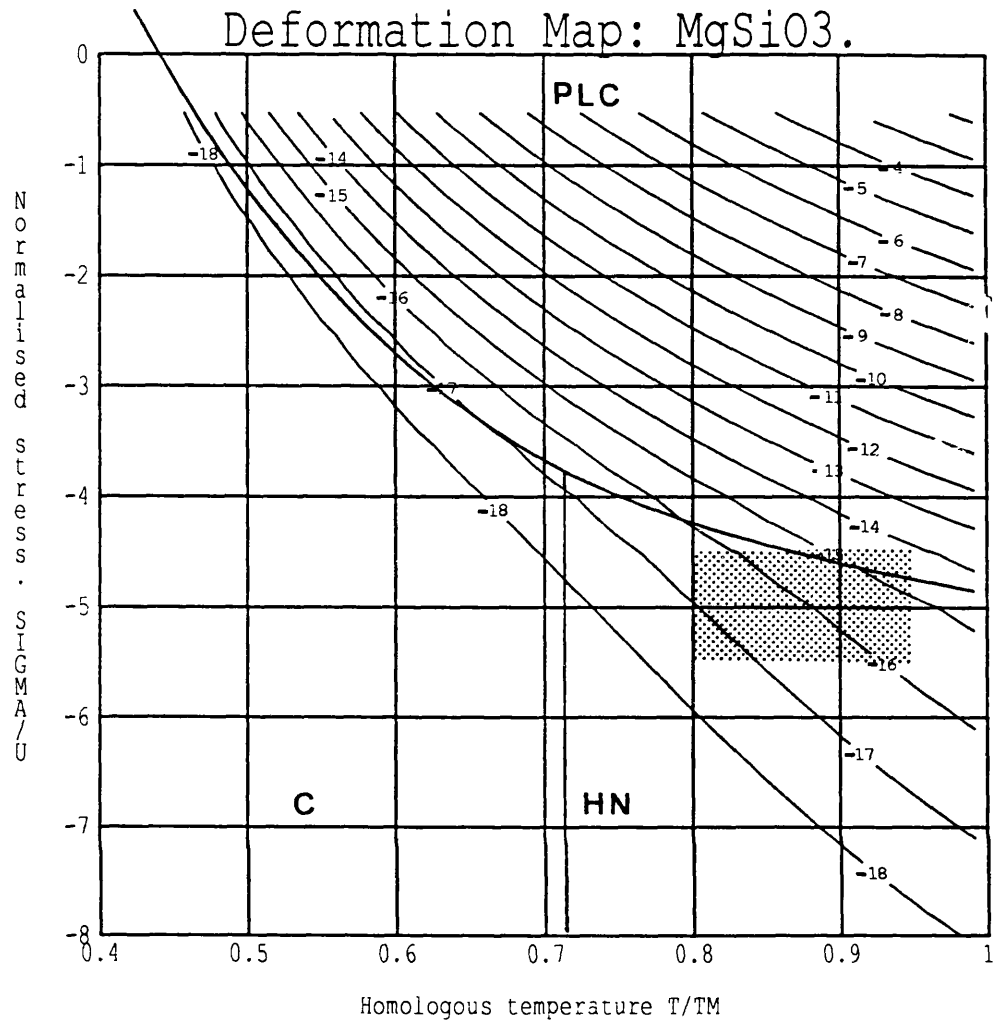


Figure 6.11 Nap for MgSiO₃ at 125 GPa with Si as the rate controlling species and $d = 1\text{mm}$. Contours labelled with log strain rate.

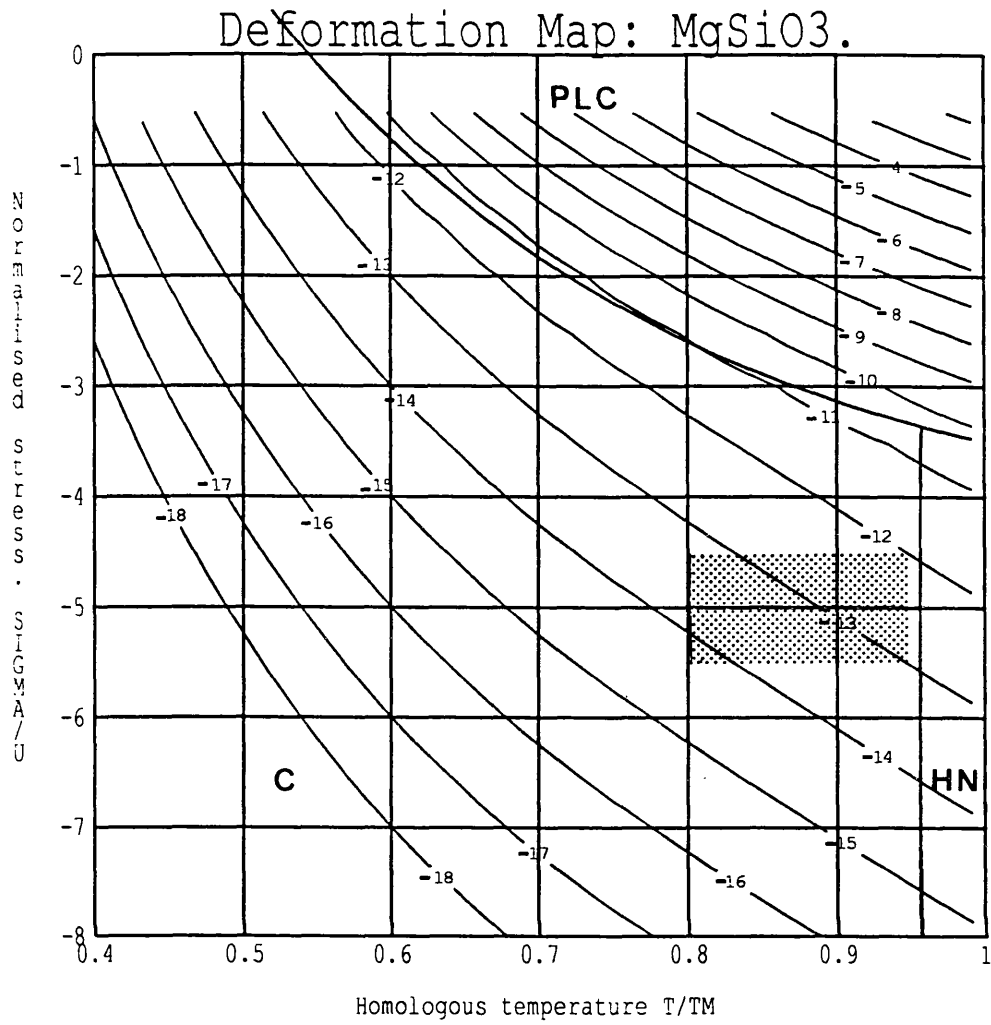


Figure 6.12 Map for MgSiO₃ at 125 GPa with Si as the rate controlling species and $d = 50 \mu\text{m}$. Contours labelled with log strain rate.

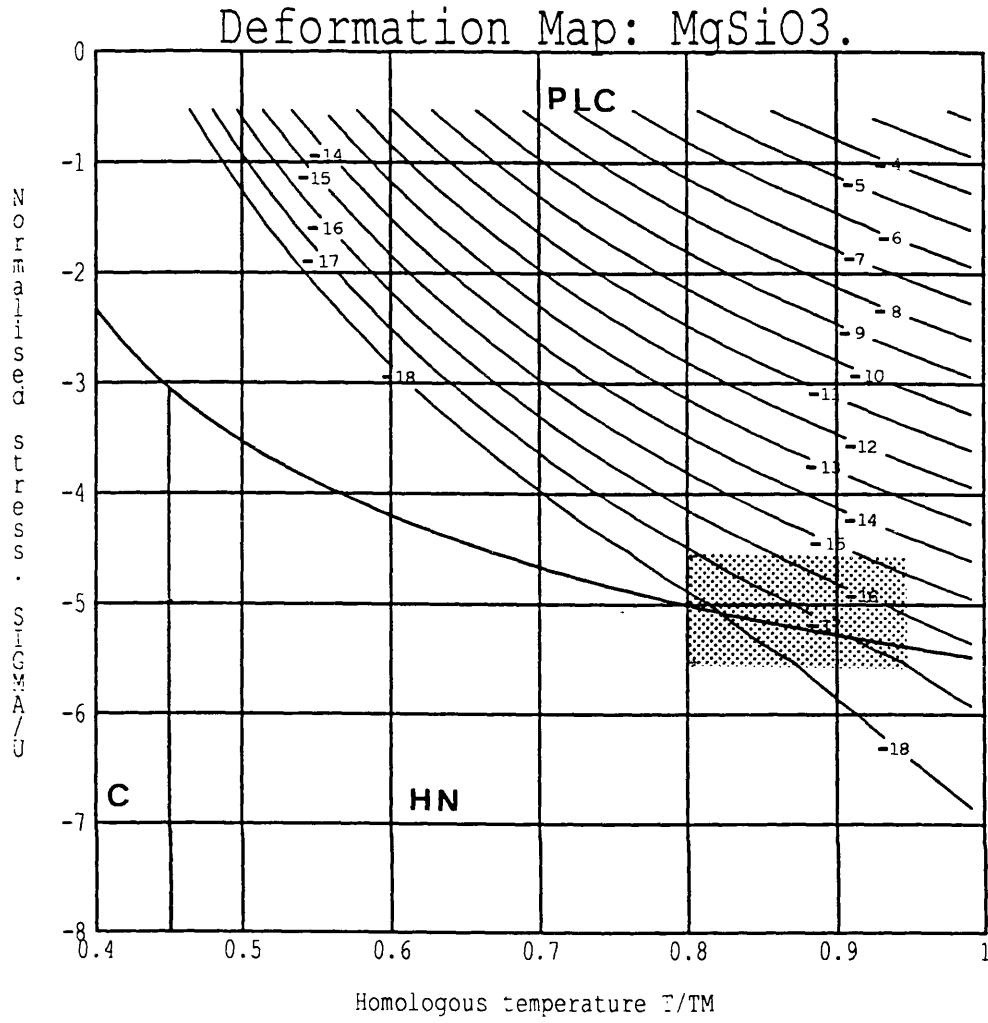


Figure 6.13 Map for MgSiO₃ at 125 GPa with Mg as the rate controlling species and $d = 1\text{mm}$. Contours labelled with log strain rate.

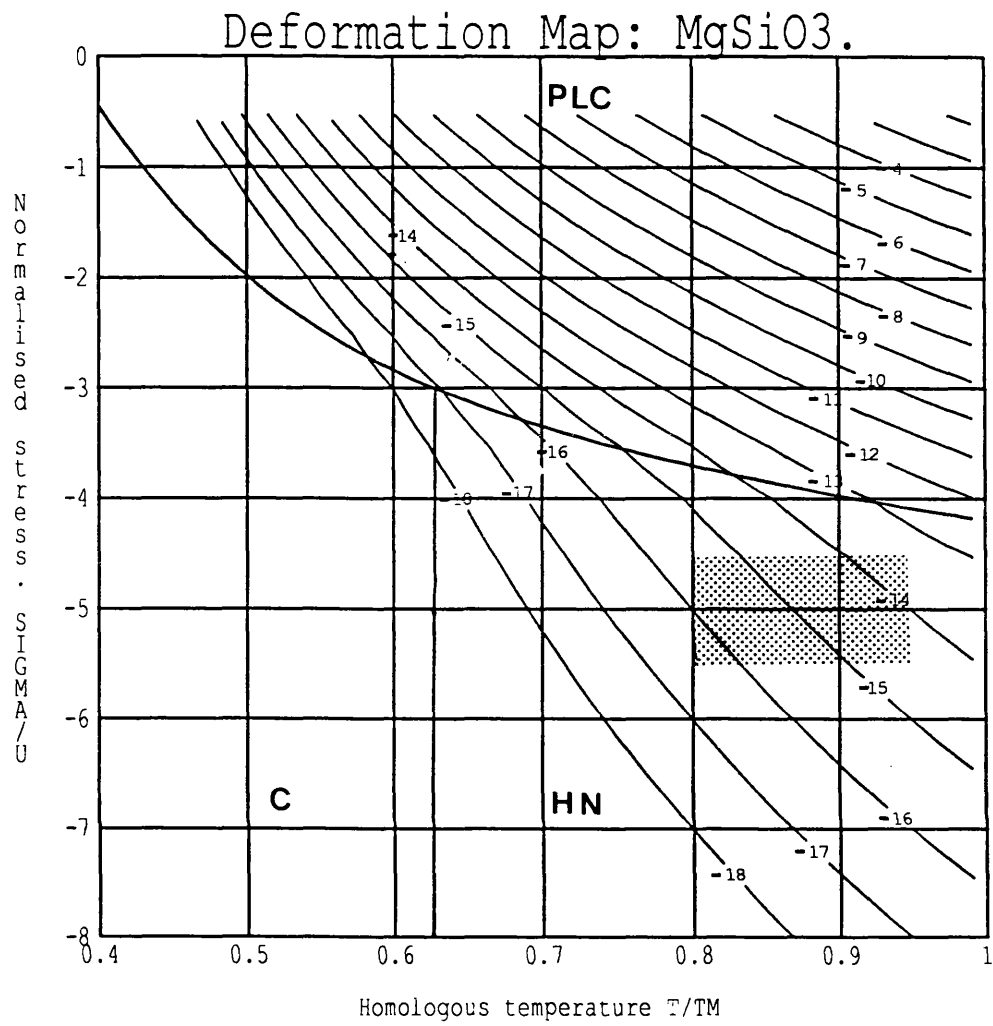


Figure 6.14 Map for MgSiO₃ at 125 GPa with Mg as the rate controlling species and $d = 50 \mu\text{m}$. Contours labelled with log strain rate.

6.8.3 Deformation maps with contours of constant viscosity

Perhaps more useful in terms of lower mantle rheology, are maps showing contours of constant viscosity. In the lower mantle, viscosity is considered to be of the order of 10^{22} Pa s to 10^{23} Pa s. (Viscosity and viscosity profiles are dealt with in Chapter 7.) Therefore a series of maps have been constructed with contours of iso-viscosity although the boundaries between different mechanisms are the same as in the previous section.

At 60 GPa, lower mantle conditions are well modelled by the maps for both Si (Figure 6.15) and Mg (Figure 6.16) diffusion. However, for Mg diffusion and a grain size of $50\ \mu\text{m}$ (Figure 6.17), lower mantle viscosities are at least two orders of magnitude lower than those obtained from geophysical data.

At 125 GPa, the situation is similar to that at 60 GPa for grain sizes above 0.1 mm although for grain sizes below this, low values of viscosity are predicted regardless of the which species is taken to be rate controlling.

6.8.4 Discussion

Combining the information from the maps with constant strain rate and constant viscosity contours allows some general statements to be made concerning possible deformation mechanisms in the lower mantle. Firstly, at 60 GPa, which from PREM (Dziewonski and Anderson 1981) relates to a depth of 1407 km, deformation is most likely to occur by power-law creep regardless of whether Si or Mg is the rate controlling species for diffusion. Only if the grain size were less than 0.1 mm could diffusional creep processes become dominant.

At 125 GPa, a depth of 2670 km, the situation is not so straightforward. If Si diffusion is rate controlling, then Herring-Nabarro creep is predicted to dominate flow, but if Mg is rate controlling, as suggested by the simulation

Key

1	10^{11}
2	10^{12}
3	10^{13}
4	10^{14}
5	10^{15}
6	10^{16}
7	10^{17}
8	10^{18}
9	10^{19}
10	10^{20}
11	10^{21}
12	10^{22}
13	10^{23}
14	10^{24}
15	10^{25}
16	10^{26}
17	10^{27}
18	10^{28}
19	10^{29}
20	10^{30}

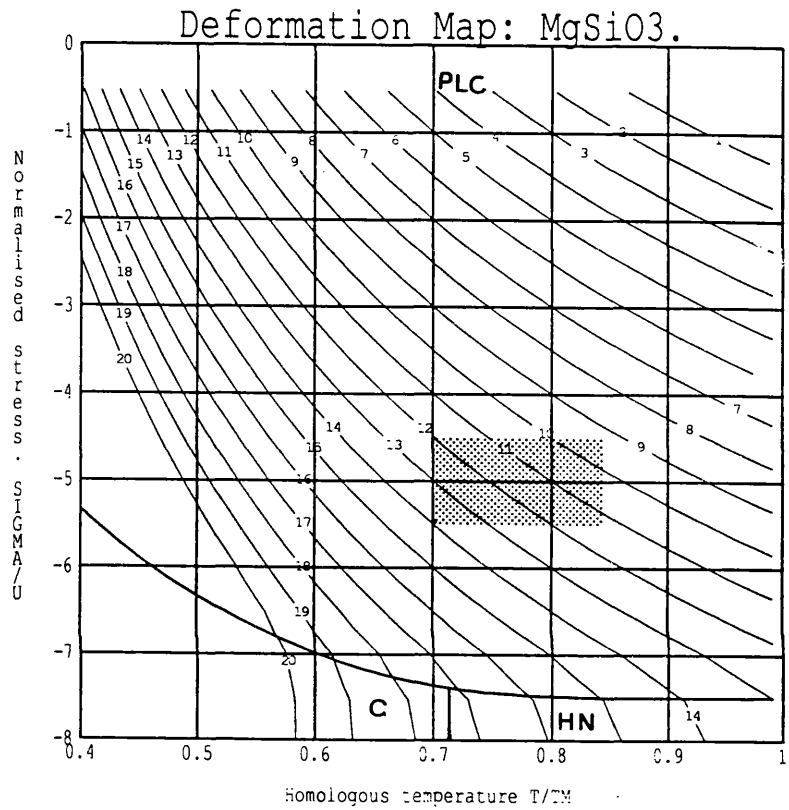


Figure 6.15 Map for MgSiO₃ at 60 GPa with Si as the rate controlling species and $d = 1.0$ mm. Values of viscosity contours are given in the key.

Key

1	10^{11}
2	10^{12}
3	10^{13}
4	10^{14}
5	10^{15}
6	10^{16}
7	10^{17}
8	10^{18}
9	10^{19}
10	10^{20}
11	10^{21}
12	10^{22}
13	10^{23}
14	10^{24}
15	10^{25}
16	10^{26}
17	10^{27}
18	10^{28}
19	10^{29}
20	10^{30}

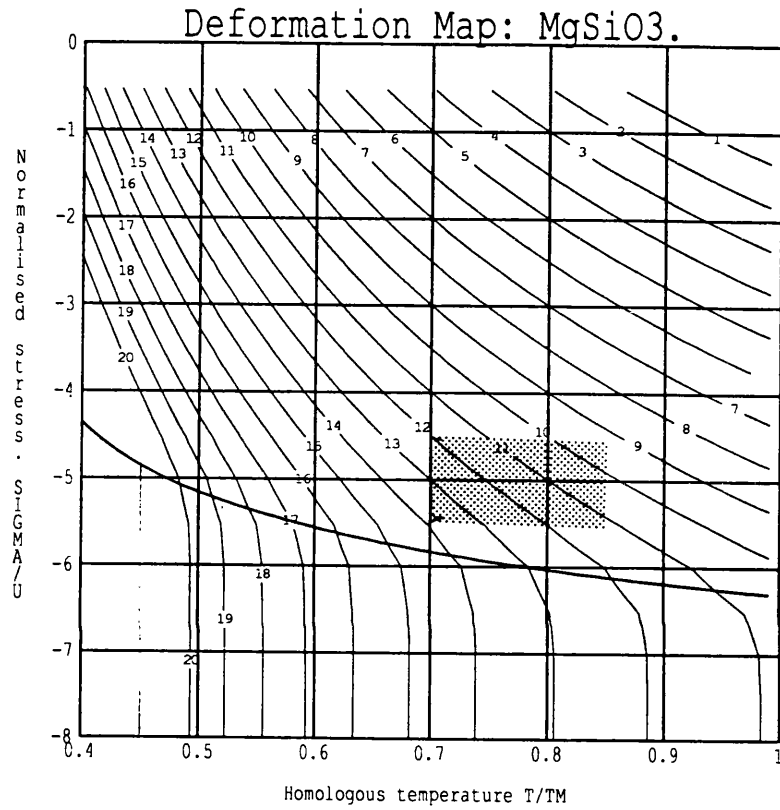


Figure 6.16 Map for MgSiO₃ at 60 GPa with Mg as the rate controlling species and $d = 1.0$ mm. Values of viscosity contours are given in the key.

Key

1	10^{11}
2	10^{12}
3	10^{13}
4	10^{14}
5	10^{15}
6	10^{16}
7	10^{17}
8	10^{18}
9	10^{19}
10	10^{20}
11	10^{21}
12	10^{22}
13	10^{23}
14	10^{24}
15	10^{25}
16	10^{26}
17	10^{27}
18	10^{28}
19	10^{29}
20	10^{30}

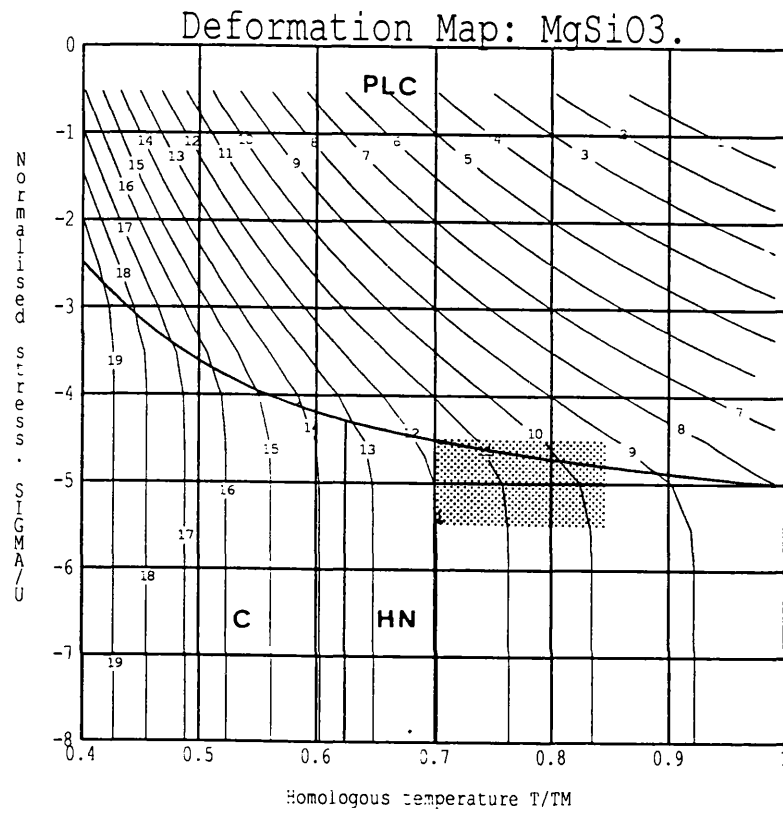


Figure 6.17 Map for MgSiO₃ at 60 GPa with Mg as the rate controlling species and $d = 50 \mu\text{m}$. Values of viscosity contours are given in the key.

results in Chapter 5, then either power-law or Herring-Nabarro could dominate.

However, to predict viscosities in line with those inferred from geophysical data, grain size must be greater than 50 μm , which agrees with previous estimates.

The preferred model is one where power-law creep controls deformation throughout the bulk of the lower mantle. Mg diffusion is likely to take over from Si as the rate controlling process at depth which increases the importance of diffusion in flow. Because of the uncertainties in estimates of stress and temperature in the lower mantle, it is impossible to distinguish from Figure 6.13 which mechanism will dominate flow, and it seems more likely that both mechanisms will contribute in a significant way to the overall deformation.

Of course it must be borne in mind that the data used in the construction of these maps may not necessarily be representative of the actual physical properties and that the assumptions made regarding similarities between CaTiO_3 and MgSiO_3 behaviour may not be valid. However, the ability of the data set to reproduce mantle conditions of strain rate, stress and viscosity does show that it is possible to investigate the rheology of perovskites using a mineral physics approach.

CHAPTER 7: THE RHEOLOGY OF THE LOWER MANTLE

7.1 Introduction

The rheological approach to modelling the lower mantle consists of trying to constrain the viscosity profile by making use of rheological equations of state (EOS). The simplest EOS (Poirier 1988) describes the viscosity, η , of a material as:

$$\eta = f(P, T, \sigma, \dot{\epsilon}, d, m, c) \quad (7.1)$$

where P is the pressure, T is temperature, σ is the effective stress, $\dot{\epsilon}$ is the strain rate, d is the grain size, m denotes the intrinsic material properties and c is the chemical environment. Viscosity is then one of the most important parameters in all rheological studies.

The biggest problem to date with using this approach, has been the lack of data on the properties and behaviour of the main lower mantle phase (Mg,Fe)SiO₃ perovskite. Previous attempts to model the viscosity profile of the lower mantle have centred on the use of gross physical and thermodynamic properties inferred from seismic data (eg. Sammis et al. 1977, Ellsworth et al. 1985, Stacey et al. 1977), numerical convection models (eg. Christensen and Yuen 1985), by extrapolating upper mantle flow laws to the lower mantle (Ranalli and Fischer 1984) or by assuming that the minor component of the lower mantle, (Mg,Fe)O magnesiowustite, controls flow (Karato 1981). The work presented here then represents the first attempt at modelling the rheology of the lower mantle by considering explicitly the properties of MgSiO₃ perovskite.

In this chapter, the geophysical evidence for lower mantle viscosity is first presented and then the previous models reviewed. A number of viscosity

profiles for the lower mantle are then presented, constructed using the rheological data set compiled in Chapter 6. The results of these profiles are then compared to those of other workers and the geophysical significance of the models discussed.

7.2 Models of mantle viscosity from geophysics

On the time scale of a few seconds, the Earth's mantle can be considered as an elastic body and thus the passage of seismic waves causes no permanent deformation. Over much longer timescales however, the mantle will behave as a fluid which can be described as a classical Maxwell body (Peltier et al. 1981), and so will deform in response to a large surface load.

Large scale loading of the Earth's surface occurred most recently during the last Pleistocene glaciation when large areas of the Canadian and Fennoscandian shields were covered by ice sheets. This glacial loading resulted in the depression of the lithosphere and consequent deformation of the underlying mantle. Melting of the ice sheets, thereby removing the load, has led to uplift of these areas as the lithosphere strives to regain isostatic equilibrium.

The displacement of the surface due to unloading, decreases exponentially with time, τ , known as the relaxation time (Turcotte and Schubert 1982) and is related to viscosity by:

$$\tau = 4\pi\eta/\rho g\lambda \quad (7.2)$$

where g is the acceleration due to gravity and λ is the characteristic wavelength of the load. Therefore, the viscosity can be estimated once the relaxation time is known. In order to find τ , the rate of uplift, the time since unloading and the remaining uplift must all be quantified. Rates of uplift have

been calculated from radio carbon dating of organic debris found on raised beaches, whilst accumulation of glacial deposits shows that de-glaciation occurred about 10^4 years ago. The remaining uplift before isostatic equilibrium is reached can be inferred from gravity data, since areas in non-isostatic equilibrium are characterised by negative free air Bouger anomalies. More complex studies which take into account the rigidity of the lithosphere and the depth dependence of viscosity along with considerable post-glacial rebound data have led to an inferred mantle viscosity of 10^{21} Pa s (eg. Cathles 1975; Peltier 1982, Wolf 1986) which changes by only a factor of only 2 or 3 across the whole mantle.

One of the problems with using post glacial rebound data, is that it only samples the response of the mantle to deformation over a relatively short timescale and may therefore represent a transient response (Weertman 1978), which is superimposed on the steady state convective motion, which could mask the true long term behaviour. Other techniques, such as variations in the geoid and long term polar wander, sample much longer timescales and so provide additional constraints on the dynamic state of the mantle.

Long wavelength variations in the Earth's geoid can be directly related to the density variations resulting from convection. Using techniques of seismic tomography (see Woodhouse and Dziewonski 1989), differences in density which provide the driving force for convective motion, can be mapped with increasingly higher resolution. Analysis of the geoid together with seismic tomography, places constraints on the variation of viscosity with depth although it is unable to give absolute values. The models of Hager and Richards (1989) show a significant increase in viscosity across the upper/lower mantle boundary and lead to a lower mantle viscosity of at least 3×10^{22} Pa s, more than a factor of 10 higher than that inferred from post-glacial rebound.

The phenomena of true polar wander, changes in the position of the Earth's magnetic poles with time, can also be related to mantle convection.

The analyses of true polar wander rates by Sabadini and Yuen (1989) also supports the case for a more viscous lower mantle. The above authors invoke a chemical change at the transition zone coupled with a lower mantle viscosity of 10^{22} to 10^{23} Pa s to fit to the observed polar wander rates.

This apparent contradiction in lower mantle viscosity between rebound and geoid and polar wandering data can be resolved by using models to include the effects of transient rheology. Peltier (1985), used a Burgers body model to analyze rebound data, which is able to include both steady state and transient components of the viscosity. Peltier found that by using this model, a lower mantle with a viscosity of 10^{22} to 10^{23} Pa s was indeed compatible with glacial rebound data.

All of the above models however, assume a Newtonian mantle which conflicts with microphysical models of rock deformation, especially for the upper mantle (Stocker and Ashby 1973), which is likely to flow according to a power-law. Turcotte and Schubert (1982) consider that the geophysical evidence can be attributed to either Newtonian or non-Newtonian rheology and that the absolute value of viscosity will only differ by a factor of 3 between the two. These authors consider that the temperature and depth dependence of viscosity will be far more important.

7.3 Previous models of mantle viscosity

The following is a short review of previous attempts to model the viscosity of the lower mantle using mineralogic and thermodynamic constraints. Various other methods have been used as indicated in section 7.1, however, as this is not intended to be a comprehensive review, these will not be covered.

Ellsworth et al. (1985) modelled the viscosity of the lower mantle using models of Gibbs free energy of activation, G , and an assumed adiabatic temperature gradient. These authors used an initial value of G of 390 kJmol^{-1} , close to the experimental values for O diffusion and dislocation recovery in olivine. This value was then extrapolated to lower mantle conditions using both an elastic strain energy model where G is related to seismic properties, and by using the empirical relationship between G and the melting temperature described in section 2.6. Ellsworth et al. considered both Newtonian and non-Newtonian flow laws and with conditions of constant stress, constant strain rate and constant strain energy dissipation. The results predicted a non-Newtonian rheology with an increase in viscosity of 2 - 3 orders of magnitude with depth for constant stress, depending on which model value of G was used. The variation of viscosity with depth was progressively reduced for constant strain rate and constant dissipation respectively.

Both methods of estimating G , however, have their limitations. Using the strain energy model, Ellsworth et al. (1985) found that the activation volume for olivine was systematically underestimated. Using the second method, the melting temperature is assumed to follow Lindemann's theory of melting which may not be appropriate for silicates at very high pressures (Wolf and Jeanloz 1984, Stacey et al. 1989).

Ranalli and Fischer (1984) attempted to model mantle viscosity assuming that the creep laws for an olivine upper mantle could be carried over to the lower mantle. Both the constant stress and constant strain rate situations were considered. The results obtained were similar to those of Ellsworth et al. (1985), with a predicted lower mantle viscosity of 10^{22} Pa s rising to as much as 10^{25} Pa s when stress was constant, but with constant strain rate these values were reduced to 10^{21} to 10^{22} Pa s .

The viscosity profiles of Karato (1981) were constructed assuming that (Mg,Fe)O magnesiowustite, the minor component of the lower mantle, would

control flow. The basis of the argument was that the elastic constants of MgSiO_3 are much stiffer than those of MgO and hence MgO should control flow unless frame work effects are important. Poirier (1988) has pointed out that no clear relationship exists between elastic constants and deformation behaviour. The fact that only 30% $(\text{Mg,Fe})\text{O}$, at the very most, is present in the lower mantle suggests that frame work effects will be important. However, this attempt may be somewhat more realistic than those based on the assumption that the lower mantle behaves rheologically like olivine. Karato took diffusion of O to be the rate controlling process and considered the case for both constant stress and constant strain rate. The variation of viscosity across the lower mantle was found to vary depending on the activation volume, temperature and whether stress or strain rate was constant. Karato's main conclusion, like that of Ellsworth et al. and Ranalli and Fischer, was that flow in the lower mantle would be non-Newtonian in behaviour.

7.4 Lower mantle viscosity profiles: Methodology

The values of viscosity across the lower mantle can be calculated using a model of channel flow where the system is bounded by upper and lower thermal boundary layers, in this case taken to be the lithosphere and D'' respectively. Between the boundary layers, temperature is assumed to follow an adiabatic gradient. The viscosity for such a 2 dimensional system can be expressed in terms of stress and strain rate by:

$$\eta = \sigma/2\dot{\epsilon} \quad (7.3)$$

where η is the effective viscosity. The strain rate term can be expanded so that viscosity can be calculated from the theoretical constitutive equations (Chapter 2) for both Newtonian and non-Newtonian behaviour.

In the case of linear Newtonian rheology, flow may be controlled by

either Herring-Nabarro or Coble creep (Section 2.2). Rearranging and expanding the rate equations for each gives:

$$\eta = [RTd^2/2\beta\Omega D_0] \exp(E+PV^*/RT) \quad (7.4)$$

for Herring-Nabarro creep where D_0 is the pre-exponential diffusion coefficient for bulk diffusion and the exponential term expresses the pressure dependence. For Coble creep:

$$\eta = [RTd^3/2\beta\Omega\delta D_0] \exp(E+PV^*/RT) \quad (7.5)$$

where D_0 is the pre-exponential diffusion coefficient for grain boundary diffusion.

For non-Newtonian behaviour, the rate equation for power-law creep (Equation 2.9 Section 2.3.2.1) is rearranged to give:

$$\eta = [RT\mu^2 b^2/2A\Omega D_0](1/\sigma^{n-1}) \exp(E+PV^*/RT) \quad (7.5)$$

where D_0 is the pre-exponential coefficient for dislocation climb. The effects of pressure and temperature on these equations can be calculated by using the equations of state given in section 6.4.

The effective viscosity is then calculated for each mechanism in turn assuming a constant value of stress. The mechanism with the lowest value then gives the value of viscosity as a function of depth.

7.5 Models of lower mantle viscosity

A number of viscosity profiles have been constructed for the lower mantle using the rheological data set for $MgSiO_3$ perovskite presented in the previous chapter. The effects of temperature on the viscosity profiles has been

considered by using the geotherms of both Stacey (1977) and Brown and Shankland (1981) as upper and lower limits on lower mantle temperatures respectively. Similarly, the effects of the diffusion activation parameters are considered by using the calculated values of activation enthalpy and activation volume for both Si and Mg diffusion.

7.5.1 The effects of temperature and stress

Viscosity is exponentially dependent on temperature through the diffusion coefficient and therefore the geotherm chosen will have a considerable effect on the calculated value of viscosity and its variation with depth. Figure 7.1 shows the profiles produced using the geotherms of Stacey (Figure 7.1a) and Brown and Shankland (Figure 7.1b). Both were computed for a grain size of 1mm and constant stress of 1 MPa. The diffusion activation enthalpy and activation volume are those calculated for Si diffusion. Both geotherms predict that the rheology of the bulk of the lower mantle will be non-Newtonian.

Using the Stacey geotherm (Figure 7.1a), viscosity increases from 5.8×10^{19} Pa s at 670 km to a maximum of 4.0×10^{20} Pa s at 2675 km depth and then falls slightly in the bottom 300 km of the lower mantle. These values are lower by a factor of 15 than those expected from geophysical data. With the Brown and Shankland geotherm, viscosity rises smoothly from 1.4×10^{22} Pa s at 670 km to 1.3×10^{23} a depth of 2570 km where Coble creep takes over as the lowest viscosity mechanism. This change from non-Newtonian to Newtonian behaviour is accompanied by a drop in viscosity of a factor of 8. Setting the stress to an upper estimate of 10 MPa, flow is non-Newtonian for both geotherms throughout, but the values of viscosity drop by a factor of 20, making both unacceptable.

On the basis of temperature and stress at a grain size of 1.0 mm, the lower mantle viscosity profile is best modelled, within the constraints imposed

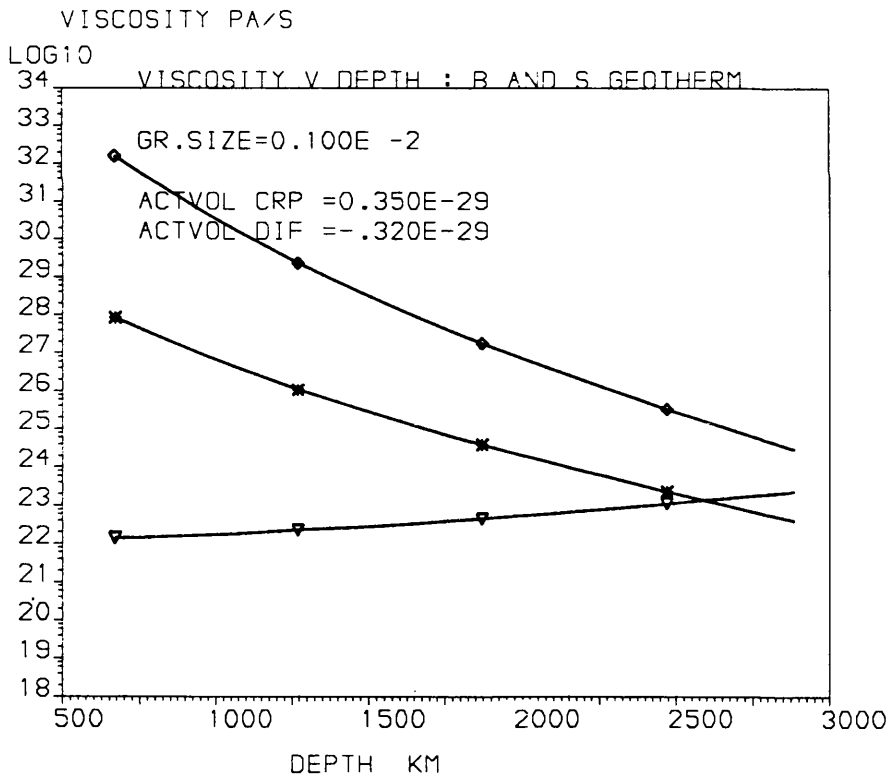
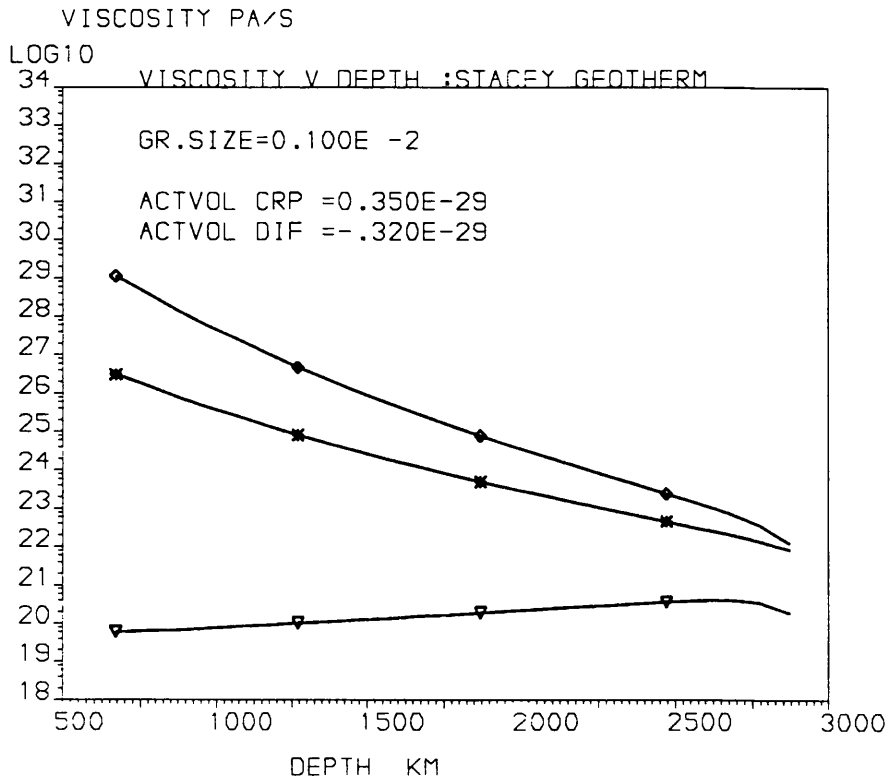


Figure 7.1 Viscosity profiles of the lower mantle using the geotherms of (a) Stacey (1977) and (b) Brown and Shankland (1981).

▽ Power-law creep * Coble creep ◇ Herring-Nabarro creep

by geophysical data, by the Brown and Shankland geotherm using a value of 1 MPa for applied stress. Both geotherms predict a drop in viscosity over the lowermost part of the lower mantle.

7.5.2 The effects of grain size

In section 6.8 it was proposed that grain size in the lower mantle was likely to lie between 1.0 and 0.1 mm. Figure 7.2 shows the effects of reducing the grain size on the viscosity profiles using the Brown and Shankland geotherm and the same activation parameters as in Figure 7.1a. For a grain size of 0.1 mm the rheology is controlled by power-law creep only to a depth of 1470 km, when Coble creep is dominant and flow is Newtonian. This leads to a sharp drop in viscosity due to the negative activation volume for Si diffusion.

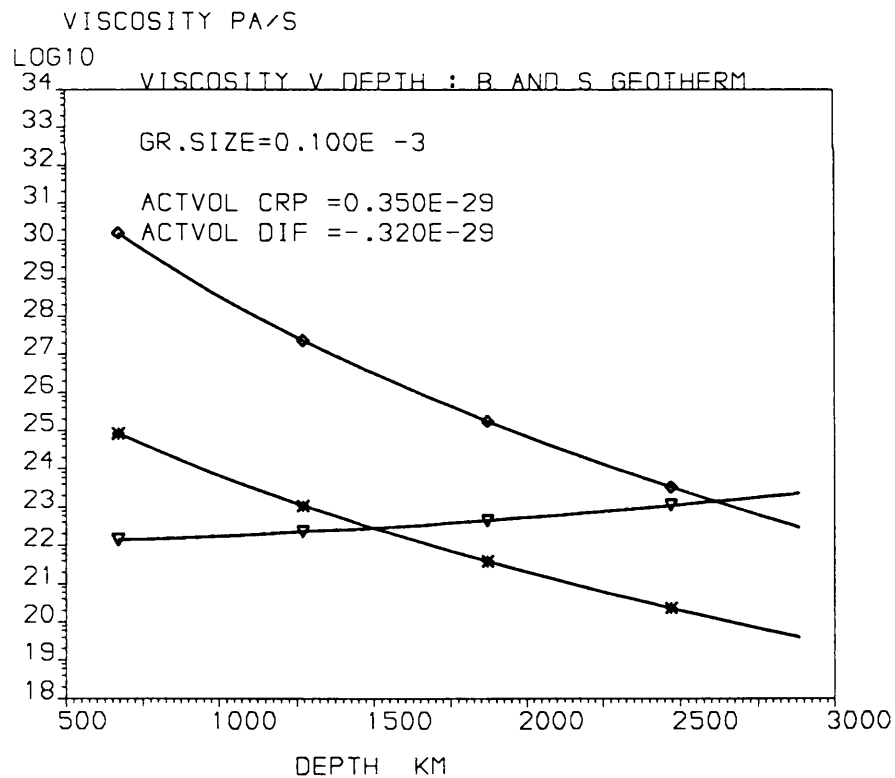


Figure 7.2 Viscosity profile for grain size of 0.1mm

The situation when using the Stacey geotherm is similar, although the crossover between non-Newtonian and Newtonian rheology does not occur until a depth of 2100 km. Both geotherms, however, give unrealistic values of viscosity. The predominant effect of reducing grain size, is then to reduce the values of viscosity predicted for diffusional creep mechanisms.

7.5.3 Changing the activation parameter

In section 5.8, the activation volume for Si diffusion was calculated to be $-2.2 \text{ cm}^3 \text{ mol}^{-1}$ ($-3.2 \times 10^{-30} \text{ m}^3$), if this figure is reduced to $-1.3 \text{ cm}^3 \text{ mol}^{-1}$, ($-2.2 \times 10^{-30} \text{ m}^3$) then the slope of the diffusional creep profiles is considerably reduced. The rheology of the lower mantle using the Brown and Shankland geotherm (Figure 7.3a) is now non-Newtonian throughout for the larger grain size, with viscosity increasing smoothly with depth giving a good fit to geophysical data. Reducing the grain size to 0.1 mm however (Figure 7.3b) again shows a change to Coble creep and a corresponding low viscosity in the bottom half of the lower mantle.

Increasing the value of V_{plc}^* , leads to an increase in viscosity with depth for the power-law profile. Combining this with the reduced activation volume for diffusion gives the profile shown in figure 7.4 . For a grain size of 1.0 mm, the Stacey geotherm now gives the best fit to geophysical data although over the last 450 km of the lower mantle, the viscosity is once again controlled by Coble creep and drops by a factor of 5. The corresponding profiles using the Brown and Shankland geotherm are now completely at variance with geophysical data.

If Mg rather than Si is the rate controlling species for diffusion in MgSiO_3 perovskite at depth, then the activation volume for diffusion will be positive and the activation enthalpy lower. The calculated value of activation volume for Mg diffusion in this case is similar to the initial value chosen for V_{plc}^* . Using these values and the Stacey geotherm, rheology is predicted to be

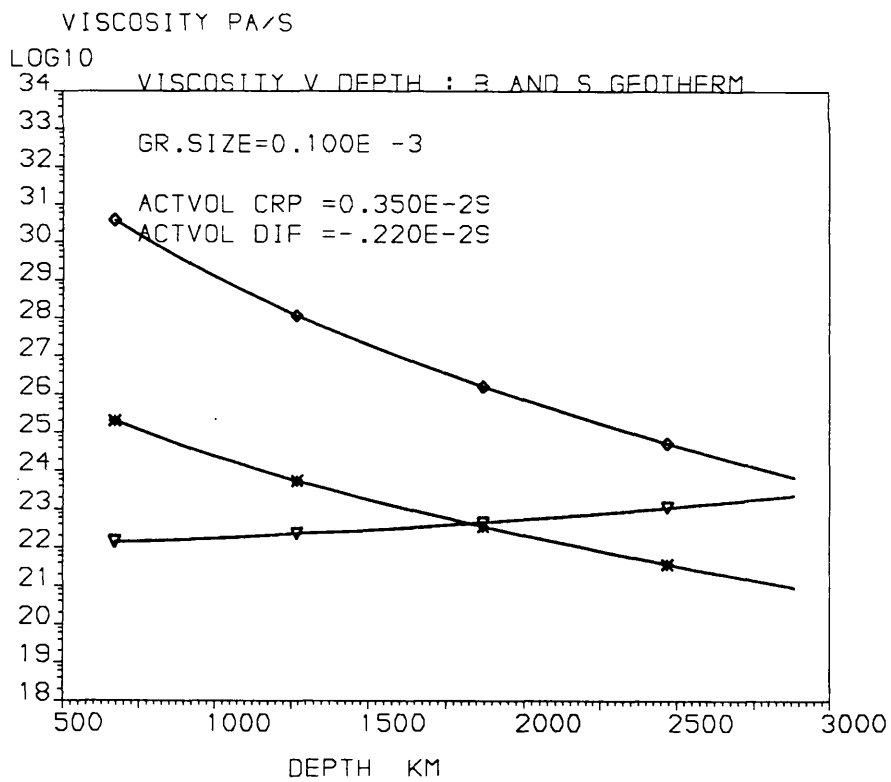
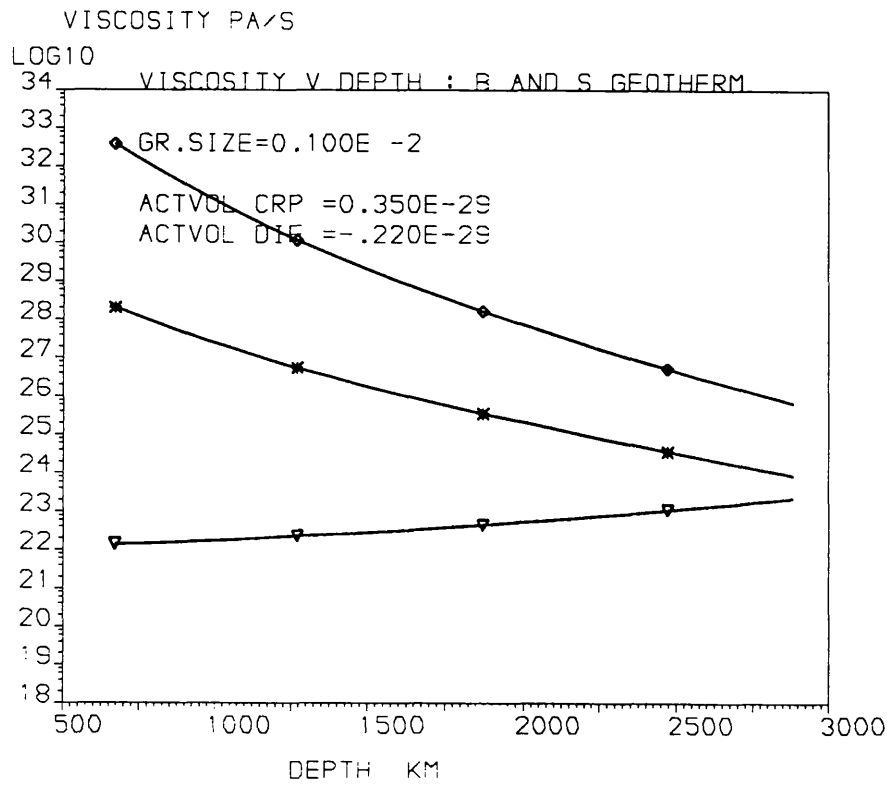


Figure 7.3 The effects of changing V^* on the viscosity profiles for grain size of (a) 1.0 mm and (b) 0.1 mm

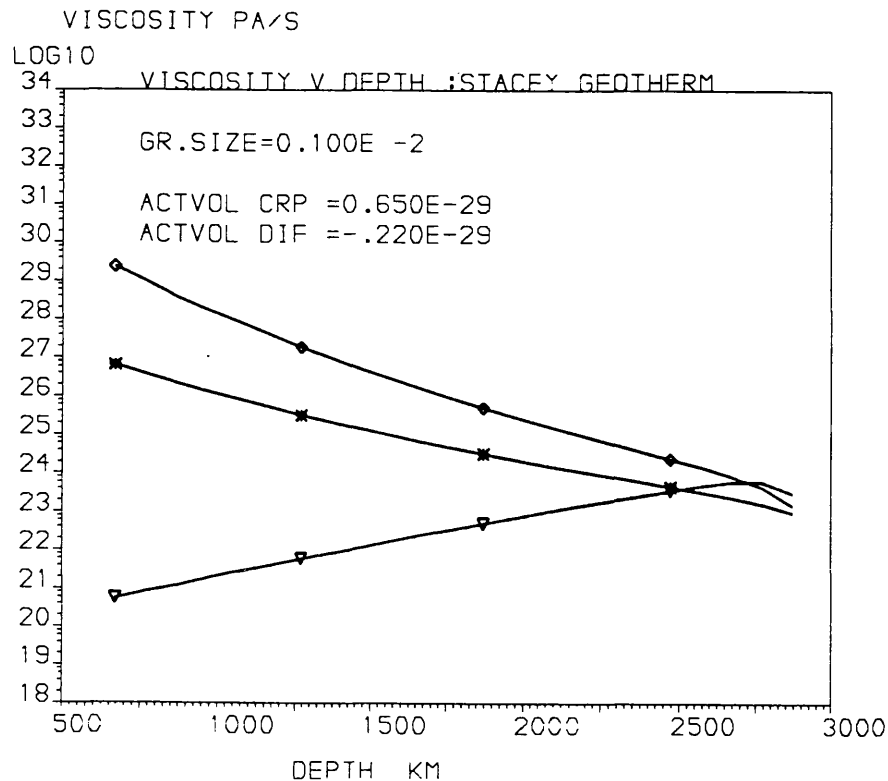


Figure 7.4 Viscosity profile using the geotherm of Stacey and grain size of 1.0 mm

non-Newtonian throughout the lower mantle for all grain sizes ranging from 1.0 mm to 50 μm with the rather low values of viscosity as in Figure 7.1a. Diffusional creep mechanisms only control rheology when the activation volume for power-law creep is large and grain size less than 1.0 mm (Figure 7.5). It is then Herring-Nabarro rather than Coble creep which gives the lowest viscosity.

Using the Brown and Shankland geotherm, rheology is also non-Newtonian for all grain sizes when $V_{\text{Dif}}^* = V_{\text{plc}}^*$ with the values of viscosity as in Figure 7.1b. With a larger value of power-law creep activation volume, Coble creep is responsible for the viscosity throughout the bulk of the lower mantle as shown in Figure 7.6, although the values of viscosity are now at the upper limit of those considered as acceptable.

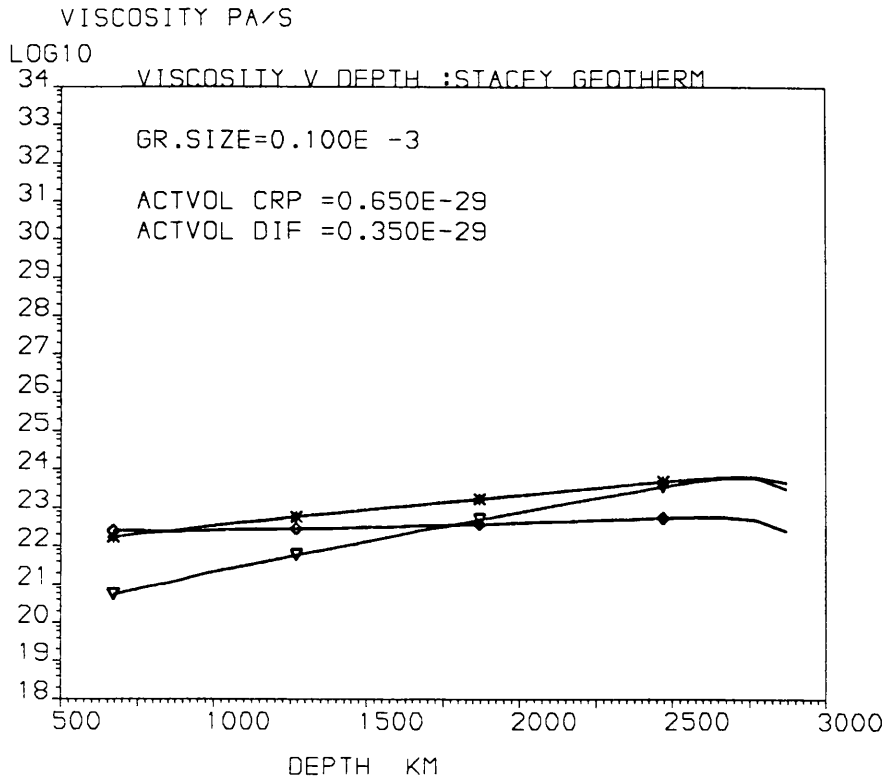


Figure 7.5 Viscosity profile using a large value of V_{plc}^* and the Stacey geotherm

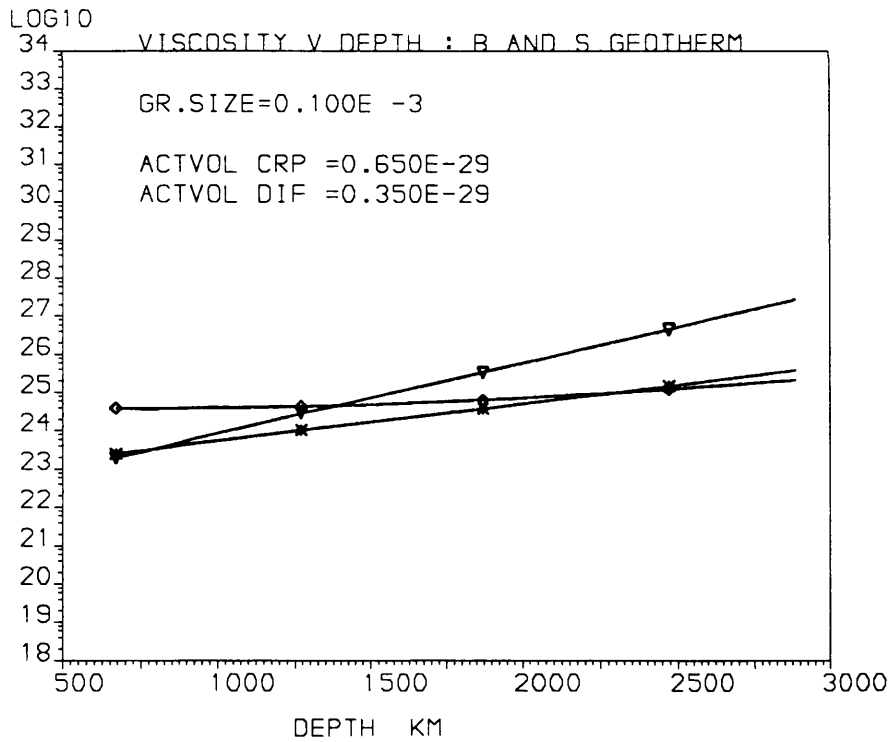


Figure 7.6 Viscosity profile using a large value of V_{plc}^* and the geotherm of Brown and Shankland

7.5.4 Discussion

From examination of figures 7.1 to 7.6, it can be seen that temperature and activation volume are the most important in determining the values of viscosity with depth. These parameters, along with grain size, will control whether the rheology of the lower mantle is Newtonian or non-Newtonian in its behaviour.

In general, the Brown and Shankland geotherm was found to be more able to reproduce viscosities in line with those inferred from geophysical data. For the higher geotherm of Stacey, profiles are only acceptable when the larger values of activation volume are used. Rheology, using this geotherm, is predicted to be non-Newtonian unless grain size is less than 0.1mm. For the Brown and Shankland geotherm, acceptable profiles are produced using the smaller values of V^* and predict predominately non-Newtonian behaviour. Newtonian rheology is only predicted to occur when V_{plc}^* is large.

Yuen and Zhang (1987) have concluded that an activation volume of not more than $2 \text{ cm}^3 \text{ mol}^{-1}$ is required to maintain the core - mantle topography inferred from seismic data. On this basis then, the larger activation volume of $3.9 \text{ cm}^3 \text{ mol}^{-1}$ ($6.5 \times 10^{-30} \text{ m}^3$) required to give the best fit profiles using the Stacey geotherm are untenable. The profiles produced using the smaller activation volume and Brown and Shankland geotherm are therefore considered to be more realistic.

On the basis of the above, the rheology of the lower mantle is predicted to be non-Newtonian, with a variation of a factor of 10 with depth. Conclusions as to the grain size of the lower mantle are in line with those inferred from the deformation mechanism maps in Chapter 6, ie. between 1mm and 0.1 mm. The preferred geotherm is that of Brown and Shankland, although an alternative geotherm, somewhere between the two extremes considered here could also be acceptable. The question as to whether Si or Mg mobility is rate

controlling in the diffusional creep of MgSiO_3 will be important only if grain size is smaller than 1.0 mm.

The profiles presented here, differ from those of previous studies in that the variation of viscosity with depth for constant stress is quite small in comparison. This seems primarily due to the small activation volumes used. The values of V^* for diffusion calculated in Chapter 5, depend only on the ability of the potential to simulate the EOS accurately and as a consequence are no better or no worse than those calculated using the various assumptions employed in the strain energy and melting temperature models. The value of the activation volume for power-law creep, $1/5^{\text{th}}$ of the molecular volume, is not an unreasonable one and its use seems to be justified by the results obtained.

7.6 Rheology and convection

The viscosity of the lower mantle depends on the exponential of the inverse absolute temperature and on pressure. Therefore the temperature and viscosity structure of the mantle are intimately related and in a sense constitute a self regulating system. Any increase in temperature will result in a corresponding decrease in viscosity giving more efficient removal of heat by enhanced convection. Therefore some equilibrium state should be theoretically possible and accurate knowledge of one should impose quite tight constraints on the other. Unfortunately, neither viscosity or temperature are well enough known.

If a double convective system exists and a thermal boundary layer is present at the upper/lower mantle boundary, then the temperature in the lower mantle will be significantly higher and the viscosity lower than in the case of whole mantle convection. Across the boundary itself, viscosity would be expected to decrease dramatically, unless the material properties of such a

layer were considerably different from those above and below.

Recent reports from Karato (1989) and Meade and Jeanloz (1990), have suggested that the transition zone materials, mainly $(\text{Mg,Fe})_2\text{SiO}_4$ spinel and garnet, could be significantly stronger than either olivine or silicate perovskite. Wu and Yuen (1991) have modelled the effects on viscosity of such a three layer mantle in relation to post glacial rebound data. These authors conclude that the presence of such a strong layer in the transition zone requires a lower viscosity in the lower mantle to comply with geophysical data.

If the mantle convects as a single body, then viscosity can be expected to increase smoothly with depth from around 10^{20} Pa s in the asthenosphere to 10^{22} to 10^{23} Pa s at depth in the lower mantle. Such a model is consistent with geophysical evidence and with the viscosity profiles presented here, providing that the geotherm is closer to the lower of the two used.

However, if layered convection occurs, then the mantle could be essentially isoviscous throughout. The viscosity increase expected across the associated thermal boundary layer could well be absorbed by a high strength layer as proposed by Karato (1989) and Meade and Jeanloz (1990). The higher temperatures in the lower mantle invoked by the thermal boundary layer are likely to be closer to the geotherm of Stacey (1977). The corresponding viscosity profiles in section 7.5 still show an increase in viscosity of a factor of 10 with depth for constant stress and unrealistically low values at 700 km depth (5.8×10^{19} Pa s). The only way to reconcile a viscosity profile using the proposed rheological properties of silicate perovskite with a double convective system, is to have an activation volume greater than $3 \text{ cm}^3 \text{ mol}^{-1}$ and constant strain energy dissipation.

The preferred model then, is one in which the mantle convects as a single system by a power-law rheology with viscosity increasing by a factor of 10 to 15 across the lower mantle. However, on the basis of the models

presented here, the presence of a double convective system cannot be ruled out.

7.7 Conclusions

The work in this thesis has used a powerful combination of experiments on analogues and computer simulation techniques to investigate the rheology of materials with the perovskite structure with a view to constrain more tightly the rheology of the Earth's lower mantle.

The experimental results, along with those of Beauchesne and Poirier (1989, 1990) have shown that perovskites are a mechanically diverse group of materials which do not show any obvious isomechanical behaviour. Of all the perovskites so far studied, CaTiO_3 seems to represent the best analogue for MgSiO_3 perovskite. However, a more detailed study on the deformation microstructures in CaTiO_3 and NaNbO_3 is needed to further quantify their creep laws. Further experiments on other perovskites would be most useful. In particular, the physical basis for the Harper-Dorn creep mechanism, displayed by KTaO_3 (Beauchesne and Poirier 1990) and KZnF_3 (Poirier et al. 1983) should be rigorously investigated along with the phenomena of enhanced ionic conductivity.

The computer simulation techniques used in Chapter 5 have enabled the calculation of diffusion activation enthalpies for various ionic species in three perovskite. The close agreement between calculated and experimental activation enthalpies for O diffusion in SrTiO_3 show that this particular method is indeed justified for perovskite materials. The results of simulations of MgSiO_3 at high pressures have yielded activation volumes for both Si and Mg diffusion. At depth in the Earth's lower mantle, Mg mobility is predicted to be the rate controlling process. Furthermore, it has been shown that extrinsic defect processes, due to reactions with co-existing $(\text{Mg,Fe})\text{O}$ magnesiowustite,

are likely to dominate over intrinsic processes.

Two points must be stressed when considering the results of these calculations. Firstly, only the static lattice has been considered, so that no account has been taken of the contribution of entropy to the activation parameters. At the high temperatures of the lower mantle, the effects of entropy could be significant and therefore needs further investigation. Secondly, these results are only as good as the interatomic potentials used. The potential parameters were able to simulate the structural and elastic properties of SrTiO_3 and CaTiO_3 extremely well although for MgSiO_3 the elastic constants predicted are out by some 40%. The development of potentials which can accurately simulate the structure, elasticity and thermodynamics of MgSiO_3 will lead to great improvements in our understanding of this geologically important mineral.

Using the experimental data and results from the simulations, rheological data sets for CaTiO_3 and MgSiO_3 have been compiled and used in the construction of deformation mechanism maps. The maps for CaTiO_3 are in excellent agreement with the experimental results and indicate that power-law creep will be the dominant deformation mechanism at 0 GPa for all but the smallest grain sizes. In the case of MgSiO_3 , calculated values of strain rate and viscosity at mantle P, T and σ conditions are in good agreement with those given by geophysical data. The maps are unable to predict unambiguously the dominant deformation mechanism in the deep mantle, since this is highly dependent on both temperature and grain size, both of which are poorly constrained. However, these results support the validity of the mineral physics approach.

The viscosity of the lower mantle has been calculated as a function of depth for a range of grain sizes and activation volumes for two different geotherms. The resulting profiles are able to reproduce values of viscosity which are in close agreement with those inferred from post glacial rebound,

polar wandering and consideration of the geoid. The results of this study indicate that the rheology of the lower mantle will be controlled by a power-law mechanism and are consistent with, although not required by, a model of whole mantle convection.

The techniques of seismic tomography are increasingly being used to image the fine structure of the Earth's deep interior. In particular the lateral variations in density, which have not been considered here, can be mapped with ever greater resolution. The improvement of these methods, together with high pressure experiments and improved potentials with which to model mantle minerals, can all be used to constrain more tightly the nature of the geotherm at depth. Once this is known, the rheological behaviour of the lower mantle can be modelled with far greater certainty.

BIBLIOGRAPHY

Akaogi, M., Ross, N., MacMillan, Navrotsky, A. (1984) The Mg_2SiO_4 polymorphs: Thermodynamic properties from oxide melt solution calorimetry, phase relations and models of lattice vibrations. *Amer. Mineral.* **69**:499

Anderson, D.L. and Bass, J.D. (1986) Transition region of the Earth's upper mantle. *Nature*, **320**:321-328.

Ashby, M.F. and Verral, R.A. (1978) Micromechanisms of flow and fracture and their relevance to the rheology of the upper mantle. *Phil. Trans. R. Soc. London.* **228**:59-95

Beauchesne, S. (1989) *Fluage a haut temperature et observations en microscopie electronique en transmission de composés de structure perovskite. Contribution a l'étude de la viscosité du manteau inférieur.* Ph. D thesis l'Université Paris 7.

Beauchesne, S. and Poirier J.P. (1989) Creep of barium titanate perovskite: A contribution to a systematic approach to the viscosity of the lower mantle. *Phys. Earth Planet. Ints.* **55**:187-189

Beauchesne, S. and Poirier, J.P. (1990) In search of a systematic for the viscosity of perovskites: The creep of potassium tantalate and niobate. *Phys. Earth Planet Ints.* **61**:182-198

Busse, F.H. (1989) Fundamentals of thermal convection. In *Mantle Convection: Plate Tectonics and Global Dynamics*. Ed. W.R. Peltier. Gordon and Breach. 22-96

Brown, J.M. and Shankland, T.J. (1981) Thermodynamic parameters in the

Earth as determined from seismic profiles. *Geophys. J. R. Astr. Soc.* **51**:579-96.

Brown, G.C. and Mussett, A.E. (1978) *The Inaccessible Earth*. George, Allen and Unwin.

Buckowinski, M.S.T. (1976) The effect of pressure on the physics and chemistry of potassium. *Geophys. Res. Letters.* **3**:491-494

Catlow, C.R.A. (1977) Point defects and electronic properties of Uranium dioxide. *Proc. R. Soc. London.* **A353**:533-561

Catlow, C.R.A. (1986) Computer simulation of defects in solids. In *Defects in Solids, Modern Techniques*. Eds A.V. Chadwick and M. Terenzi. New York: Plenum 269-302

Catlow, C.R.A. and Norgett, M.J. (1978) *AERE Harwell Report M2763*

Catlow, C.R.A., Dixon, M. and Mackrodt, W.C. (1982) Interatomic potentials in solids. In *Computer Simulation in Solids. Lecture Notes in Physics 166*. Eds. C.R.A. Catlow and W.C. Mackrodt. Berlin: Springer

Catlow, C.R.A and Mackrodt, W.C. (1982) Theory of simulation methods for lattice and defect energy calculations in crystals. In *Computer Simulation in Solids. Lecture Notes in Physics 166*. Eds. C.R.A. Catlow and W.C. Mackrodt. Berlin: Springer

Cathles, L.M. (1975) *The Viscosity of the Earth's Mantle*. Princeton University Press.

Christensen, U. (1989) Mantle rheology, constitution and convection. In *Mantle Convection: Plate Tectonics and Global Dynamics*. Ed. W.R. Peltier. Gordon and Breach. 569-656

Christensen, U. and Yuen, D. (1985) Layered convection induced by phase transitions. *J. Geophys. Res.* **90**:10291-10300

Cohen, R.E., Boyer, L., Menl, M., Pickett, W. and Krakaur, H. (1989) Electronic structure and total energy calculations for oxide perovskites and superconductors. In *Perovskite: A Structure of Great Interest to Geophysics and Materials Science. Geophysics Monograph 45*. Eds. A. Navrotsky and D.J. Weidner. Amer. Geophys. Union. Washington 1989.

Crager, K.C. and Jordan, T.H (1984) Slab penetration into the lower mantle. *J. Geophys. Resaerch* **89**:3031-3049

Doukhan, N. and Doukhan, J.C. (1986) Dislocations in perovskites BaTiO₃ and CaTiO₃. *Phys. Chem. Mins.* **13**:403-410

Dziewonski, A. and Anderson, D.L. (1981) Preliminary reference Earth model. *Phys. Earth Plan. Ints.* **25**:297-356

Edwards, A.R. (1988) *Diffusion and defects in silicate garnets*. M.Sc. Thesis University of Manchester

Ellsworth, K. Schubert, G. and Sammis, C.G. (1985) Viscosity profile of the lower mantle. *Geophys. J. R. Astr. Soc.* **83**:199-213

Frost, H.J. and Ashby, M.F. (1982) *Deformation Mechanism Maps* Oxford: Pergamon Press

Freer, R. (1980) Self-diffusion and impurity diffusion in oxides. *J. Mater. Sci.* **15**:803-824

Ganapthy, R. and Anders, E. (1974) Bulk composition of the moon and Earth estimated from meteorites. *Proc. 5th Lunar Science Conference.* 1181 - 1206

Guyot, F., Madon, M., Peyronneau, J. and Poirier, J.P. X-ray microanalysis of high PT phases synthesized from natural olivine in diamond anvil cell. *Earth Planet. Sci. Letts.* **2**

Hager, B.A. and Richards, M.A. (1989) Long wavelength variations in the Earth's geoid: Physical models and dynamical implications. *Phil. Trans. R. Soc London.* **A328**:309-327

Harper, J. and Dorn, J.E. (1957) Viscous creep of aluminum near its melting temperature. *Acta Metall.* **5**:654-665

Heinz, D.L. and Jeanloz, R. (1987) Measurement of the melting curve of $\text{Mg}_{0.9}\text{Fe}_{0.1}\text{SiO}_3$ at lower mantle conditions and its geophysical implications. *J. Geophys. Resaerch* **92**:11437-11444

Horiuchi, H., Ito, E. and Weidner, D. (1987) Perovskite-type MgSiO_3 : single crystal X-ray diffraction study. *Amer. Mineral.* **72**:357-360

Houlier, B., Jaoul, O., Abel, F. and Liebermann, R. (1988) Oxygen and silicon self-diffusion in natural olivine. *Phys. Earth Planet Ints.* **50**:240-250

Hull, D. (1975) *Introduction to dislocations*. Pergamon Press.

Ito, E. and Katsura, T. (1989) A temperature profile of the mantle transition zone. *Geophys. Res. Lett.* **16**:425-8.

Ito, E. and Takahashi, E. (1987) Ultra-high pressure phase transformations and the constitution of the deep mantle. In *High-pressure research in mineral physics*, M. H. Manghnani and Y. Sono, eds. Washington, D.C.:American Geophysical Union, 221-9.

Ito, E. and Takahashi, E. (1989) Postspinel transformations in the system

Mg₂SiO₄ - Fe₂SiO₄ and some geophysical implications. *J. Geophys. Resaerch* **94**:10637-10646

Jackson, W., Knittle, E., Brown, G. and Jeanloz, R. (1987) Partitioning of Fe within high-pressure silicate perovskite. Evidence for unusual geochemistry in the lower mantle. *Geophys. Res. Letts.* **14**:224-226

Jaoul, O. (1990) Multicomponent diffusion and creep in olivine. *J. Geophys. Resaerch* **95**:17631-17642

Jarvis, G.T. and Peltier, W.R. (1989) Mantle viscosity. In *Mantle Convection: Plate Tectonics and Global Dynamics*. Ed. Peltier, W. Gordon and Breach. 389-348

Jeanloz, R. and Richter, F.M. (1979) Convection, composition and the thermal state of the lower mantle. *J. Geophys. Resaerch* **84**:5497-5504

Jeanloz, R. and Thompson, A.B. (1983) Phase transitions and mantle discontinuities. *Reviews Geophys. and Space Phys.* **21**:51-74

Karato, S. (1981) Rheology of the lower mantle. *Phys. Earth Planet Ints.* **24**:1-14

Karato, S. (1989) Plasticity-crystal structure systematics in dense Earth oxides and its implicatins for the creep strength of the Earth's deep interior: A preliminary result. *Phys. Earth Planet. Ints.* **55**:234-240

Kay, H.F. and Bailey, P.C. (1957) Structure and properties of CaTiO₃. *Acta Crystallog.* **10**:219-226

Keyes, R.W. (1963) Continuum models of the effect of pressure on activated processes. In *Solids Under Pressure*. Eds Paul, W. and Warchaver, D.M. 71-99

New York: McGraw-Hill

Kohlstedt, D.L. and Ricoult, D. (1984) High temperature creep of silicate olivines. In *Deformation of Ceramics II*. Eds. R.E. Tressler and R.C. Brandt
New York: Plenum 251-280

Knittle, E. and Jeanloz, R. (1987) Synthesis and equation of state of (Mg,Fe)SiO₃ perovskite to over 100 GPa. *Science* **235**:668-670

Knittle, E. and Jeanloz, R. (1989) Simulating the core mantle boundary. An experimental study of high pressure reactions between silicates and liquid iron. *Geophys. Res. Letters*. **16**:609-612

Kroger, F.A. (1971) The chemistry of compound semiconductors. In *Physical Chemistry: An advanced Treatise Volume 10*. Ed. W. Jost. 229-259

Landolt-Bornstein *Crystal and Solid State Physics*. New York: Springer Verlag (1977,1981)

Lasaga, A.C. (1981) The atomistic basis of kinetics: Defects in minerals. In *Kinetics of Geochemical Processes. Reviews in Mineralogy Volume 8*. Eds A. Lasaga and R.J. Kirkpatrick.

Lees, A.C., Bukowinski, M.S.T and Jeanloz, R. (1983) Reflection properties of phase transitions and compositional change models of the 670 km discontinuity. *J. Geophys. Res.* **88**:8145-59

Lewis, G. and Catlow, C.R.A. (1985) Potential models for ionic oxides. *J. Phys. C: S. State. Phys.* **18**:1149

Lewis, G. and Catlow C.R.A. (1986) Defect studies of doped and undoped

- Barium Titanate using computer simulation studies. *J. Phys. Chem. Solids.* **47**:89-97
- Li, P. and Karato, S. Superplasticity in CaTiO₃ perovskite. *E.O.S.* **72(17)**:287
- Liebermann, R.C., Jones, L.E.A. and Ringwood, A.E. (1977) Elasticity of aluminate, titanate, stannate and germanate compounds with the perovskite structure. *Phys. Earth Planet Ints.* **14**:165-178
- Liebermann, R., Wang, Y. and Liu, X. (1990) Domain structure and phase transitions in CaTiO₃ at high temperature. *E.O.S.* **71(17)**:529
- Machtal, P. and Weber, P. (1991) Intermittent layered convection in a model mantle with an endothermic phase change at 670 km. *Nature* **350**:55-57
- Madon, M., Guyot, F., Peyronneau, J. and Poirier, J.P. (1989) Electron microscopy of high-pressure phases synthesized from natural olivine in the diamond anvil cell. *Phys. Chem. Mins.* **16**:320-330
- Madon, M., Castex, J. and Peyronneau, J. (1989) A new aluminous calcic high-pressure phase as a possible host of calcium and aluminium in the lower mantle. *Nature* **342**:422-425
- Mao, H.K., Hemley, R.J., Fei, Y., Shu, L., Chen, L.C., Jephcoat, A.P., Wu, Y. and Bassett, W.A. (1991) Effects of pressure, temperature, and composition on lattice parameters and density of (Fe,Mg)SiO₃ perovskite to 30 GPa. *J. Geophys. Research* **96**:8069-8079
- Matsui, M. and Price, G.D. (1991) Simulation of the pre-melting behaviour of MgSiO₃ perovskite at high pressures and temperatures. *Nature* **351**:735-737
- Meade, C. and Jeanloz, R. (1990) The strength of mantle silicates at high

pressure and room temperature: Implications for the viscosity of the mantle.
Nature **348**:533-535

Megaw, H.D. (1973) *Crystal structures: a working approach*. W.B. Saunders Company, Philadelphia.

Mott, N.F. and Littleton, M.J. *Trans. Farad. Soc.* **34**:485

Murrell, S.A.F. (1989) Brittle to ductile transition in polycrystalline non-metallic solids. In *Deformation of Minerals, Ceramics and Rocks*. Eds A. Barber and P. Meredith.

Olson, P. (1981) Mantle convection with spherical effects. *J. Geophys. Research* **86**:4881-4890

Olson, P., Schubert, G. and Anderson, C. (1987) Plume formation in the D" layer and the roughness of the core-mantle boundary. *Nature* **344**:209-15.

O'Nions, R.K. (1987) Relationship between chemical and convective layering in the Earth. *J. Geol. Soc. Lond.* **144**:259-274

Parker, S.C. (1982) *Computer simulation of minerals*. Ph. D. Thesis University of London.

Parker, S.C. and Price, G.D. (1989) Computer modelling of phase transitions in minerals. *Adv. Solid State Chem.* **1**:295-327

Parmentier, E.M. (1980) A possible mantle instability due to superplastic deformation associated with phase transitions. *Geophys. Res. Letts.* **8**:143

Peltier, W.R. (1982) Dynamics of the ice age. In *Advances in Geophysics* **24**:1-146 Eds. Saltzman, B. New York: Academic Press.

Peltier, W.R. (1986) New constraints on transient lower mantle rheology and internal mantle bouyancy from glacial rebound data. *Nature* **318**:614-617

Peltier, W.R. Wu, P. and Yuen, D. (1981) The viscosities of the Earth's mantle. In *Anelasticity of the Earth*. Eds. F.D. Stacey, M.S. Patterson and A. Nicolas. 59-77

Poirier, J.P. (1978) Is power-law creep diffusion controlled? *Acta Metal'*, **26**:629-637

Poirier, J.P. (1985) *Creep of crystals. High temperature deformation processes in metals, ceramics and minerals*. Cambridge University Press.

Poirier, J.P. (1988) The rheological approach to the viscosity of planetary mantles: A critical assesment. In: *The Physics of the Planets*. Ed. Runcorn, S. J.Wiley and Sons 161-171

Poirier, J.P. (1989) Lindemann law and the melting temperature of perovskites. *Phys. Earth Plan. Ints.* **54**:364-369

Poirier, J.P. and Vergobbi (1978) Splitting of dislocations in olivine, cross-slip controlled creep and mantle rheology. *Phys. Earth Planet. Ints.* **16**:370-378

Poirier, J.P., Peyronneau, J. Gesland, J.Y. and Brebec, G. (1983) Viscosity and conductivity of the lower mantle: an experimental study on a MgSiO₃ perovskite analogue, KZnF₃. *Phys. Earth Planet. Ints.* **32**:273-287

Poirier, J.P. and Liebermann, R.C. (1984) On the activation volume for creep and its variation with depth in the lower mantle. *Phys. Earth Planet. Ints.* **35**:283-293

Poirier, J.P. Beauchesne, S. and Guyot, F. (1989) Deformation mechanisms for

crystals with the perovskite structure. In *Perovskite: A Structure of Great Interest to Geophysics and Materials Science. Geophysics Monograph 45*. Eds. A. Navrotsky and D.J. Weidner. Amer. Geophys. Union. Washington 1989. 119-123

Price, G.D., Parker, S.C. and Leslie, M. (1987) The lattice dynamics and thermodynamics of the Mg_2SiO_4 polymorphs. *Phys. Chem. Mins.* **15**:181-190

Price, G.D., Wall, A. and Parker, S. (1989) Properties and behaviour of mantle minerals: a computer simulation approach. *Phil. Trans. R. Soc. Lond.* **A328**:391-407.

Ranalli, G. (1982) Deformation mechanism amps in grain-size/stress space as a tool to investigate mantle rheology. *Phys. Earth Planet Ints.* **29**:42-50

Ranalli, G. and Fischer, B. (1984) Diffusion creep, dislocation creep and mantle rheology. *Phys. Earth Planet. Ints.* **34**:77-84

Ranalli, G. (1987) *Rheology of the Earth*. Allen and Unwin.

Richter, F.M. and McKenzie, D.P. (1979) Simple models of mantle convection. *J. Geophys.* **44**:441-471

Richter, F.M. and McKenzie, D.P. (1981) On some consequences and possible causes of layered mantle convection. *J. Geophys. Resaerch* **86**:6133-6142

Ringwood A.E. (1975) *Composition and petrology of the Earth's mantle*. New York: McGraw-Hill.

Ross, N. and Hazen, R. (1989) High pressure crystal chemistry of MgSiO_3 perovskite. *Phys. Chem. Mins.* **16**:415-420

Sabadini, R. and Yuen, D. (1989) Mantle stratification and long term polar wander. *Nature* **339**:373-375

Sammis, C.G. Smith, J.C. and Schubert, G. (1981) A critical assesment of estimation methods for activation volume. *J. Geophys. Resaerch* **86**:10707-10718

Sanders, M.J., Leslia, M. and Catlow, C.R.A. (1984) Interatomic potentials for SiO_2 . *J. Chem. Soc. Comm.* 1271-1274

Sclater, J.G., Jaupart, C. and Galson, D. (1980) The heat flow through oceanic and continental crust and the heat loss of the Earth. *Rev. Geophys. Space Phys.* **19**:394-406

Sotin, C. and Poirier, J.P. (1984) Analysis of high-temperature creep experiments by generalized nonlinear inversion. *Mech. of Materials.* **3**:311-317

Stacey, F.D. (1977) A thermal model of the Earth. *Phys. Earth Plan. Ints.* **15**:341-348

Stacey, F.D. and Irvine, R.D. (1977) Theory of melting: Thermodynamic basis of Lindemann law. *Aust. J. Phys.* **30**:631-40

Stacey, F. D., Fu Rong-Shan and Spiliopoulos, S. (1989) Viscosity structure implied by mantle convection. *Phys. Earth Planet. Ints.* **55**:1-9

Stocker, R.L. and Ashby, M.F. (1973) On the rheology of the upper mantle.

Suito, K. (1977) Phase relations of pure Mg_2SiO_4 up to 200 kilobars. In *High pressure research*, M. H. Manghnani and S. Akimoto, eds. New York: Academic, 255-66

Tilley, R.J.D. (1987) *Defect crystal chemistry and its applications*. Blackie, Glasgow.

Turcotte, D.L. and Schubert, G. (1982) *Geodynamics Applications of Continuum Physics to Geological Problems*. John Wiley and Sons.

Udayakumar, K.R and Cormack, A.N. (1989) Non-stoichiometry in alkaline earth excess alkaline earth titanates. *J. Phys. Chem. Solids*. **50**:55-60

Wall, A. (1988) *Lower mantle minerals: Computer Simulation and Analogue studies*. Ph.D. Thesis University of London

Wall, A. and Price, G.D. (1989) Defects and diffusion in MgSiO_3 : A computer simulation approach. In *Perovskite: A Structure of Great Interest to Geophysics and Materials Science. Geophysics Monograph 45*. Eds. A. Navrotsky and D.J. Weidner. Amer. Geophys. Union. Washington 1989. 45-53

Weertman, J. (1970) The creep strength of the Earth's mantle. *Rev. Geophys. Space Phys.* **8**:145-168

Weertman, J. (1978) Creep laws for the mantle of the Earth. *Phil. Trans. R. Soc. London*. **A288**:9-26

Weidner, D.J. and Ito, E. (1987) Mineral physics constraints on a uniform mantle composition. In *High Pressure Research in Mineral Physics, Geophysics Monograph 38*. Eds. Manghnani, H.M. and Syono, H. A.G.U. Washington.

White, S.H (1985) Defect structures in deformed minerals. In *Short Course in Applications of Electron Microscopy in the Earth Science. Mineralogical Society of Canada*. Ed. J.C. White.

- White, T.J., Segall, R.L., Barry, J.C. and Hutchison, J.L. (1985) Twin boundaries in perovskite. *Acta Crystallog.* **B41**:93-98
- Williams, Q., Knittle, E. and Jeanloz, R. (1989) Geophysical and Crystal chemical significance of (MgFe)SiO₃ perovskite. In *Perovskite: A Structure of Great Interest to Geophysics and Materials Science. Geophysics Monograph 45*. Eds. A. Navrotsky and D.J. Weidner. Amer. Geophys. Union. Washington 1989.
- Wolf, G. and Jeanloz, R. Lindermann melting law: anharmonic correction and test of its validity for minerals. *J. Geophys. Research* **89**:7821-7835
- Wolf, D. (1986) Glacio-isostatic adjustment in Fennoscandia revisited. *J. Geophys.* **59**:42-48
- Woodhouse, and Dziewonski, A. Seismic modelling of the Earth's large scale three-dimensional structure. *Phil. Trans. R. Soc London.* **A328**:1-18
- Wright, K. and Price, G.D. (1989) Computer simulation of iron in magnesium silicate perovskite. *Geophys. Res. Letters.* **16**:1399-1402
- Wu, P. and Yuen, D. (1991) Post glacial relaxation of a viscously stratified compressible mantle. *Geophys. J. Int.* **104**:331-349
- Yaganeh-Haeri, A., Weidner, D. and Ito, E. (1988) Elasticity of MgSiO₃ in the perovskite structure. *Science* **234**:787-789
- Yamada, H. (1984) Viscous creep deformation of polycrystalline CaTiO₃ at elevated pressures. *J. Mat. Science.* **19**:2639-2642
- Yuen, D.A. and Zhang, S. (1987) Deformation of the core-mantle boundary induced by spherical-shell, compressible convection. *Geophys. Res. Letters.*

14:899-902

Zener, C. (1942) Theory of lattice expansion introduced by cold-work. *Trans. A.I.M.E.* **147**:361-368

APPENDICES

Appendix A

Creep Curves for experiments on CaTiO_3 and NaNbO_3

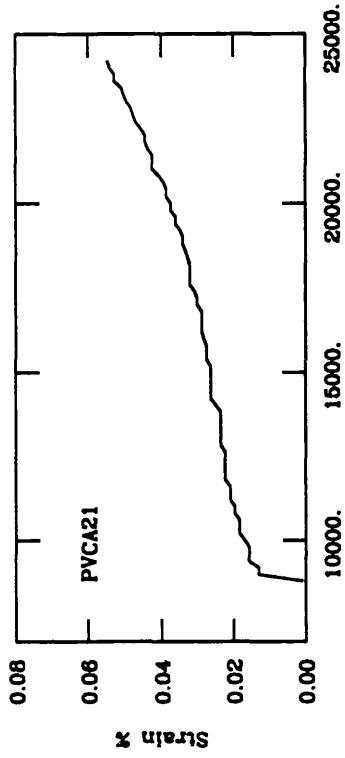
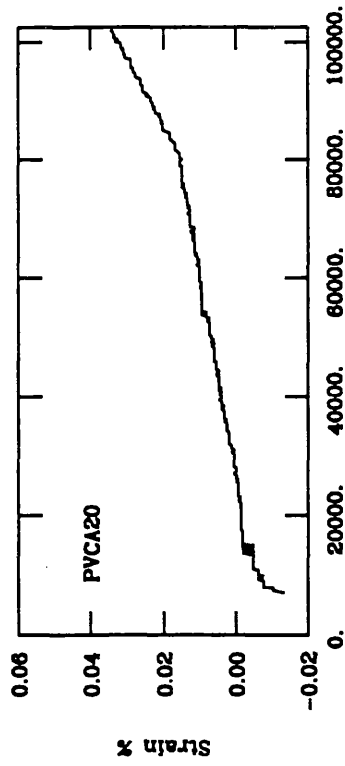
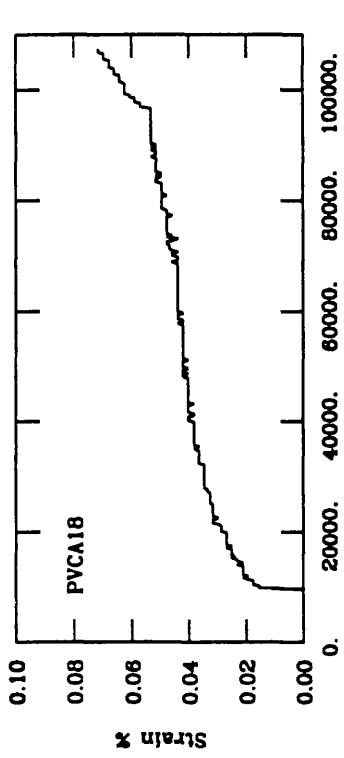
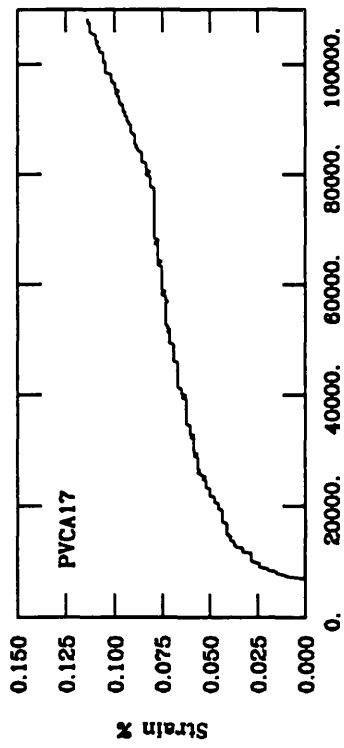


Figure A.1 Creep curves for experiments on CaTiO_3 with stress parallel to $\langle 100 \rangle_{pc}$

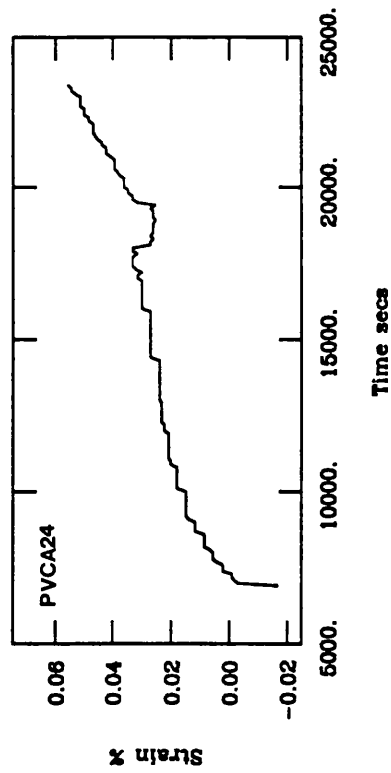
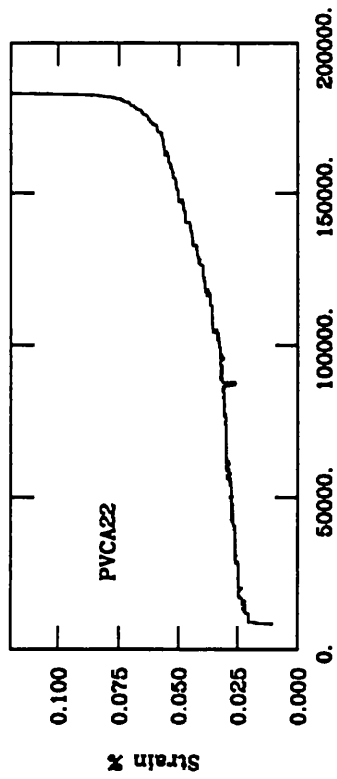
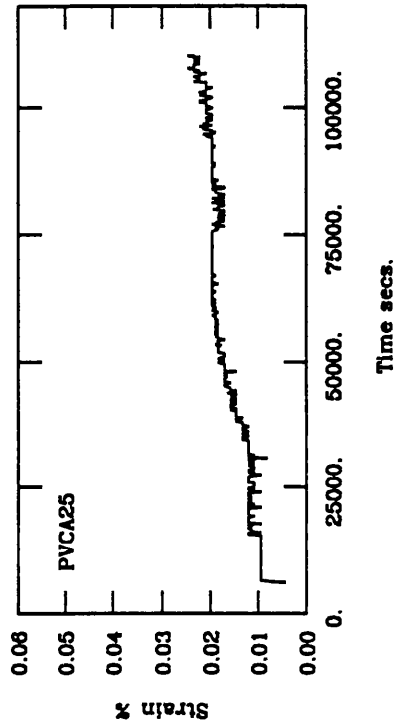
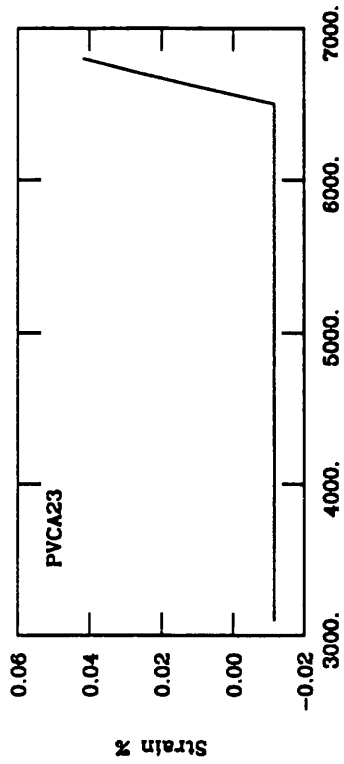


Figure A.1 continued

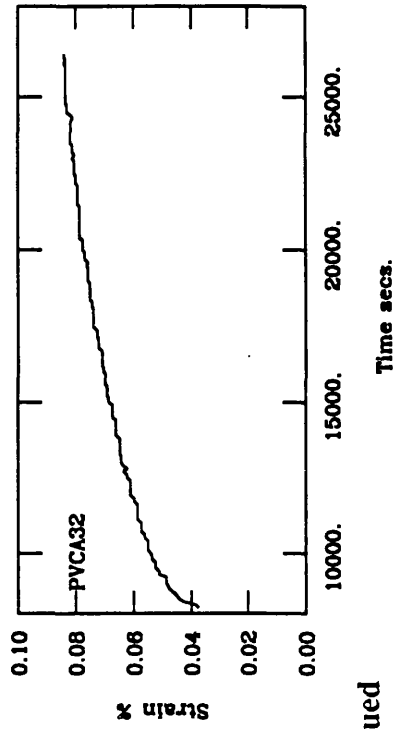
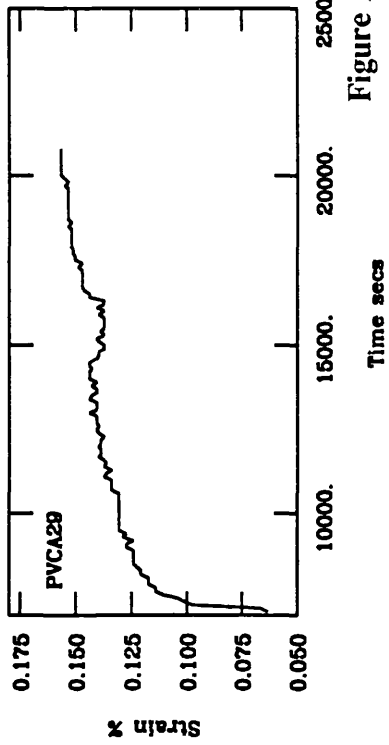
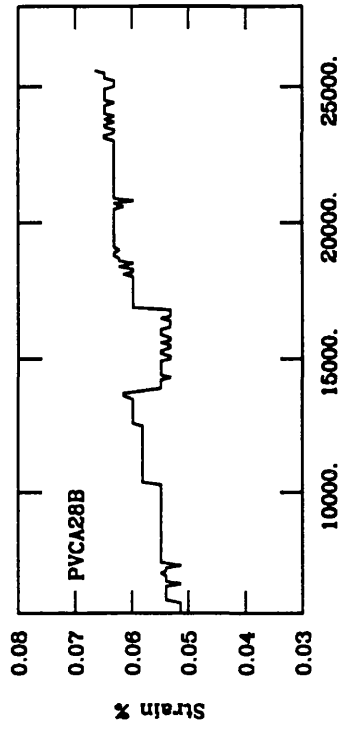
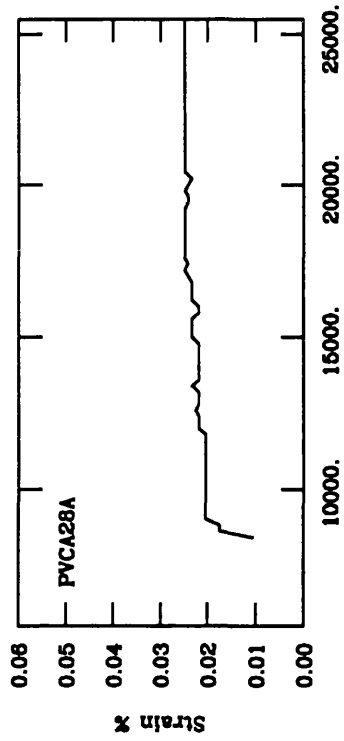


Figure A.1 continued

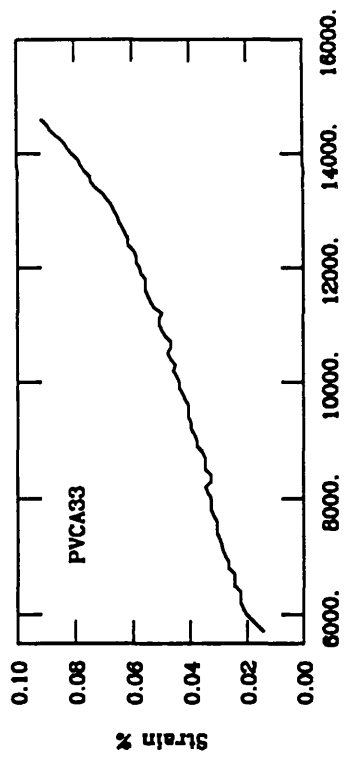


Figure A.1 continued

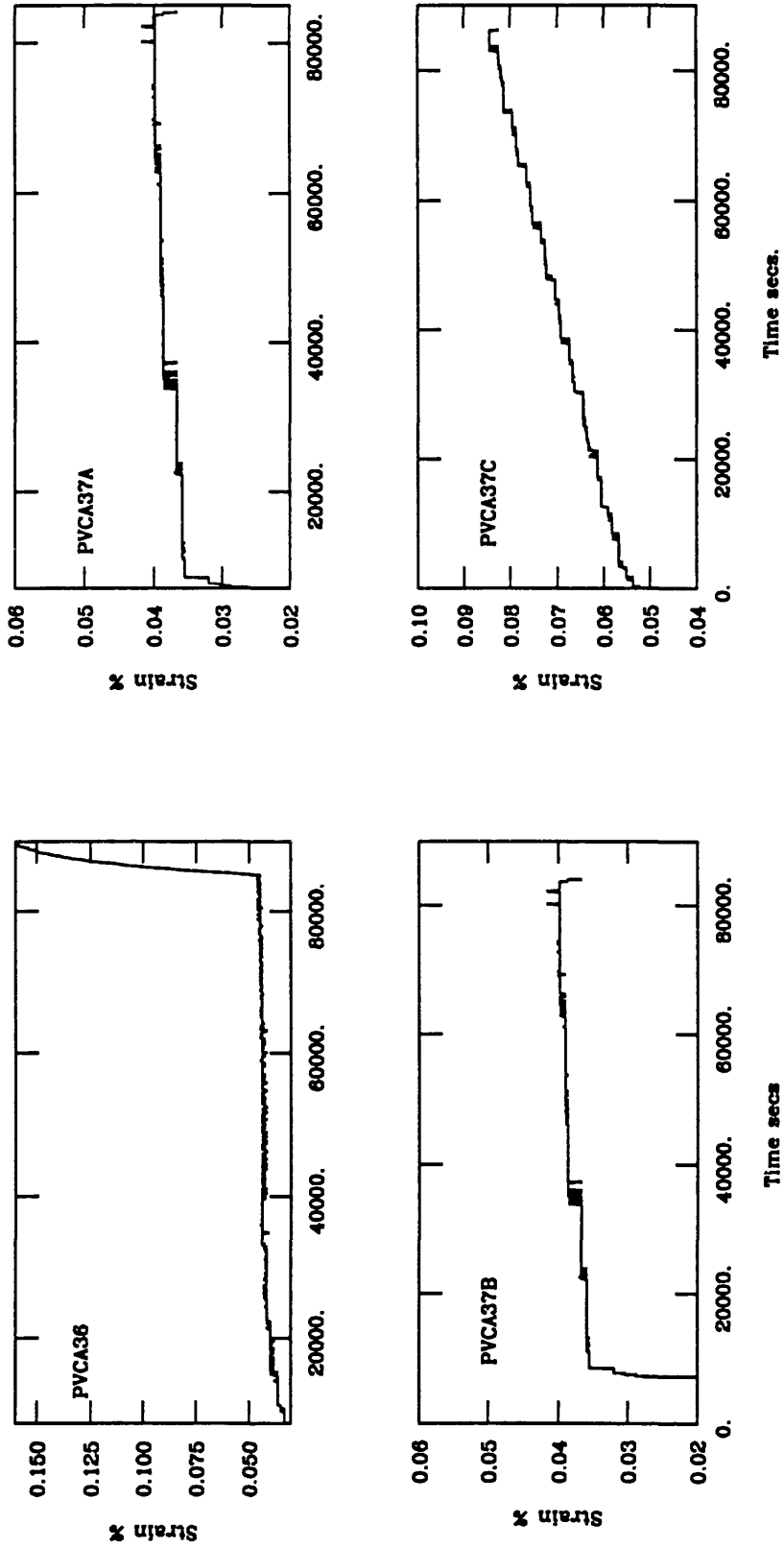


Figure A.2 Creep curves for experiments on CaTiO_3 with stress parallel to $\langle 110 \rangle_{pc}$

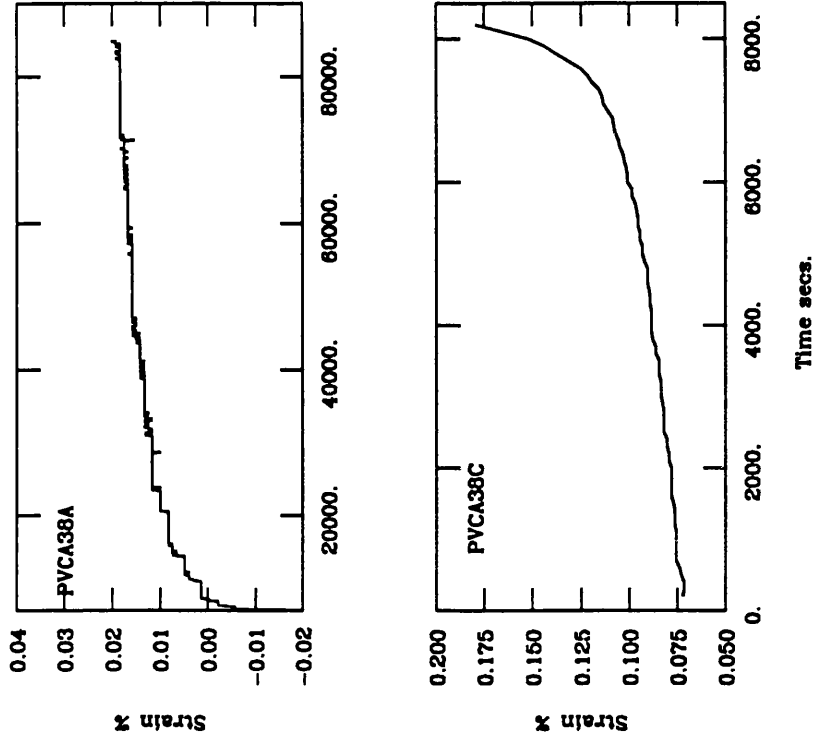


Figure A.2 continued

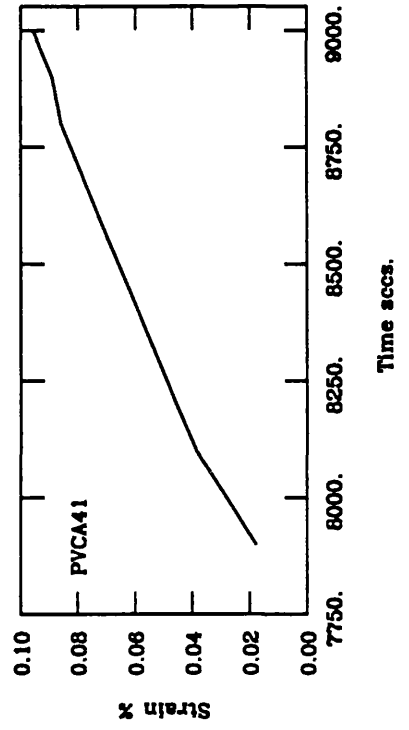
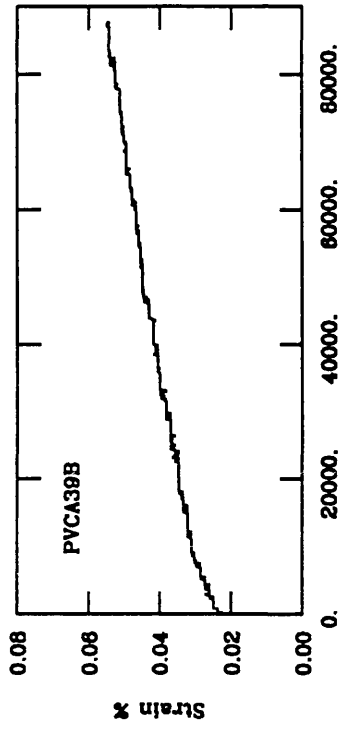
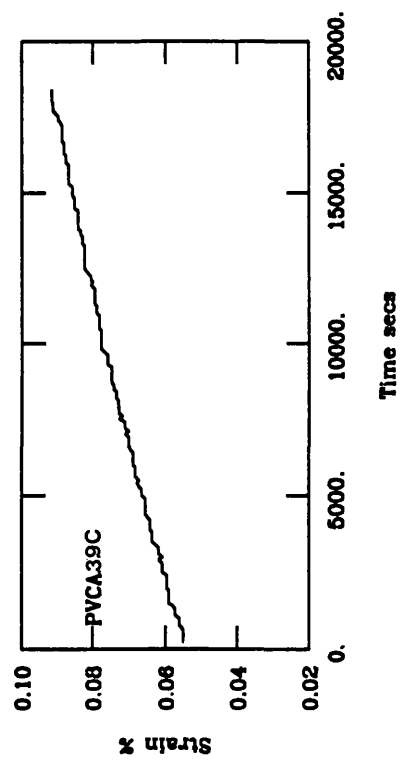
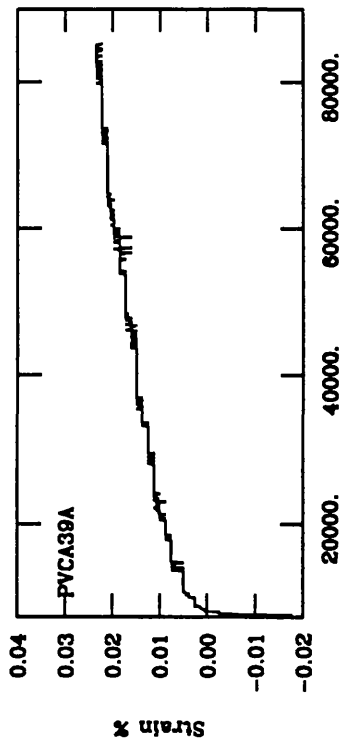


Figure A.2 continued

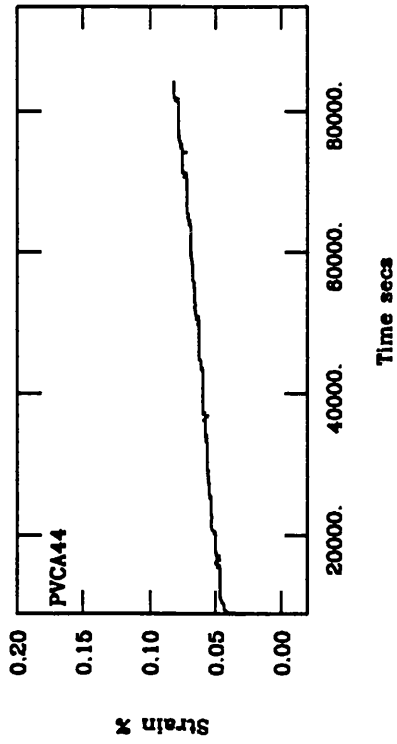
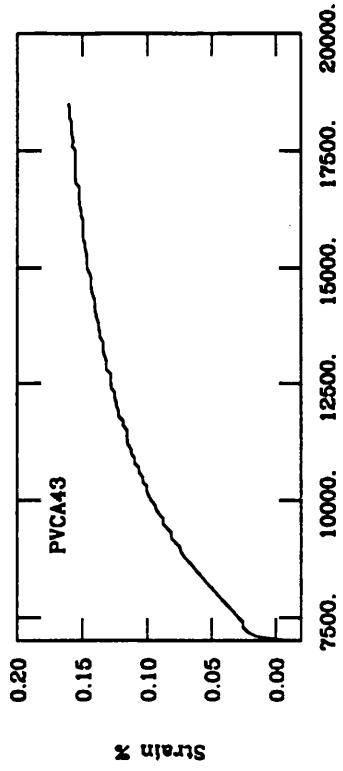
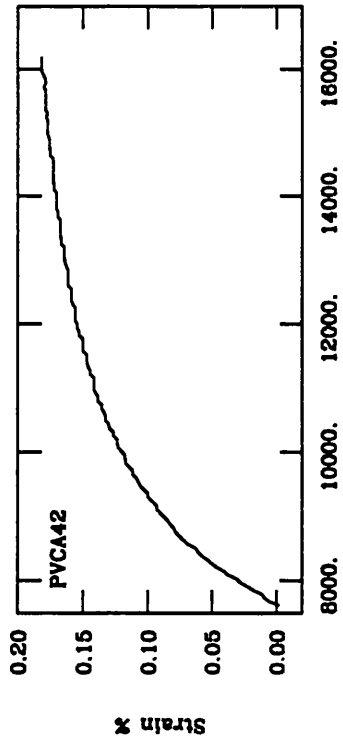


Figure A.2 continued

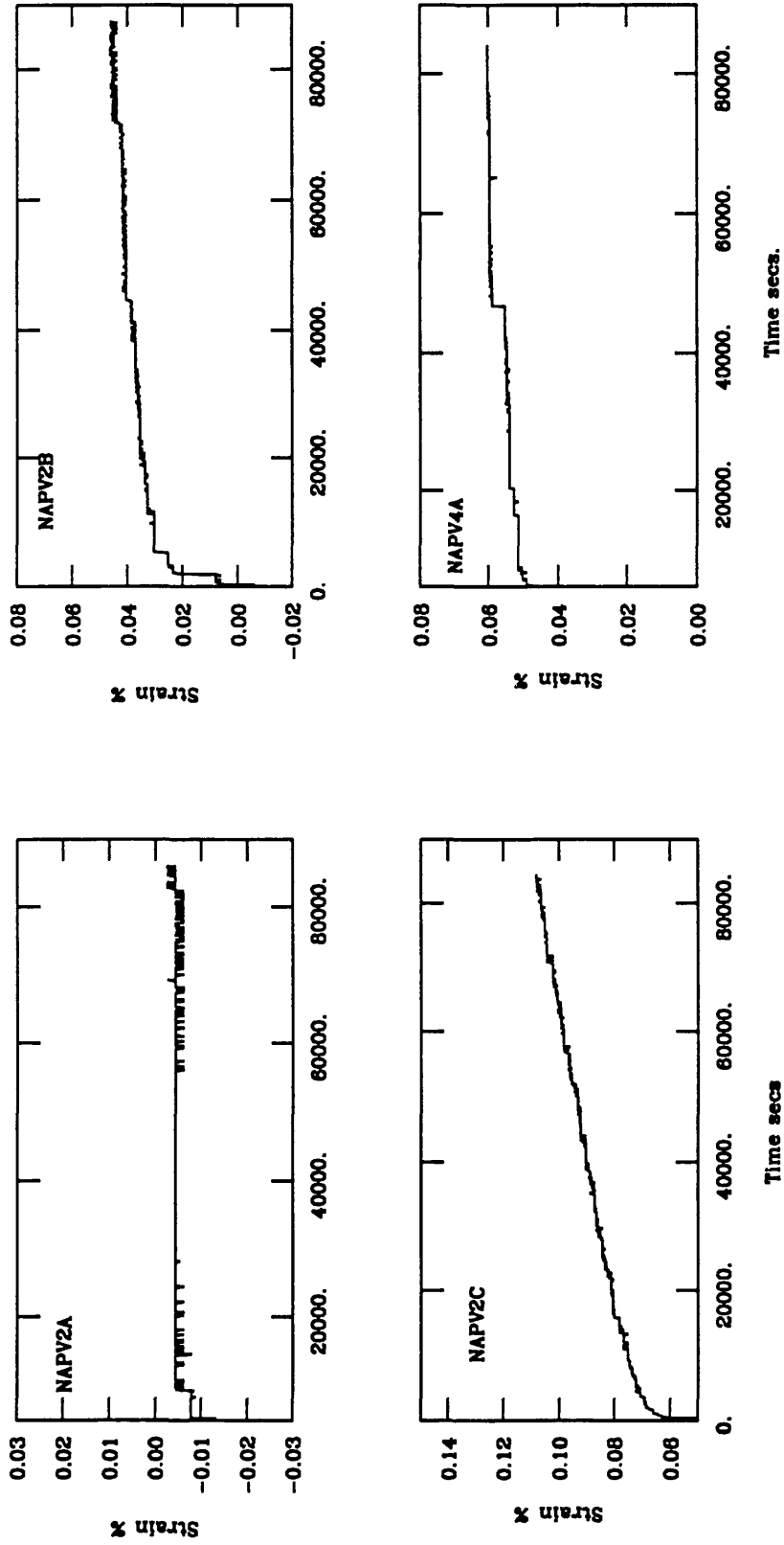


Figure A.3 Creep curves for experiments on NaNbO_3

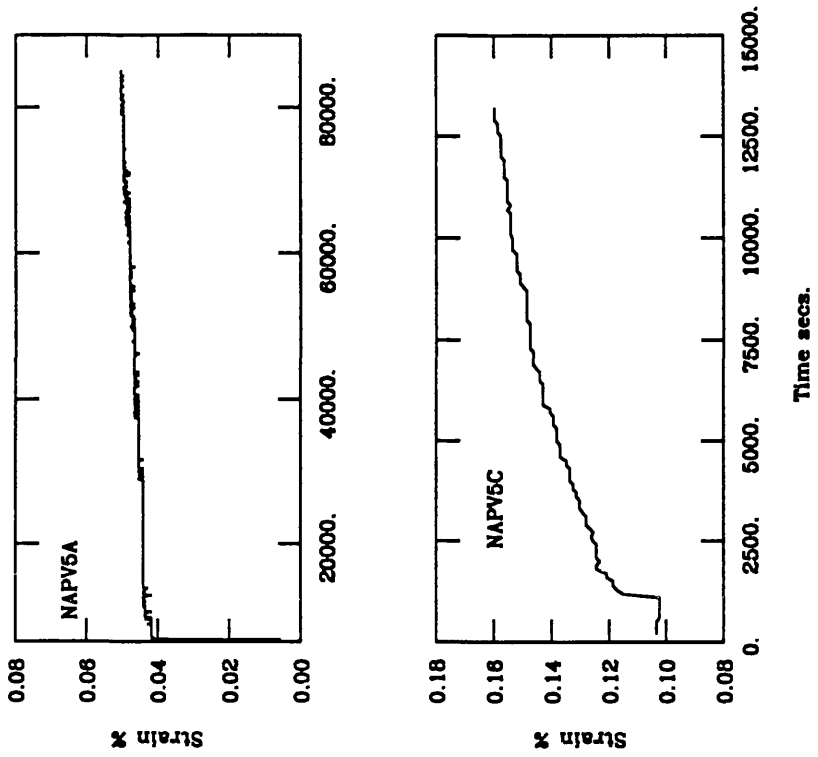


Figure A.3 continued

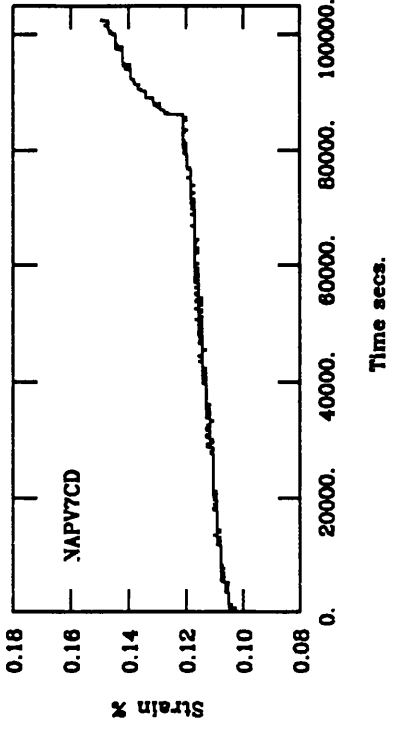
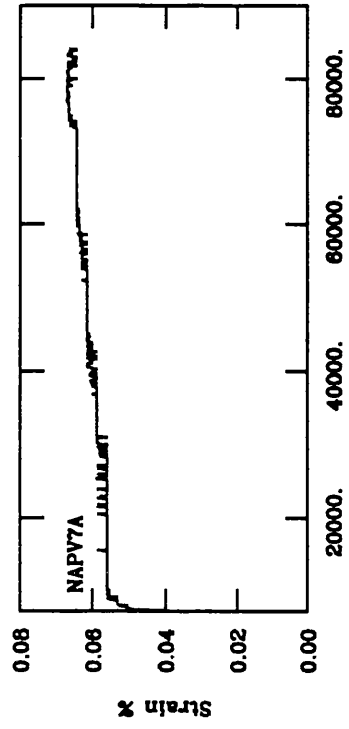
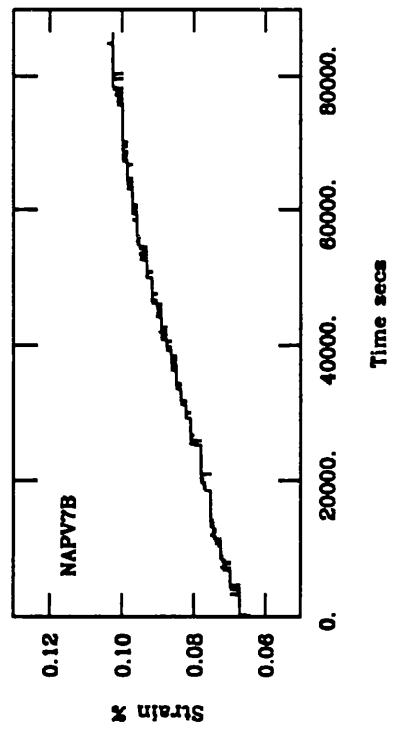
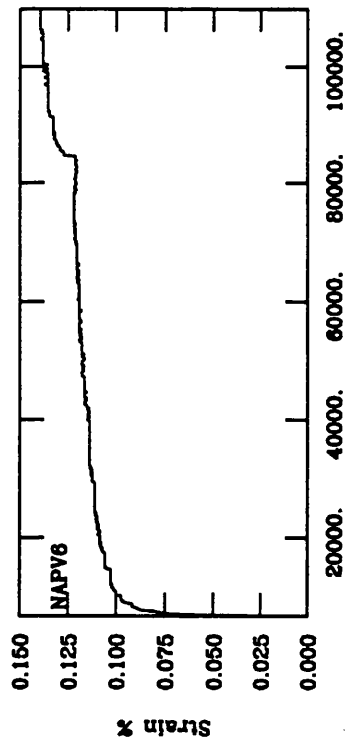


Figure A.3 continued

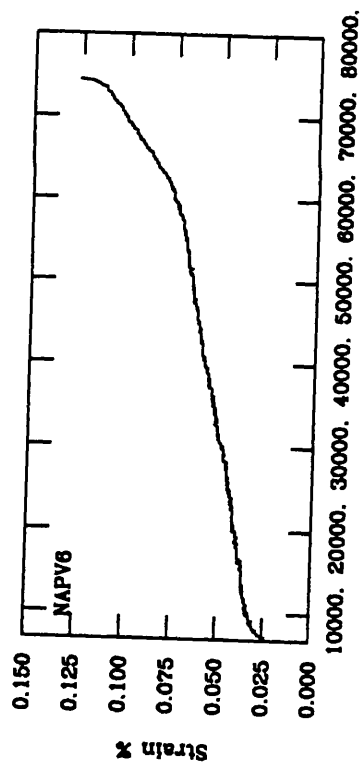


Figure A.3 continued

- **Appendix B**

Fortran 77 program for the construction of deformation mechanism maps

C PROGRAM TO PLOT DEFORMATION MECHANISM MAPS IN STRESS
 C TEMPERATURE SPACE FOR CONSTANT PRESSURE WITH CONTOURS
 C OF CONSTANT STRAIN RATE. STRESS DEPENDANCE OF GRAIN SIZE
 C INCLUDED IN CALCULATIONS OF VISCOSITY. MTHOD AS OUTLINED BY
 C FROST & ASHBY (1982). WRITTEN BY K. WRIGHT AUGUST 1987.
 C VERSION FOR CaTiO3.

C ** Definition of terms : -

C ** Dorn constant.....DORN
 C ** Molecular volume.....VOLL M3
 C ** Pre. exp. volume diffusion.....DOV M2/SEC
 C ** Activation energy diffusion.....EV J/MOLE
 C ** Pre. exp. boundary diffusion....DGB M2/SEC
 C ** Activation energy diffusion....EGB J/MOLE
 C ** Activation volume.....VV M3
 C ** Shear modulus.....U N/M2
 C ** DU/DP.....U1
 C ** DU/DT.....U2 N/M2/K
 C ** Burgers vector.....B M
 C ** Dislocation density.....R M2
 C ** Pre. exp. PowerLawCreep.....DOEFF M2/SEC
 C ** Activation energy PLC.....EEFF J/MOL
 C ** Grain size.....G M
 C ** Grain boundary width.....DEL M
 C ** Bulk modulus.....AK N/M2
 C ** DK/DP.....AK1
 C ** DK/DT.....AK2 N/M2/K
 C ** Coefficient thermal expansion...ALPHA /K
 C ** Pressure.....ZP N/M2
 C ** Melting temperature.....TM K
 C ** Avogadros constant.....AV
 C ** Boltzmanns constant.....BK
 C ** Viscosity.....VISC PA S
 C ** Density.....RHO KG/M3
 C ** Molar mass.....AMASS
 C ** Molar volume.....AVOL
 C ** Stress exponent.....XN
 C ** Diffusion constant.....BETA

C *** Dimension any variables in an array. Use double
 C *** precision. Ensure 1st no. in double arrays has
 C *** the same value as MT and NT in the data set.

DOUBLE PRECISION TEMP(100),ASIGMA(100),A(2),BSIGMA(100)
 DOUBLE PRECISION XPTS(50), YPTS(16), SURFCE(50,16)
 DOUBLE PRECISION CHTS(20),CTEMP(100),SRNET(50,16)
 DOUBLE PRECISION AX(100), AY(100)
 LOGICAL UNUSED(50,16)
 CHARACTER*1 CHAR(1)

```

CHARACTER*50 D
C ** Open the input data set.
WRITE(2,*)'Enter name of data set'
READ(1,999) D
999 FORMAT(A50)
OPEN(5,FILE=D,STATUS='OLD')
C ** Read in constants
C ** QC = start values for Temp arrays.
READ(5,*) QC
C ** MT = No. of counts in arrays in part 1 of prog.
READ (5,*) MT
C ** NT = As above, but for part 2.
READ (5,*) NT
C *** Now read in material parameters for chosen mineral.
READ (5,*) DORN
READ (5,*)XN
READ (5,*)BETA
READ (5,*) VOLL
READ (5,*) DOV
READ (5,*) EV
READ (5,*) DGB
READ (5,*) EGB
READ (5,*) VV
READ (5,*) U, U1, U2
READ (5,*) B
READ (5,*) R
READ (5,*) DOEFF
READ (5,*) EEFF
READ (5,*) CVV
READ (5,*) G
READ (5,*) DEL
READ (5,*) AK, AK1, AK2
READ (5,*) ALPHA
READ (5,*) ZP
READ (5,*) TM
AV = 6.022E23
BK = 1.381E-23
CLOSE(5)
C *** Calculate the position of the mechanism boundaries.
C *** Put values of temperature in an array.
ACOUNT = QC
DO 1 I = 1, MT
TEMP(I) = ACOUNT
ACOUNT =ACOUNT+25.0
1 CONTINUE
C ** Open an output file.

```

```

OPEN(6,FILE='MOUT.DAT',STATUS='NEW')
DO 2 J = 1, MT
C *** Use equations of state to take into account effects
C *** of pressure and temperature.
AAK = AK*(1.0+AK2*(TEMP(J)-300)/AK+AK1*ZP/AK)
UU = U*(1.0+U2*(TEMP(J)-300)/U+U1*ZP/U)
VVV = VV*(1.0+ALPHA*(TEMP(J)-300))
ACTVOL = VVV*(((ZP*AK1)/AK+1.0)**(-1.0/AK1))
VCV=CVV*(1.0+ALPHA*(TEMP(J)-300))
CCVOL=VCV*(((ZP*AK1)/AK+1.0)**(-1.0/AK1))
BB = B*EXP(-(ZP/(3.0*AK)))
VL = VOLL*(1.0+ALPHA*(TEMP(J)-300))
VOL = VL*(((ZP*AK1)/AK+1.0)**(-1.0/AK1))
DQ = ZP*ACTVOL*AV
DCQ=ZP*CCVOL*AV
C *** Calculate values of diffusion terms. Use logs to avoid
C *** overflow.
C *** Boundary diffusion.
C DB = DGB*EXP(-((EGB+DQ)/(8.314*TEMP(J))))
DBL=LOG(DGB)-((EGB+DQ)/(8.314*TEMP(J)))
C *** Lattice diffusion
C DV = DOV*EXP(-(EV+DQ)/(8.314*TEMP(J)))
DVL=LOG(DOV)-((EV+DQ)/(8.314*TEMP(J)))
C *** Effective diffusion rate for dislocation climb.
ALNDF=LOG(DOEFF)-((EEFF+DCQ)/(8.314*TEMP(J)))
C Boundary is then
ALNS1=2*LOG(BB)+2*LOG(UU)+LOG(BETA)-LOG(DORN)-ALNDF-
12*LOG(G)
SL2 = LOG(DEL)+DBL-LOG(G)
S2 = (EXP(DVL))+EXP(SL2)
XF=XN-1
ASIGMA(J)=((S2**(1.0/XF)/1.0E6)*(EXP(ALNS1/XF)))
SSIGMA=ASIGMA(J)/(UU/1.0E6)
C *** AX and AY are normalised axes used to plot the map.
AX(J) = TEMP(J)/TM
AY(J) = LOG10(SSIGMA)
2 CONTINUE
C *** Data output
C *** 1) Material parameters used.
WRITE(6,1001) VOLL
1001 FORMAT(' MOLECULAR VOLUME ',E10.3)
WRITE(6,1002) DOV
1002 FORMAT(' VOLUME DIFF. COEFF. ',E8.3)
WRITE(6,1003) EV
1003 FORMAT(' ACTIVATION ENERGY ',E8.3)
WRITE(6,1004) DGB

```

```

1004 FORMAT(' BOUNDARY DIFF. COEFF. ',E8.3)
WRITE(6,1005) EGB
1005 FORMAT(' ACTIVATION ENERGY ',E8.3)
WRITE(6,1006) VV
1006 FORMAT(' ACTIVATION VOLUME ',E8.3)
WRITE(6,1007) DOEFF
1007 FORMAT(' PLC DIFF. COEFF. ',E8.3)
WRITE(6,1008) EEFF
1008 FORMAT(' ACTIVATION ENERGY ',E8.3)
WRITE(6,1009) G
1009 FORMAT(' GRAIN SIZE ',E8.3)
WRITE(6,1010) ZP
1010 FORMAT(' PRESSURE ',E8.3)
WRITE(6,1011) TM
1011 FORMAT(' MELTING TEMPERATURE ',F8.1)
DO 3 K = 1, MT
WRITE (4,1021) TEMP(J), ASIGMA(J)
1021 FORMAT ('0', F8.2, E11.3)
3 CONTINUE
C *** Now calculate the strain rate for each mechanism
C *** and the net strain rate for a given T and sigma,
C *** divide sigma by strain rate to get viscosity.
C *** Put values of T into an array
BCOUNT = QC
DO 4 I = 1, MT
CTEMP(I) = BCOUNT
XPTS(I) = BCOUNT/TM
WRITE(6,*)XPTS(I)
BCOUNT = BCOUNT + 25.0
4 CONTINUE
C *** Set up loops to step through values of T and Sigma
C *** Take in the effects of pressure as before.
DO 6 K = 1, MT
VL=VOLL*(1.0+ALPHA*(CTEMP(K)-300.0))
VOL=VL*(((ZP*AK1)/AK+1.0)**(-1.0/AK1))
BB=B*EXP(-(ZP/(3.0*AK)))
UU=U*(1.0+U2*(CTEMP(K)-300.0)/U+U1*ZP/U)
VVV=VV*(1.0+ALPHA*(CTEMP(K)-300.0))
ACTVOL=VVV*(((ZP*AK1)/AK+1.0)**(-1.0/AK1))
DQ=ZP*ACTVOL*AV
C ** Calculate values of diffusion terms.
DBL=LOG(DGB)-((EGB+DQ)/(8.314*CTEMP(K)))
DVL=LOG(DOV)-((EV+DQ)/(8.314*CTEMP(K)))
ALNDF=LOG(DOEFF)+(-((EEFF+DCQ)/(8.314*CTEMP(K))))
CCOUNT = 1.0
DO 5 I =1, 2

```

```

A(I) = CCOUNT
C ** Set up an array of stress values.
DO 7 J = 1, 8
IJ = (8-J)*2+I
BSIGMA(J) = A(I)/(10.0**J)
YPTS(IJ) = LOG10(BSIGMA(J))
GR = G
C *** Calculate the strain rate for each mechanism.
C *** For power-law creep....
SLNRP
=(LOG(DORN*VOL)+ALNDF)-(LOG(BK*CTEMP(K))+2.0*LOG(BB*UU))
SR4 =EXP(SLNRP+(XN*(LOG(BSIGMA(J)*UU))))
C *** For Herring-Nabarro creep.....
SRHNA=LOG(BETA)+LOG(BSIGMA(J)*UU)+LOG(VOL)+DVL
SRHNB=LOG(BK*CTEMP(K))+2*LOG(GR)
SRHNC=SRHNA-SRHNB
SRHN=EXP(SRHNC)
C *** For Coble creep.....
SRCA=LOG(BETA)+LOG(BSIGMA(J)*UU)+LOG(VOL)+LOG(DEL)
SRCB=SRCA+DBL
SRCC=LOG(BK*CTEMP(K))+3*LOG(GR)
SRCD=SRCB-SRCC
SRC=EXP(SRCD)
C *** For plasticity
SR2 = 1.0E6*EXP(-(0.5*U*B**3)/(BK*CTEMP(K)))
SRPL = SR2*(1-(BSIGMA(J)*UU/(5.0E-3*U)))
C *** Find the net strain rate.
IF (SRPL .GT. SR4)THEN
SRNET(K,J) = SRHN +SRC+SRPL
ELSE
SRNET(K,J) = SR4 + SRHN +SRC
END IF
IF(SRNET(K,J) .LE. 1.0E-20)THEN
SURFCE(K,IJ)=-30
ELSE
SURFCE(K,IJ)=LOG10(SRNET(K,J))
ENDIF
C *** Find the net viscosity.
C VISC(K,J) =(BSIGMA(J)*UU)/SRNET(K,J)
C VSURF(K,IJ) = LOG10(VISC(K,J))
C *** Data output
WRITE(6,1301) YPTS(IJ),SURFCE(K,IJ)
1301 FORMAT(1X,2E10.3)
7 CONTINUE
CCOUNT = CCOUNT + 2.0
5 CONTINUE

```

```

6 CONTINUE
CLOSE(6,STATUS='KEEP')
C *** Call the various NAG plotting routines to draw the map.
C *** Initiate the plotting.
CALL LN03R
CALL DEVICE(88,500)
CALL DEVPAP(200.,200.,0)
CALL J06WAF
C *** Set the data region and viewport.
CALL J06WBF(0.0D0,1.0D0,-8.0D0,0.0D0,1)
IFAIL = 0
C *** Draw the axes, give them and the map labels.
CALL J06AGF(1,0.0D0,1.0D0,10,0,0,-8.0D0,CHAR,2)
CALL J06AGF(2,-8.0D0,0.0D0,10,0,0,0.0D0,CHAR,2)
CALL J06AHF ('Deformation Map: CaTiO3.')
CALL J06AJF(1,'Homologous temperature T/TM ')
CALL J06AJF(2,'Normalised stress. SIGMA/U')
C *** Set any parameters needed.
DO 8 I = 1,18
CHTS(I) = -1.0*I
8 CONTINUE
NCHTS = 18
ICH = 1
M = MT
N = 16
METHOD = 1
C *** Plot the strain rate contours.
CALL PENSEL(1,0.2,0)
CALL J06GCF(SURFCE,XPTS,YPTS,M,N,NCHTS,CHTS,ICH,
1UNUSED,IFAIL)
CALL PENEND(1,0.2,0)
C *** Plot the boundaries.
CALL PENSEL(1,0.3,0)
CALL J06CAF(AX,AY,MT,METHOD,IFAIL)
CALL J06ACF
C *** Define the key box and draw.
CALL J06WCF(1.05D0,1.3D0,0.1D0,0.9D0)
CALL J06GZF(CHTS,NCHTS,2,8,1)
C *** End the plot.
CALL J06WZF
STOP
END

```

APPENDIX C : SOME COMMONLY USED SYMBOLS

A	Dorn constant
D_{SD}	Self diffusion coefficient
D_{GB}	Grain boundary diffusion coefficient
D_{plc}	Coefficient for dislocation climb
D_0	Pre-exponential for diffusion coefficient
G	Gibbs free energy
g	Gravitational constant
H	Activation enthalpy
K	Bulk modulus
n	Stress exponent for dislocation creep
P	Pressure
Q	Apparent activation energy
R	Gas constant
S	Entropy
T	Temperature
V^*	Activation volume
α	Volume coefficient of thermal expansion
β	Diffusional creep constant
ϵ	Strain
$\dot{\epsilon}$	Strain rate
η	Effective viscosity
μ	Shear modulus
ρ	Density
σ	Stress
Ω	Molecular volume